FACULTY
OF MATHEMATICS
AND PHYSICS
Charles University

DOCTORAL THESIS

Jiří Kozlík

Powder Metallurgy of Hybrid Materials for Advanced Applications

Department of Physics of Materials

Supervisor of the doctoral thesis:	Doc. PhDr. RNDr. Josef Stráský, Ph.D.
Study programme:	Physics of Condensed Matter and Materials Research

Prague 2023

I declare that I carried out this doctoral thesis independently, and only with the cited sources, literature and other professional sources. It has not been used to obtain another or the same degree.

I understand that my work relates to the rights and obligations under the Act No. 121/2000 Sb., the Copyright Act, as amended, in particular the fact that the Charles University has the right to conclude a license agreement on the use of this work as a school work pursuant to Section 60 subsection 1 of the Copyright Act.

In Prague, July 16, 2023 Author's signature .....

Title: Powder Metallurgy of Hybrid Materials for Advanced Applications

Author: Physics of Condensed Matter and Materials Research

Department: Department of Physics of Materials

Supervisor: Doc. PhDr. RNDr. Josef Stráský, Ph.D
Department of Physics of Materials

Keywords: Field-assisted sintering technology; High-throughput methods; Architectured composites; Titanium alloys; Refractory complex concentrated alloys

Abstract:

The field-assisted sintering technology (FAST) is a versatile powder consolidation method, which uses electrical current for rapid heating of the sintered material. It is routinely used for sintering of various metallic materials, but mostly with prealloyed powders as a feedstock. The aim of the thesis is to explore the capabilities of FAST for sintering of composite materials and for using blended elemental powders as a raw material in following areas:

1. Manufacturing of architectured composites
2. Consolidation and ageing in a single processing run (in-situ ageing)
3. Rapid alloy prototyping using blended elemental powders
4. High-throughput experimental investigations of multicomponent phase diagrams

Al6061 + Ti-6Al-4V architectured composite was produced, but issues with the powder penetration into the lattice have arisen due to the small lattice dimensions. Mechanical properties could have been assessed by a three-point bending only. The composite has shown improved strength over the plain, unannealed Al6061 matrix, but a premature fracture when the Al matrix was aged properly. Using FAST was found to be inconvenient for architectured composite manufacturing.

A long, fully dense rod was manufactured from the Ti-5Al-5V-5Mo-3Cr alloy with blended elemental powders as a starting material. The whole process of consolidation, homogenization and ageing was carried out in a single process run and the tensile properties of the alloy was fully comparable to the commercially available material, reaching 1183 MPa of yield strength and a ductility of 6 %. It was shown that FAST can be used for preparation of alloys with good mechanical properties from blended elemental powders.

The phase stability of the Ti-(20–29)Nb-7Zr-(0.2–0.8)O system was investigated using materials with deliberately produced Nb concentration gradient. The critical concentration of 22 wt% of Nb was measured to suppress the α/α''

precipitation. Homogeneous alloys were prepared from the elemental powder blend as well, the phase composition and elastic modulus were measured by X-ray diffraction and resonant ultrasound spectroscopy in the as-sintered and water quenched conditions. The lowest elastic modulus of 64 GPa was measured in the quenched Ti-29Nb-7Zr-0.7O sample. It was demonstrated that samples with a tunable chemical heterogeneity can be prepared FAST.

Finally, we have designed a method for sintering multiple powder blends in a single specimen, able to produce a heterogeneous sample with a wide range of alloy compositions. This method allowed high-throughput investigations of phase equilibria in an AlTiTaNbZr refractory complex concentrated alloy. Using FAST is considered viable and will be explored further.

Out of the explored areas of FAST applications, manufacturing of architectured composites is not very much viable, while the blended elemental based methods have proven themselves useful in research and should be exploited further.

Acknowledgements

Firstly, I would like to thank my supervisor, Josef Stráský, for his unending support and encouragement during my studies.

I would also like to thank the colleagues in our department for all the discussions and insights and for a great atmosphere at the workplace.

The thesis could not be done without the cooperation of the Institute of Plasma Physics, especially without Zdeněk Dlabáček, the master of FAST.

I am also grateful to Prof. Hamish Fraser for giving me the opportunity to stay at The Ohio State University for a very eventful year and to all CEMAS people for showing me many flavors of the USA.

The financial support by Czech Science Foundation and Charles University Grant Agency is also gratefully acknowledged.

Finally, many thanks belong to my wife and daughter, for all the support in my work and for the patience during the months spent by finalizing the thesis.

Contents

Někdo musel tu slepou uličku lidského poznání prohledat a ohlásit světu: 'Tudy ne, přátelé!' /

Someone had to explore that dead end of human knowledge, to report: 'Not here, my friends!'

Divadlo Járy Cimrmana: Vražda v salonním coupé /

Jára Cimrman Theatre: Murder in a Parlor Car Compartment

Introduction

The thesis topic has emerged during my master study at the Department of Physics of Materials as an indirect result of a long-term cooperation with the Institute of Plasma Physics of the Czech Academy of Sciences. At that time, we have used the field-assisted sintering technology (FAST) as a tool for rapid sintering of ultrafine-grained materials. During discussions with my colleagues, often inspired by conference presentations, a couple of other ideas emerged on how to exploit the FAST further and what unconventional materials and experiments can FAST be used to.

I wanted to focus on two fields: architectured composites and using FAST for rapid prototyping of alloys. The first because of the possible synergy between the recent advances in additive manufacturing and the classical powder metallurgy, the second because the need of manufacturing a small sample of an experimental alloy have come up many times during my and my colleagues' research and casting was not always an option for various reasons.

An organization of the thesis is rather unorthodox, due to the diverse palette of the materials prepared and their intended applications. In the first chapter, theoretical background and a literature review is given, concerning mostly powder metallurgy, sintering and the field-assisted sintering technology in particular. The concept of high-throughput methods, emerging in the thesis, is briefly explained and the introduction is closed by the description of the investigated materials.

The second chapter summarizes the aims of the thesis. In the third chapter, characterization methods used throughout the thesis are briefly presented, but without details on the material-specific manufacturing and sample preparation.

The main body of the thesis consists of four chapters, one for each of the different materials prepared. Each of them starts with a detailed description of the material and sample preparation. The results are then presented, discussed and summarized.

Chapter 4 deals with the preparation of composites and joining of dissimilar materials using FAST – an Al6061 + Ti-6Al-4V metal-metal composite with 3D printed Ti-6Al-4V lattice as a reinforcing phase.

Chapters 5 and 6 are focusing on a blended elemental powder metallurgy (BEPM) of Ti alloys, ultimately aimed at the development of new alloys. The method for a large sample preparation is tested using a commercial Ti-5Al-5V-5Mo-3Cr alloy and compared with the conventional processing route. Then, a BEPM approach is used for investigations of β stability in a biomedical Ti-Nb-Zr-O system in chemically homogeneous and heterogeneous alloys.

Finally, tentative results from an ongoing project on a high-throughput mapping of refractory complex concentrated alloys are presented in Chapter 7, as the method was developed as an extension of the investigations of heterogeneous Ti-Nb-Zr-O alloys. The concluding chapter discusses main achieved results in the context of FAST applications and summarizes the thesis outcomes.

1 Theoretical Background

In this chapter, an introduction into the powder metallurgy and sintering will be given. The field-assisted sintering technology will be then reviewed in more detail, focusing on a complex part manufacturing, upscaling of the method and the blended elemental powder metallurgy.

The next part will provide a short introduction into the concept of high-throughput methods and a CALPHAD framework, used in Chapters 6 and 7. Finally, an overview of the investigated materials (Ti alloys, Al-Ti composites and complex concentrated alloys) will be given at the end of the chapter.

1.1 Powder Metallurgy and Sintering

Powder metallurgy is a broad field of materials science and engineering dealing with manufacturing of metallic parts from powders as a feedstock material. Contrary to the conventional approach which starts with casting and forging, followed by machining to the final shape (top-down approach), powder metallurgy represents a bottom-up approach, in which the part is built by bonding the raw material (powder) together to form the specified shape.

The field covers many aspects of powder production and thermomechanical treatment, methods of consolidating powder into bulk material and post-processing treatment [1]. Technically, additive manufacturing (i.e. 3D printing of metals) is also a powder metallurgy method, but it is nowadays generally viewed as a separate branch of material science.

The thesis focuses on sintering of materials, in particular on sintering by field-assisted sintering technology (FAST). The definition of sintering follows, according to [2]:

> *"Sintering is a thermal treatment for bonding particles into a coherent, predominantly solid structure via mass transport events that often occur on the atomic scale. The bonding leads to improved strength and lower system energy."*

The most widely known application of sintering is pottery – with its history as old as the human civilization itself.

1.1.1 History

Sintering of ceramics is known to the mankind for millennia: the oldest known man-made ceramic object is the Venus of Dolní Věstonice, dating back to 29,000–26,000 BC [3]. The powder metallurgy of metallic materials is related

to the origins of steelmaking. The primitive furnaces were unable to reach the temperatures needed for melting the iron, so the bulk metal was made by reducing small iron ore chunks and then hammering the iron sponge into a bulk material. Some jewelry made by ancient Incas were also produced by powder metallurgy [1].

The innovations in the steelmaking during the Industrial revolution favored casting. The renaissance of powder metallurgy started with a sintering of tungsten carbide tools during early 20th century [1]. As in many other fields, significant advances were done during the WWII and the research continued in the post-war years.

Nowadays, powder metallurgy is mostly used for manufacturing of objects, which would be difficult to produce by other methods due to a complex shape, poor machinability, high melting point, high reactivity in the liquid phase, made of difficult-to-alloy alloys, etc. A significant effort is devoted to near-net shape processing – manufacturing of objects as close to their desired final shape as possible to minimize the post-processing steps.

1.1.2 Principles of Sintering

The driving force for the sintering process is a reduction of the surface energy of individual powder particles. This driving force is naturally present at ambient conditions as well, but the sintering rate is severely limited by the kinetics of the process involved. We will focus on a solid-state sintering of metallic materials, which is mostly governed by diffusion [2].

Prior to the sintering, *a green body* is prepared by cold pressing or binding the powder into the desired shape. At this point, particles are touching each other at only a small fraction of their surface. When the temperature is increased to a level which is sufficient for the diffusion activation, a neck is formed between neighboring particles. Thanks to the surface energy, a Gibbs-Thompson effect creates a positive pressure under the surface with a positive curvature (such as particle surface) and a negative pressure under the negatively curved surface (such as the neck). This leads to a prevailing mass transport from the particle to the neck, as shown in Figure 1.1.

As the process continues, the interparticle spaces are eventually closed, forming pores. They can either close during further sintering, or can be retained in the material, filled with the sintering atmosphere. The decrease in porosity can be directly connected to the macroscopic shrinkage of the sample. This allows using dilatometric data (if available) for tracking of the sintering progress.

When this process occurs without any external stress applied, it is called *free sintering*. However, it is also possible to apply an external pressure during sintering, which leads to activation of plastic flow as an additional sintering mechanism. Moreover, application of a stress also leads to enhancing the mass transport rate similarly to a creep. This family of methods is called *pressure-assisted sintering*.

A wide range of materials can be prepared by sintering, which would be impossible or difficult to prepare by other methods, such as tungsten carbide tools. Furthermore, using sintering (or powder metallurgy in general) can lead

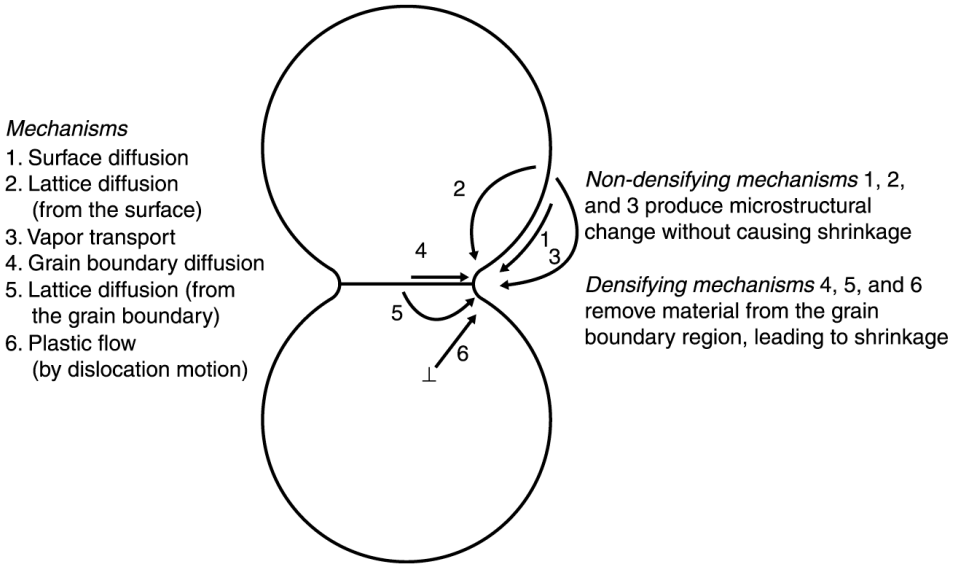

Figure 1.1: Processes involved in solid-state sintering [2]

to lower contamination than during the conventional processing due to lower temperatures involved and the absence of a liquid phase. A formation of dendrites can be also prevented by avoiding the solidification phase transition.

Naturally, there are some drawbacks associated with the sintering. Firstly, it is a generally higher price of powdered raw materials compared to bulk feedstock, which must be balanced by some added value (e.g. near-net shape processing). Next, the powders have high specific surface and are more prone to contamination (oxidation in particular) and cannot be usually prepared with the purity as high as of bulk materials. Porosity is also an issue to be dealt with, unless very high sintering temperatures are used.

1.1.3 Field-Assisted Sintering Technology

The *field-assisted sintering technology* (FAST), also known as *spark plasma sintering* (SPS) or *electric current-assisted sintering* (ECAS) is a pressure-assisted sintering method, using Joule heat of the electric current passing directly through the sintering die and the specimen. The first pressureless electric current sintering was patented in 1906 for manufacturing of lightbulb W and Mo filaments [4, 5]. In 1913, an apparatus was patented by Weintraub [6] for pressure-assisted electric current sintering, similar to modern FAST furnaces (both shown in Figure 1.2). The development of the methods and the important related patents are reviewed in [7].

The operating principle is simple – the powder is placed into a conductive die (usually made of graphite), compressed by two pistons and heated by an electric current passing through the pistons, outer die and (if conductive) the specimen. Thanks to this design, in which the specimen itself acts as a heat source, very high heating rates are possible, reaching 1000 K/min (depending on the sample size) [8]. The whole assembly is typically enclosed in a vacuum chamber to protect the powder from oxidation. Cooling is achieved mainly by thermal radiation from the outer die (at high temperatures) and by heat

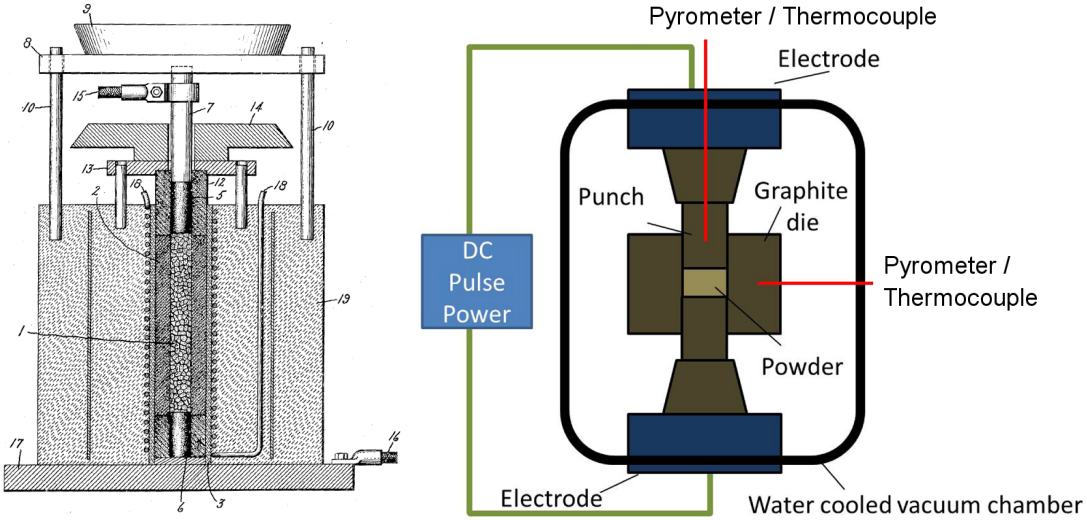

(a) The 1913 sintering patent [6] (b) A present sintering device illustration [8]

Figure 1.2: Schematic diagrams of the FAST furnaces

conduction to the upper and lower pistons, which are water-cooled. Unlike heating, it cannot be actively controlled and the maximum achievable cooling rate can reach hundreds of K/min, which is comparable to air cooling.

The main advantage of FAST is its ability to sinter samples in shorter times than the other sintering methods, such as conventional free sintering or hot (isostatic) pressing. A typical FAST sintering run takes minutes, while a standard duration of other sintering methods counts in hours [8]. There is still no universal agreement on the reason for this. The presence of plasma (hence *spark plasma sintering*) was disproved by in-situ atomic emission spectroscopy performed by Hulbert et al. [9]. Also, there was a hypothesis about high current density and local overheating at the necks between the particles, but the numerical models have shown that the heat conduction is fast enough at this length scale to equalize the temperature distribution [10, 11]. The effect of electromigration was also rejected by direct observation [12]. So far, it seems that there is no special mechanism, other than a combination of high heating rate, localized heating and a mechanical compression. Finally, the accuracy of the temperature measurement is sometimes disputed, as the sensors (both thermocouple and pyrometer) are placed in the graphite tooling several mm from the sample.

Temeperature Homogeneity and Upscaling of FAST

Measurements of a temperature homogeneity within the sample were performed in [13]. Thermal and electrical conductivity were both found to be important factors – best homogeneity was achieved with the insulating sample, which is heated from the outside by a current passing through the die only. The temperature at the edge of a conductive Cu sample was 40 K lower than in its center – the sample is cooled from the outside, but the thermal conductivity of an electrically conductive sample is also good, contributing to the temperature homogenization. Partially conductive samples are the worst case

scenario, with the temperature difference up to 400 K. Numerical simulations have been performed with similar results [14].

The die insulation was found to greatly decrease the energy consumption (up to 3× for conductive samples and 5× for insulating samples) and improve the temperature homogeneity [15]. Different sizes of the FAST furnaces were compared in [16], from laboratory to industrial scale. It turned out that the larger devices are generally more homogeneous in temperature. The authors were able to prepare large, fully dense samples with dimensions 100 mm × 60 mm ($d \times h$) from a TiAl intermetallic compound.

Majority of the FAST produced samples have a cylindrical shape with the base diameter significantly larger than its height. However, a possibility to manufacture rod-shaped samples would be useful for preparation of tensile specimens of a standard size. A modification of FAST called spark plasma extrusion was promoted in [17], with the original patent dating back to 1983 [18]. In this setup, the extrusion nozzle acts as one electrode and the ram as the second. When compared with the FAST-manufactured Al at the same temperature, the spark plasma extruded samples exhibited lower porosity and higher hardness. Titanium was first consolidated by this method by Hallet et al. [19] at 806 °C (α phase field) and 1234 °C (β phase field), but only the extrusion in the β field lead to a crack-free specimen.

To increase the throughput of the method, multiple smaller samples can be prepared in a single sintering run when using a special die assembly design [8]. A combination of a near-net shape sintering and a precision forging called a *FAST-forge* method was developed in [20]. This could reduce the cost of the thermomechanical processing and the material waste, while keeping the precision shape control achieved by forging. When applied to a Ti-6Al-4V alloy (wt%), the microstructure and mechanical properties were comparable to conventionally prepared bulk material. Similar results were achieved in [21] with FAST-forged Ti-5Al-5V-5Mo-3Cr alloy (wt%), being able to produce a material not different from the conventional forging.

The preparation of net shape products is relatively easy for the samples with a translational symmetry along the compression direction. Small Cu dog-bone specimens for mechanical testing were manufactured in a one-step process by [22]. Manière et al. [23] were able to prepare a Ni cogwheel, with the temperature homogeneity ensured by alumina spacers above and below the metal powder. Finally, a net shape turbine blade made of TiAl was successfully prepared by [24] with a specially designed die assembly with multiple moving/sliding parts to allow continuous compression of the complex shape. The blade exhibited good creep resistance, but slightly worse RT ductility than the conventionally manufactured blade.

1.1.4 Blended Elemental Powder Metallurgy

This method, abbreviated as BEPM, is used and investigated in Chapters 5, 6 and 7. The main goal of this branch of powder metallurgy is a preparation of fully dense material from a blend of elemental or master alloy powders. This is achieved by either performing the consolidation at significantly higher temperatures than usual (to promote the diffusion and homogenization) or

by a standard consolidation followed by a homogenization heat treatment at higher temperature. Mechanical alloying and milling are also sometimes used to improve the material homogeneity.

The benefits of the BEPM are usually reaped in the lab-scale alloy development. It provides a great variability in alloy compositions which may be prepared, without the necessity for an expensive production of a prealloyed powder first. It also allows preparing a compositionally graded materials with a greater control over the gradients than in diffusion couples. On the other hand, for widely used and standardized alloys at the industrial scale, using prealloyed powders is often cheaper in terms of both material and processing.

The main issue in the BEPM is reaching the desired level of chemical homogeneity. For this, the temperature and/or duration of the sintering must be significantly increased from the level necessary for a plain consolidation. In [25], even a refractory alloy (prealloyed equiatomic HfNbTaTiZr alloy) was readily sintered to full density (porosity $< 0.3\,\%$) after 2 min at 1000 °C, whereas even 60 min at 1300 °C was not sufficient to reach chemical homogeneity in Ti-39Nb (wt%) alloy made of blended elemental powders (with Nb particles having $\sim 60\,\mu m$ in diameter) [26]. Both methods used FAST as a consolidation method.

Ti-22Nb-4X (at.%, X = Al, Sn or Ta) was sintered from blended elemental powders for 20 min at 1100 °C and then solution treated for 4 h at 1100 °C [27]. A single-phase material was prepared, but the chemical homogeneity was not assessed. Ti-35Nb-10Ta-(0-4.5)Fe (wt%) was sintered for 3 h at 1300 °C, but the chemical homogeneity was still not achieved [28]. Taddei et al. ran a parametric study of the homogenization kinetics [29] on Ti-35Nb-7Zr-5Ta (wt%) biomedical alloy in the temperature range between 900 and 1700 °C (1 h free sintering after cold isostatic pressing). With the powder particle size of approximately $20 - 60\,\mu m$, the Ta powder has been fully dissolved between 1300 and 1500 °C and the alloy was chemically homogenized between 1500 and 1700 °C. The dissolution kinetics of various elements in the Ti-5Al-5Mo-5V-2Cr-1Fe (wt%) alloy was investigated in [30], showing that addition of Fe can enhance the diffusion rate of other elements. Ti-5Al-2.5Fe (wt%) alloy was prepared with Fe and Al introduced as blended elemental powders or intermetallic compounds in [31]. Kirkendall porosity remained after dissolution of pure Fe particle, while more homogeneous microstructure was achieved by using intermetallics.

Mechanical milling and alloying was also employed to reduce the particle size and improve the homogenization kinetics [32]. After 50 h of milling and sintering at 1250 °C, the Ti-40Nb (wt%) alloy was chemically homogeneous. However, mechanical milling often induces additional contamination of the material during the process (mostly by O, N and Fe), which was not measured in the paper. A similar experiment was performed with Ti-35Nb-7Zr-5Ta (wt%) alloy [33]. After 60 h of milling, O concentration increased from 0.16 to 0.25 wt% and Fe from 0.07 to 1.58 wt%. As both elements strongly influence the phase transformations in Ti, this additional contamination during processing is undesirable.

Although not a pure BEPM method, additive manufacturing of compositionally graded materials is currently gaining popularity in research, although

the idea is not new [34]. The heterogeneity is achieved by feeding different powders from multiple hoppers with a variable ratio. The homogenization then occurs only locally in the meltpool in the liquid phase (unlike BEPM, which occurs in a solid phase).

All in all, BEPM is mostly used for determining the influence of individual alloying elements (using the base alloy powder and a single elemental powder) and for development of new alloys (using multiple elemental powders). From this, it is only a short step towards high-throughput methods.

1.2 High-Throughput Methods

Rather than being a set of methods only, the high-throughput approach is more a strategy plan for material development. The underlying idea is this: one should use the fast and cheap methods first to screen the available materials and select promising candidates for the next level of more demanding testing, leading to even narrower selection of candidates, etc. The paradigm is schematically illustrated in Figure 1.3. An excellent review of the currently available methods and their experimental challenges was recently published by Miracle et al. [35].

Computational methods are the first step in alloy selection. Ab-initio calculations, such as those provided by a density functional theory (DFT), can be used directly to assess the phase stability [36], or they can be incorporated into a more complex framework, such as CALPHAD (CALculation of PHAse Diagrams) method.

1.2.1 CALPHAD

The CALPHAD method provides a bridge between the classical thermodynamics of materials and the experimental data available. At first, a model of a given phase is designed and a corresponding Gibbs energy function is constructed. This semi-empirical function typically depends on temperature, pressure and composition and has some free parameters which need to be determined by fitting the function to the experimental data. In a CALPHAD approach, essentially any data which can provide some useful information about the Gibbs energy can be used – calorimetric data, transition temperatures, equilibrium compositions etc. [37]

The Gibbs energy functions are stored along with the set of parameters for each phase in a thermodynamic database. Phase equilibria can be then calculated by a minimization of a total Gibbs energy for a given set of phases of interest. In this way, both stable and metastable phase diagrams can be calculated, along with the thermodynamic properties at the specified conditions. The calculation can be readily performed for wide ranges of conditions and commercial software and databases, such as ThermoCalc, are available for this.

The method is very powerful in its ability to absorb virtually any relevant data. However, it should be stressed that the method can be only as good as the data provided. The results can be very accurate for conditions where large

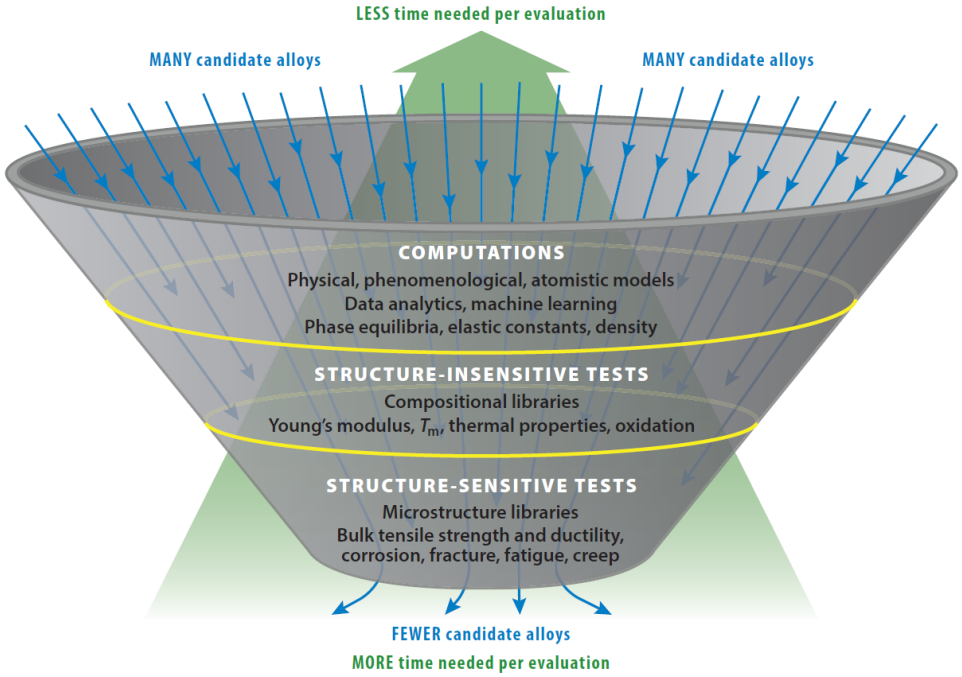

Figure 1.3: The high-throughput strategy for efficient development of new materials [35]

datasets exist, such as commercial, well established alloying systems, but the reliability decreases when extrapolation is required and the results should be handled with caution [35].

1.2.2 High-Throughput Investigations of Phase Diagrams

A typical approach for experimental assessment of the phase diagram follows this pathway: a sample of a certain nominal composition is prepared, annealed at a specified temperature until equilibrium is (assumed to be) reached and subjected to a quantitative characterization of chemical and phase composition (by means of SEM, TEM, XRD, EDS/WDS, etc.). The diagram is then constructed by plotting the tie-lines and tracing boundaries of various regions. This naturally involves preparation of numerous samples, making the process time- and material-consuming.

A smarter way is to prepare samples which would allow to investigate many compositions at once. This is actually an old idea – using diffusion couples for measurements of compositionally dependent diffusion coefficients is a standard method [38, 39]. The same approach can be used for getting the information about the equilibrium phase composition as well under one condition: the system must be locally homogeneous, i.e. at the scale of the experimental method used for characterization. For a suitable specimen geometry, many of the tasks can be automated, e.g. the SEM imaging, EDS and XRD acquisition, etc. We have used FAST for preparation of such a sample, which will be shown in Chapter 7.

The large amount of acquired data can be then used as an experimental dataset for a CALPHAD assessment, further improving the accuracy of the database.

1.3 Studied Materials

1.3.1 Titanium Alloys

The investigations of Ti alloys form the core part of the thesis – the Chapters 5 and 6. Therefore, a brief introduction is given here.

Titanium is a light transition metal, discovered in 1791 by Martin Heinrich Klaproth, but not isolated until 1910 [40]. The first commercially feasible production process was discovered by Wilhelm Justin Kroll in 1940 [41] and it is still used until today. The complexity of production and the absence of continuous process are the main factors causing higher cost of titanium in comparison with other structural materials.

Thanks to its low density and high strength, titanium alloys were mostly used in aerospace applications during the Cold War. The workhorse titanium alloy, Ti-6Al-4V, was developed in 1950s and is still the single most used Ti alloy until now [41]. For example, the famous Lockheed SR-71 'Blackbird' structure consisted of 85 % titanium.

Pure titanium is an allotropic metal with two stable crystallographic modifications. A hexagonal close-packed (hcp) structure, denoted as α phase, is stable at low temperatures up to $T_\beta = 882\,^\circ\mathrm{C}$ (so-called β transus temperature), and a body-centered cubic (bcc) structure, denoted as β phase, is stable above this temperature. The unit cells and lattice parameters of both phases are drawn in Figure 1.4.

The stability of the phases can be modified by alloying with other elements, which can be then grouped according to their effect on the equilibrium phase diagram. The classification of the elements and the typical phase diagrams are drawn in Figure 1.5.

The β stabilizing elements, such as V, Zr, Nb, Mo, Fe, etc., decrease the β transus temperature and a two-phase $\alpha + \beta$ region is formed. These can be further divided into intermetallic-forming elements (creating eutectoid phase diagrams, e.g. Fe) and so-called isomorphous elements (e.g Mo, Nb,...). Majority of the alloying elements used in the titanium industry are β stabilizers.

Among α stabilizing elements, which increase the β transus temperature, only three are of a practical importance – N, O and Al. Out of them, only Al is usually added deliberately for α phase stabilization, while the N and O are present as impurities. However, their effect on the phase stability is strong and they may cause embrittlement of the alloy, so it is desirable to keep their concentration low.

Apart from the stable α and β phases, two important metastable phases can be found in β-stabilized alloys – an orthorhombic α'' phase (α'' martensite) and a hexagonal (but not close-packed) ω phase. Figure 1.6 shows the metastable phase diagram of Ti alloyed with a β-stabilizing element. The solid

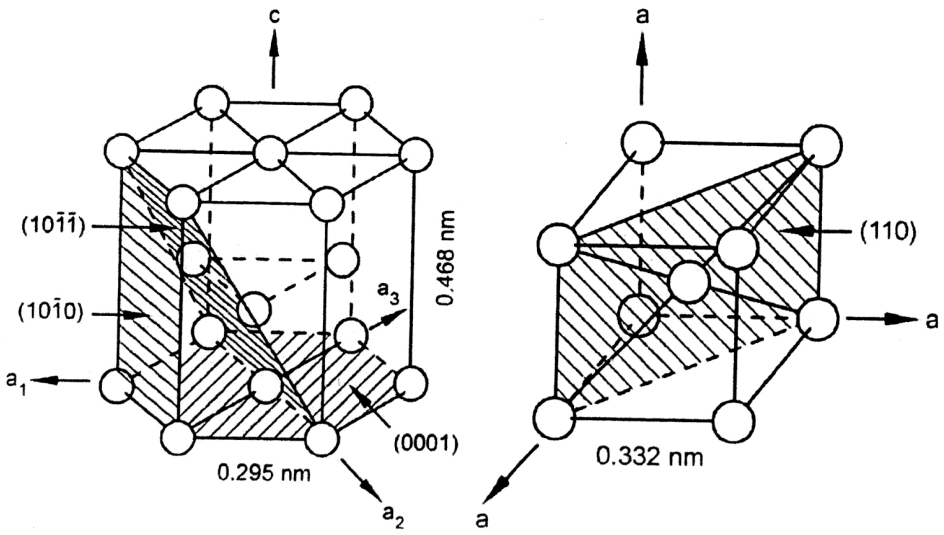

(a) hcp α Ti (b) bcc β Ti

Figure 1.4: Crystal structures of the stable phases of titanium [41]

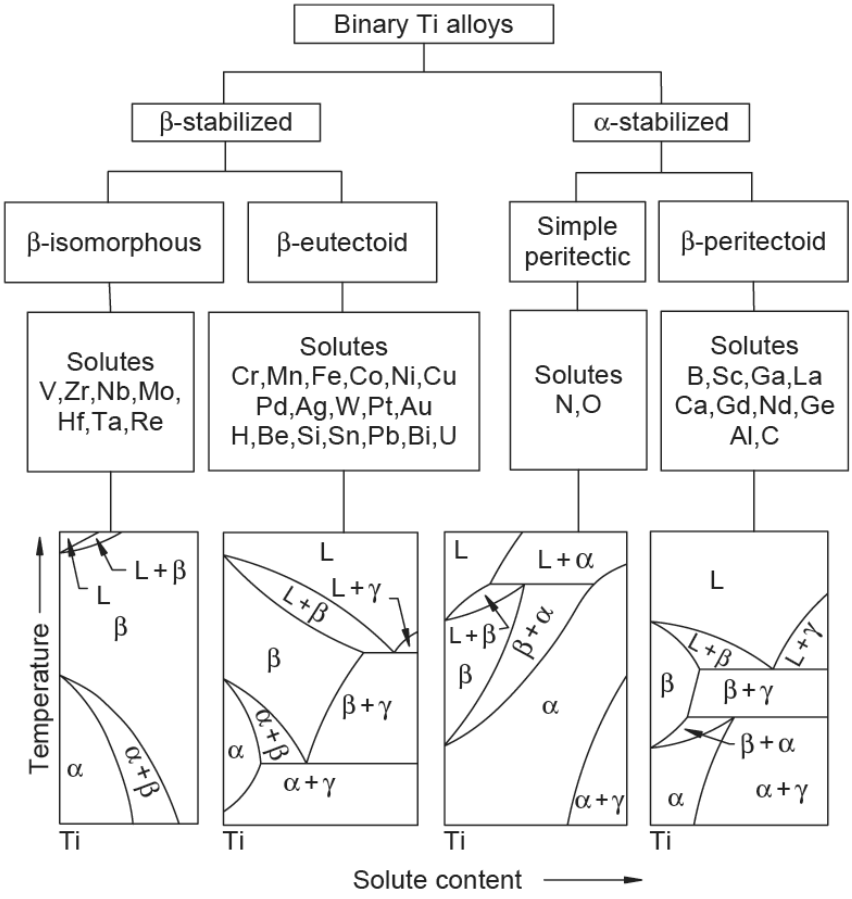

Figure 1.5: Classification of alloying elements in Ti alloys based on their influence on the equilibrium phase diagram[42]

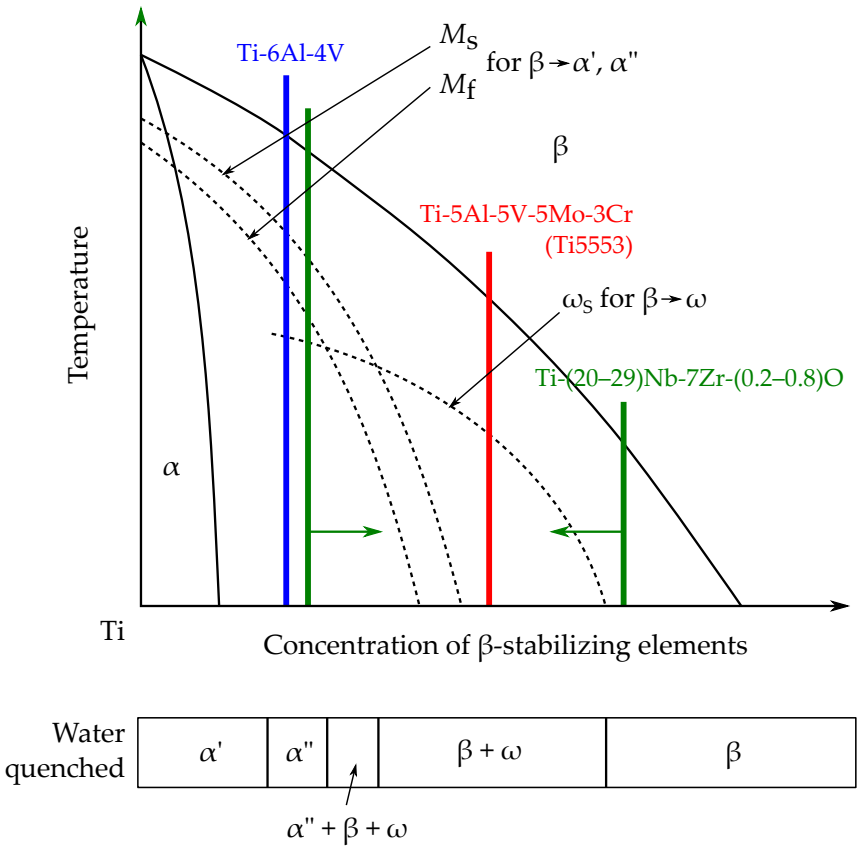

Figure 1.6: A schematic phase diagram of a general β-stabilized Ti alloy. The stable diagram is drawn in solid, important curves of the metastable diagram (M_s, M_f, ω_s) are drawn with dashed lines. Phases, which are found in the material after quenching from the β field, are plotted below the phase diagram. Schematic positions/ranges of the alloys investigated in the thesis are drawn in color.

lines correspond to the stable phase diagram, while the dotted lines mark the transition temperatures of the metastable transformations.

The martensitic transformation occurs in alloys cooled from the β region fast enough to suppress the diffusional precipitation of a stable α phase, when the temperature decreases below the M_s (martensite start) line (see Figure 1.6). The β phase becomes unstable, but the complete transformation to hexagonal α phase is not possible due to the presence of β-stabilizing alloying elements. The intermediate lattice has an orthorhombic symmetry and is called α'' martensite. The transformation is completed when M_f (martensite finish) temperature is crossed.

The ω phase is formed upon quenching from the β region at higher concentrations of the β stabilizers. The transformation is diffusionless, but not martensitic – its principle is a collapse of two of three neighboring {111} planes into their midplane. Domains up to several nm are formed and denoted as ω_{ath} (athermal ω). When the material is heated to a diffusion-allowing temperature, the ω_{ath} domains may be chemically stabilized by rejecting the β stabilizers, forming isothermal ω_{iso} phase [41, 42].

All Ti alloys are classified according to the phase composition upon quenching from the β field to the RT, as illustrated in Figure 1.6:

- α alloys, consisting of only stable α phase upon quenching
- $\alpha + \beta$ alloys, containing α'' martensite upon quenching
- metastable β alloys, which does not form α martensite upon quenching, but which may contain ω_{ath} and in which α phase can be precipitated
- stable β alloys

$\alpha + \beta$ alloys and metastable β alloys are the most important classes from the application point of view, since the precipitation hardening by α phase is one of the major strengthening mechanisms in Ti alloys and various microstructures can be prepared by thermomechanical processing. The three alloys, which were used in the thesis and which are marked in color in Figure 1.6, will be now briefly introduced.

1.3.1.1 Ti-6Al-4V Alloy

The workhorse Ti-6Al-4V alloy belongs to the group of $\alpha + \beta$ alloys. It is a high-strength low-cost Ti alloy with a widespread applications in aerospace industry[41], readily available in a powder form suitable for additive manufacturing, which can be performed industrially at standardized conditions. The alloy has a martensitic microstructure after printing, with a yield strength of $900 - 1000$ MPa. Detailed properties of the Ti-6Al-4V alloy are not a topic of the thesis and the reader is kindly referred elsewhere, e.g. [43].

1.3.1.2 Ti-5Al-5V-5Mo-3Cr Alloy

This standard and commercially available alloy is investigated in Chapter 5. It is usually abbreviated as Ti5553 (the composition is given in wt%) and belongs to the class of metastable β alloys, which have been available in aerospace applications since 1950s. The first application of β Ti alloys in a civil aircraft was the usage of Ti-10V-2Fe-3Al alloy in high-strength forgings of Boeing 777 [44], replacing the high-strength low-alloy steel and resulting in significant weight savings. However, the processing window of this alloy is relatively narrow and the microstructure is sensitive to small fluctuation is both temperature and strain rate [45]. The Ti5553 alloy was consequently developed by Boeing (on the basis of the Soviet VT22 alloy [46]) to overcome this disadvantage. The alloy offers larger processing window around the β transus temperature and exhibit higher strength than the Ti-10V-2Fe-3Al alloy. It has therefore become an alloy of choice for large structural components, such as landing gears [47]. It is currently used in Boeing 787 Dreamliner.

The β transus of the Ti5553 alloy is approximately 845 °C [47], depending on the precise chemical composition. According to [48], the alloy typically exhibit yield stress of 1055 MPa, ultimate tensile strength of 1159 MPa, maximum elongation of 9 % and a fatigue performance of 10^7 cycles at 800 MPa after hot isostatic pressing. It is an age hardenable alloy, strengthened primarily by precipitation of α particles in the β matrix. The mechanical properties are strongly influenced by the thermomechanical processing – the alloy can be worked in

the $\alpha + \beta$ region ($\sim$ 800 °C), quenched and aged for maximum strength or worked above the β transus, quenched and aged for maximum toughness [43].

The influence of heat treatment schemes on microstructure and mechanical properties was investigated quite intensively. When the Ti5553 alloy is quenched from the β field to RT, ω phase is formed [45]. Upon heating to 570 °C, α precipitates are noticeable after 90 s already. A similar Ti5553-1Zr alloy was aged at 300 °C to promote ω_{iso} formation before the final ageing at 600 °C [49]. The two-step ageing resulted in precipitation of extremely fine α particles, but the material was brittle, while the single-step ageing produced material reaching 9 % in ductility. The influence of the solution treatment of rolled samples (below/above β transus) prior to the final ageing was investigated in [50]. The best combination of strength and ductility was achieved for the material annealed below β transus + aged, resulting in globular α particles at GBs and fine lamellae in the grain interior. The ST above β transus + ageing resulted in significant grain growth, precipitation of lamellae at GBs and low ductility.

An ingenious method for high-throughput investigations of the ageing temperature influence was designed in [51]. The Ti5553 sample was cut into a truncated cone shape and heated by electrical current, resulting in a temperature gradient across the sample. Pseudospinodal decomposition of the β matrix was reported at 617 °C, resulting in very fine α precipitates.

Ti5553 was sintered with TiFeMo intermetallics by FAST with the aim of preparing a metal-matrix composite [52]. However, a partial dissolution of the TiMoFe occurred and tensile properties were not assessed, although the compressive yield stress increased from 1100 to 1300 MPa.

The in-situ ageing (without intermediate cooling to the RT) was tested in [53]. The Ti5553 alloy was prepared by selective laser melting (SLM) and in-situ aged by heating the baseplate to 500 °C. The material had columnar grains with a strong texture, reaching yield strength of $1000 - 1100$ MPa. Finally, Ti5553-1Zr alloy was prepared by FAST + in-situ ageing (without intermediate cooling) for 30 min at $600 - 750$ °C [54]. The authors used prealloyed powder of $100 - 200$ µm in diameter, which was then mechanically milled. The samples sintered from milled materials exhibited better tensile properties, reaching 1230 MPa yield stress and 5 % of elongation for the sample aged at 600 °C

1.3.1.3 Ti-Nb-Zr-Ta-O System

These alloys are prospective for biomedical applications and are investigated in Chapter 6 of the thesis. Using metastable β Ti alloys for implant manufacturing was considered for more than two decades [55–61]. Biomedical Ti alloys are intended to replace the stainless steel and the aerospace Ti-6Al-4V alloy, which are still in a widespread use. The alloy development is driven mostly by the endeavor to suppress the stress-shielding effect.

The stress-shielding occurs when the implant, having high elastic modulus, is cemented in a bone which has relatively low elastic modulus. For comparison – Young's modulus of a bone is as low as 30 GPa, while the moduli of metallic materials are much higher (200 GPa for steels, $100 - 110$ GPa for Ti-6Al-4V) [58]. This difference results in the proportional increase of the load

on the implant and corresponding decrease of the load on the surrounding bone. The bone slowly deteriorates and after some time, a revision surgery may be necessary. When the implant modulus is decreased, this effect is less pronounced and the implant lifetime is increased. The state-of-the-art β Ti alloys reach moduli in the range of $50 - 90$ GPa [62], depending on the chemical composition. However, there is a trade-off between elastic modulus and strength of the alloy, in a sense that excessive lowering of the modulus leads to decrease of the yield strength as well. This limits the practical applicability of the alloys with the lowest modulus.

Another design consideration is a biocompatibility of the potential β-stabilizing elements. There are concerns about long-term exposure to the potentially hazardous elements, such as Al and V. It was shown that Nb, Zr and Ta may be used without any limits and Fe and Mo to a limited extent [61–63].

Last, but not least, is the aspect of the alloy competitiveness in terms of cost. This is a major problem of metastable β Ti alloys, which use expensive alloying elements such as Ta, Nb, Zr or Mo, moreover in relatively high concentrations. There is always a question whether the undoubtedly superior properties are worth the even more superior price.

In Figure 1.6, we have shown a schematic phase diagram of a Ti alloy where all alloying elements are merged and represented by a concentration of a generic β stabilizer. It is generally agreed that the elastic modulus reaches its minimum when the metastable β phase is at the verge of stability, i.e. as close to the martensite start (M_s) line as possible, while avoiding formation of the ω phase [64]. This optimization is typically done empirically, based either on the relative 'strength' of the β stabilizing elements (Mo equivalence [41, 65]), or on the empirical description of the electronic structure – a simple calculation of e/a (valence electrons per atom) ratio [64] or a more sophisticated Bo-Md diagram (bond order vs. mean d-orbital energy) [66, 67].

For a long time, oxygen was perceived only as a contaminating element leading to the alloy embrittlement in higher concentrations [41]. While this is true for α and $\alpha + \beta$ alloys, its concentration in β alloys can exceed 1 at.% without embrittlement, while the yield strength is significantly increased [68]. The oxygen influence on phase transformations is difficult to capture by the empirical methods described above, because oxygen, unlike most of other alloying elements, forms interstitial solid solutions (while the others form substitutional solutions). Therefore, the electron density, bond order and d-orbital energy calculations are meaningless and cannot be used for predictions.

Oxygen is classified as an α-stabilizing element [41], but this is assessed by its effect on the increase of the β transus temperature, which mostly plays role during diffusional phase transformations. However, it is a β-stabilizing element at the same time, which refers to its ability to suppress the martensitic $\beta \rightarrow \alpha''$ transformation during quenching from a single phase β region [69–71]. The exact mechanism is still not fully resolved and it is one of the hot topics in research of Ti alloys.

We have focused our attention on the Ti-Nb-Zr-Ta-(O) system, as the most promising one. The studied alloy composition range is plotted in the schematic phase diagram in Figure 1.6 (green lines) to show what phases can be expected. The outstanding biocompatibility and low Young's modulus of the Ti-Nb-Ta-

Zr (TNTZ) alloy was demonstrated already in late 90s [55, 72]. More recently, it was shown that alloying Ti-35.3Nb-5.7Ta-7.3Zr with oxygen up to 0.7 wt% results in a significant increase of the yield strength (from 447 to 1017 MPa), while maintaining the ductility and increasing the elastic modulus only little (from 63 to 80 GPa) [56, 60, 73]. Alloying with 2 wt% of Fe and 0.25 wt% of Si was also investigated in [73], but the yield stress increase was smaller (587 and 629 MPa, respectively). Alloys with both Fe/Si and O additions did not exceed the properties of the alloy with O addition only.

It was shown recently in [74] that Ta can be omitted in the TNTZO alloy, without compromising its strength and elastic modulus. This can significantly reduce the alloy cost, as Ta is the most expensive alloying element. However, this also shifts the β stability of the alloy and the optimization of the composition must be performed again. Due to the oxygen modelling issues described above, the optimization must be carried out experimentally.

1.3.2 Ti/Ti-6Al-4V – Al6061 Composites

The preparation of architectured Ti-Al composites is investigated in Chapter 4 of the thesis. Composite materials consist of two or more dissimilar constituents, which should, in their synergy, exhibit better properties than each of the constituents individually [75]. The term 'architectured composites' then refers to a composite consisting of an inner reinforcement of one material and surrounding matrix of the other material. The reinforcement is a tailored (architectured) inner structure, typically at the length scale of the specimen (i.e. not at the micrometer scale, common for particle-reinforced composites) [76]. Additive manufacturing is a great method for the reinforcement manufacturing, as it provides a freedom of shape, which can be designed to meet the specific mechanical demands.

The idea of manufacturing an architectured composite by FAST from an architectured lattice pre-manufactured by AM and a powder matrix was inspired by [77], preparing a CP Ti + Ti-6Al-4V by consequent use of electron beam melting (reinforcement lattice) and FAST. Similar experiment was per-

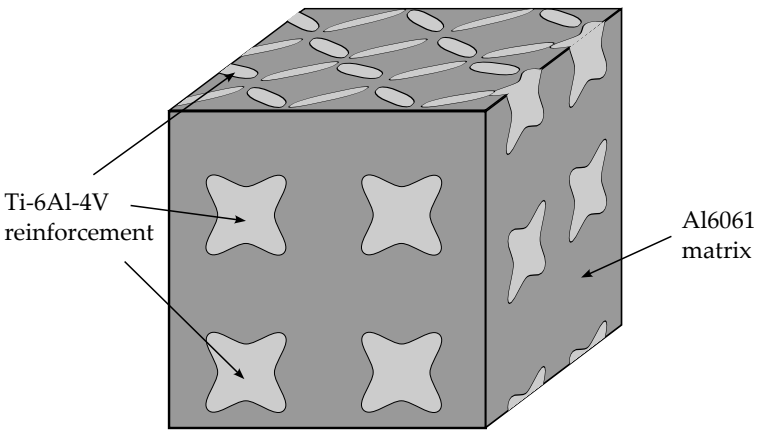

Figure 1.7: An illustration of the architectured composite with the reinforcement lattice and the surrounding matrix marked.

Table 1.1: Basic properties of the materials used for the sintering of the architectured composites. σ_{02}^{RT} and σ_{02}^{550} stand for the yield strength at the RT and the sintering temperature, respectively.

Material	σ_{02}^{RT} (MPa)	σ_{02}^{550} (MPa)	E (GPa)	ρ (g/cm^3)	Source
Ti Grade 2	400–500	~ 100	105	4.51	[43, 83]
Ti-6Al-4V	1000	~ 600	114	4.43	[43, 84]
Al6061	276	< 10 (extrapolation)	69	2.70	[85]

formed recently [78], combining AM of lattice reinforcement with the FAST-forge method (both reinforcement and matrix were made of Ti-6Al-4V). Some other examples include 3D printing of Inconel 718 + CoCr composite [79], sintering of tungsten powder with a zirconia coated tungsten mesh able to withstand high heat fluxes [80], or FAST sintering of Ti with AZ91 Mg alloy, reaching bonding efficiency (ratio of the composite strength to the Mg alloy strength) of 96 % [81]. Finally, interpenetrating Mg (matrix) + NiTi (reinforcement) composites with high strength and damping capacity were manufactured by pouring molten Mg into the additively manufactured NiTi lattice [82].

An Al6061 alloy was selected as a material for the matrix, while commercially pure Ti (Grade 2) and Ti-6Al-4V alloys were used as a reinforcement. The basic properties of the materials are presented in Table 1.1.

The Al6061 (Al-1Mg-0.6Si-0.3Cu-0.2Cr, wt%) alloy is a general purpose, age-hardenable aluminium alloy with a solidus temperature of 582 °C [85]. The typical heat treatment (denoted as T6 temper) consists of the solution treatment at 530 °C, water quench, ageing at 160 °C for 18 h and air cool. The typical yield strength is 55 and 276 MPa in the solution treated and T6-aged condition, respectively [85]. It is a workhorse Al alloy, easily obtainable in the powder form.

The commercially pure titanium (Grade 2) and the Ti-6Al-4V alloy (wt%) was chosen as a testing material for the proof-of-concept sintering. Ti-6Al-4V (wt%) alloy is the most used $\alpha + \beta$ Ti alloy for AM and can be deposited by selective laser melting using a standardized set of parameters. The large difference of the yield strength at the sintering temperature (σ_{02}^{550} in Table 1.1) is desirable, because the Al powder can be then mechanically pressed into the Ti matrix, which, on the other hand, should not deform.

The linear thermal shrinkage of all three materials is plotted in Figure 1.8, along with the relative shrinkage. The shrinkage is calculated with respect to the sintering temperature, because the thermal stresses matter only in the material after consolidation. The Al shrinks more than Ti during cooling, resulting in a compressive stress acting on the reinforcement as a whole.

Manufacturing of metallic cellular structures was investigated in multiple papers. In general, the selected lattice geometry should be designed according to the expected loading regime [87]. Al-Ketan et al. [88] prepared lattices from

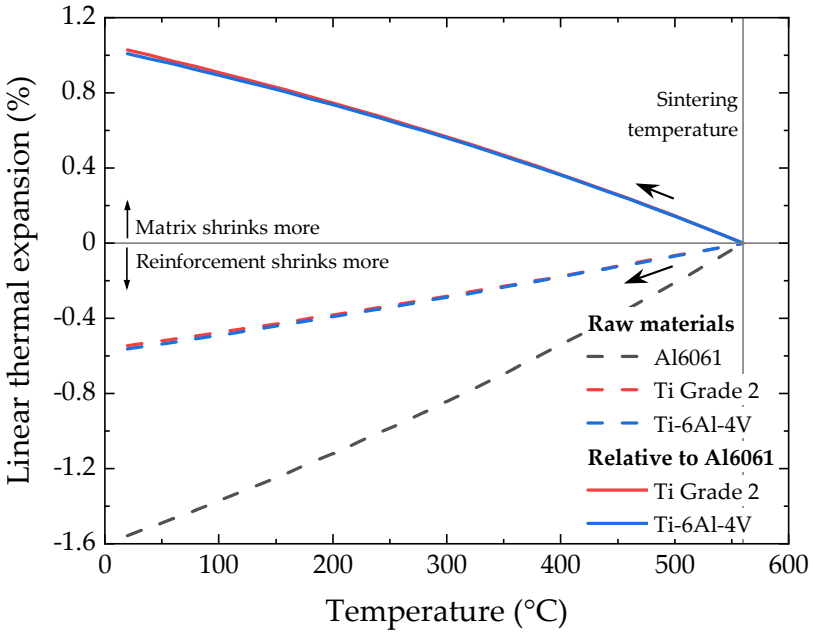

Figure 1.8: Comparison of thermal expansion/shrinkage of the used materials during cooling from the sintering temperature. The raw material data (dashed lines) were used for calculation of the thermal shrinkage relatively to the Al6061 matrix (solid lines). Data source: [86]

maraging steel of several different geometries and performed compression test to assess their mechanical response in terms of strength and toughness. However, the fatigue strength and ductility were compromised by the high surface roughness of the as-built lattice. Several methods were used to overcome this problem in the Ti-6Al-4V cellular structure [89]: hot isostatic pressing, sandblasting, polishing and etching. Etching in the Kroll solution was found to improve the mechanical properties and also improve the cell proliferation on the surface. Similar results were achieved in [90], where the surface roughness of Ti-6Al-4V was lowest after etching in HF solution. For us, achieving the low surface roughness of the lattice, resulting also in lower overall surface area of the reinforcement, is important even more, since it can affect the formation of the intermetallic layer at the interface between the lattice and the matrix.

1.3.3 Refractory Complex Concentrated Alloys

Conventional alloys are usually based on one or two principal elements, whose basic properties are then modified by alloying elements. This includes steels, Ti alloys, brasses and bronzes etc. The concentration of alloying elements can reach tens of percent in high performance alloys (stainless steels, Ni superalloys, biomedical Ti alloys,...), but one element is still dominant. Investigation of alloys based on a single dominant element leaves out a large portion of the available concentration space unexplored. If we use a naval analogy (as illustrated in Figure 1.9), this is like exploring only the coastal waters close to the safe harbors of pure elements.

The paradigm of using one or two dominant elements was overcome in 2004 by Cantor and Yeh, who were the first to sail out to the high seas of what

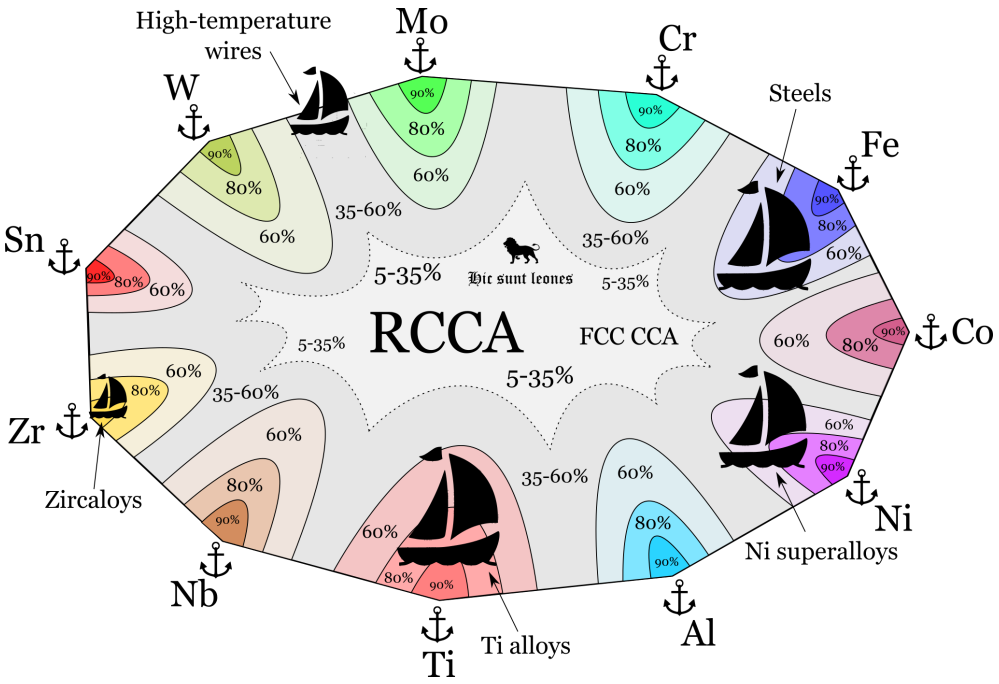

Figure 1.9: An artistic illustration of a vast compositional space. The locations of explored alloying systems are shown. The RCCAs can be found far from the 'coastal waters' in the vast unexplored 'ocean'. Drawing by Dalibor Preisler.

we now call *high-entropy alloys* (HEAs) or *complex concentrated alloys* (CCAs) [91–93]. They prepared a single-phase fcc equimolar CoCrFeMnNi alloy and provided the first theoretical description promoting a role of configurational entropy in the alloy stability, hence called HEAs.

The underlying idea is that a large number of elements in comparable molar fractions increases the configurational entropy of the random solid solution, stemming from the $S_{\text{conf}} = R \sum_i x_i \ln x_i$ term, decreases Gibbs energy of the alloy and makes the solid solution more stable. Such alloy would then exhibit a high strength (due to an extensive solid solution strengthening), while maintaining good ductility (due to fcc structure). However, this calculation holds only for the elements with low enthalpies of mixing. In case that the enthalpy is high for some combination elements, clustering is favored and the configurational entropy decreases. This is especially valid for CCAs, because more elements involved means higher probability of finding a suitable pair with high enthalpy of mixing [94]. The 'high entropy' concept and naming is therefore questioned. Nevertheless, a significant portion of the research in the CCA field is still in pursuit of utilizing high configurational entropy to achieve single-phase bcc or fcc CCAs.

Refractory complex concentrated alloys (RCCAs) differ from the Cantor-based fcc CCAs by element selection (Ti, V, Cr, Nb, Zr, Mo, Hf, Ta, W and Al are the most commonly used) and the resulting crystal structure of the disordered phase, which is bcc, as most of the elements are bcc metals [95]. Their practical aim of developing RCCAs is to potentially replace the currently used Ni superalloys in high temperature applications, such as jet engines or fusion reactors, where even a minor increase of the service temperature greatly improves the efficiency. While the high-temperature strength of some RCCAs is

already superior to Ni superalloys [96, 97], the room temperature ductility is typically poor, which limits the handling of the parts and thus the application.

One of the research interests within RCCAs are Al-Nb-Ta-Ti-V-Zr based alloys, which were reported to have a superalloy-like microstructure consisting of bcc/B2 cuboidal phases [98]. This could serve as a great starting point for the optimization of the alloy microstructure – phase fraction and morphology. However, there comes the general challenge of CCA design – the sheer vastness of the compositional space, which grows exponentially with the number of elements involved.

A general approach is to use CALPHAD modelling to narrow the search first and then do the final optimization experimentally. For conventional alloys with a huge amount of data available (such as steels), the predictions can be quite accurate, while for CCAs (and even more RCCAs), the data are simply not available yet. The Gibbs energies are usually assessed using the binary and ternary systems only, but more complex interactions of elements are possible in multicomponent CCAs [95]. A typical fail of CALPHAD is a theoretical prediction of a single bcc phase instead of a mixture of bcc and ordered B2 phases observed experimentally [95]. Therefore, new experimental data are needed, as pointed out by Miracle and Senkov [94]:

> *"A desperate need exists for high quality phase diagrams in ternary and higher order refractory metal systems, including Al. Many decades ago, phase diagram studies were considered important contributions to basic science, but they seem to have fallen out of favour by research proposers and funding agencies alike. This trend needs to be reversed. Experimental phase diagrams are an essential starting point to guide compositional studies and to build thermodynamic models of ternary and higher order B2 phases."*

Because of the size of the compositional space, the sample design must be optimized for obtaining as much information as possible with the least effort (in terms of time, labor and resources) [99]. For this purpose, high-throughput methods need to be used. The use of powder metallurgy, namely FAST, can provide invaluable tool for high-throughput characterization and alloy development as described in this thesis.

2 Aims of the Thesis

The main objective of the thesis is to explore the capabilities of FAST beyond its common applications. The following areas will be explored:

1. Preparing an architectured composite consisting of additively manufactured cellular structure and a powder-based matrix (Ti/Ti-6Al-4V + Al6061).

2. Manufacturing a sample sufficiently large for standard-sized tensile testing using blended elemental powders in a single run, including the ageing treatment (Ti-5Al-5V-5Mo-3Cr aerospace alloy).

3. Preparing homogeneous and compositionally graded alloys from blended elemental powders for fast assessment of the phase stability across the range of compositions (Ti-xNb-7Zr-yO biomedical alloy system).

4. Preparation of a heterogeneous sample containing several refractory complex concentrated alloys, providing experimental data for construction of the phase diagrams (Al-Ti-Ta-Nb-Zr system).

Finally, promising capabilities of FAST, deserving further attention and exploitation, will be identified.

3 Experimental Methods

Basic details about the FAST furnace used for the sample preparation are provided in this chapter, as well as an overview of the employed characterization techniques and methods. The material-specific preparation details are provided at the beginning of each Chapters 4 to 7 individually.

3.1 Field-Assisted Sintering Technology

The sintering was performed at the Institute of Plasma Physics of the Czech Academy of Sciences using SPS 10-4 furnace by Thermal Technology LLC. All sintering was performed in vacuum of the order of 1 Pa, although sintering in an inert of reducing atmosphere can be performed as well. The furnace can deliver max. 4 kA of electric current (the maximum achievable heating rate is dependent on the sample being sintered). The temperature can be controlled by two methods: by a thermocouple (K or C type) placed in a drilled hole in the bottom punch or by a pyrometer focused into the hole in the side of the die (see the drawing in Figure 3.1).

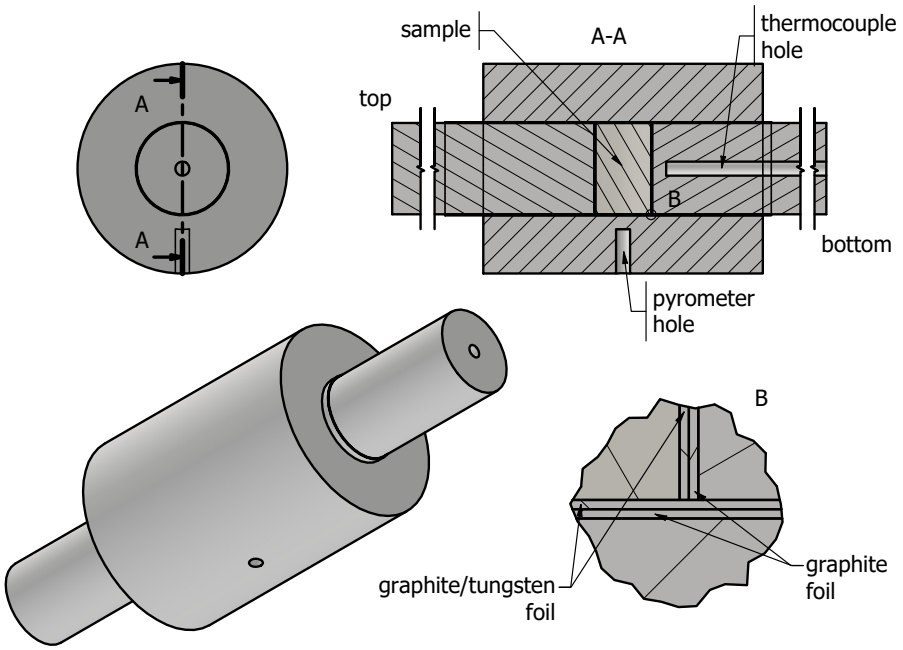

Figure 3.1: A schematic drawing of the FAST die assembly for a typical sintering run.

The die and punches are made of graphite, with graphite foils separating the sintered sample from the tooling. Tungsten foil is used instead in some cases (high-temperature sintering experiments), in which the carbon from the foil would diffuse into the sample and contaminate it.

3.2 Carrier Gas Hot Extraction

The carrier gas hot extraction (CGHE), also known as inert gas fusion, is a standard analytical technique used for measuring content of light elements O, N and H.

The method is based on melting the specimen under a stream of an inert gas (argon, helium or nitrogen is used) in a graphite crucible [100]. The measured elements are evolved in a gaseous form and react with themselves and with the crucible, which is continuously flushed by the inert carrier gas into the detector section. The content of the reaction products is measured using a series of detectors: at first, oxygen is catalytically converted to CO, which is then measured using infrared absorption detector. The oxides are then captured and the content of the remaining N_2 and H_2 is determined by a thermal conductivity detector with a pure carrier gas as a reference. The raw detector signals are recalculated to the actual content using calibration standards of a known composition.

Measurements were done using three different devices, as their availability was changing during the thesis preparation. These were LECO ONH836 at TU Bergakademie Freiberg, LECO TC 500C at ORLEN Unipetrol RPA and finally Bruker G8 Galileo available at the Department of Physics of Materials since 2022.

3.3 Electron Microscopy

Scanning electron microscopy (SEM) was employed throughout the thesis as a key imaging technique. Two devices were used: Zeiss Auriga Compact CrossBeam, equipped with a focused ion beam (FIB) system for cross-sectioning and lamellae preparation, and FEI Apreo for unparalleled imaging performance. Both microscopes were equipped with field-emission guns as electron sources and energy dispersive X-ray spectroscopy (EDS) detectors for chemical analysis. Several basic types of signals can be detected, each of them providing different information about the sample.

Secondary electron (SE) signal is broadly used for the purpose of general imaging in various applications. Secondary electrons are ejected from the electron shell of the sample atoms by inelastic scattering events with the primary electrons. They have low energy ($< 50\,\mathrm{eV}$), come from a low depth of the sample and their yield is sensitive to the topography of the specimen surface, with edges bright and corners dark, providing a feel of natural illumination, hence the usage in general imaging.

For material science, backscatter electrons (BSE) are arguably more important than secondary electrons. These are the electrons of the primary beam

which were scattered (both elastically and inelastically) out of the specimen. Because the scattering is more intensive on heavier atoms, backscatter electrons carry information about the local chemical composition of the specimen (called *composition* or *Z contrast*). Furthermore, the scattering intensity is influenced by a local lattice orientation, giving the *orientation* or *channeling contrast*. If the sample is intentionally tilted into orientation, in which the grain appears dark, even small deviations from the perfect crystallinity, such as dislocations or secondary phases with weak channeling contrast, can be observed. This technique is similar to dark-field imaging in transmission electron microscopy and called *electron channeling contrast imaging* (ECCI) [101].

The site-specific samples for further investigations by transmission electron microscopy (TEM) were prepared using a focused ion beam (FIB) system. FIB is a micromachining tool inside the scanning electron microscope, using high-energy Ga ions to mill the specimen and prepare a thin lamella, which can be then extracted by a micromanipulator and placed on a grid for further transport.

Transmission electron microscopy (TEM) was used in Chapters 4 and 6 for resolving structures beyond the resolution of the scanning electron microscope and for the identification of their crystal structure, size and morphology by selected area electron diffraction (SAED). JEOL 2200FS microscope, equipped with energy dispersive X-ray spectroscopy (EDS) and capable of working in the scanning transmission electron microscopy (STEM) regime was used.

During interactions of primary electrons with the specimen atoms (both in SEM and TEM), X-rays are also emitted – a continuous spectrum of braking radiation and a discrete spectrum consisting of characteristic emission lines of the specimen atoms, which can be used for an analysis of the specimen chemical composition by means of energy- or wave- dispersive X-ray spectroscopy.

Energy dispersive X-ray spectroscopy (EDS) is based on measuring the *energy* spectrum of the photons impinging the semiconductor detector. The peaks are then matched to known emission lines of the elements of interest and an integral intensity for each peak is calculated. The relative intensities of the peaks can be then quantified by comparing them with the spectra of standards with known composition (more accurate method, but less commonly used) or by a standardless approach, assuming that a pairwise ratios of concentration are equal to pairwise ratios of peak integral intensities on which a so-called *ZAF correction* is applied (it includes correction factors for the specimen average atomic number Z, absorption A and fluorescence F). This method is slightly less accurate, but much faster and easier to use, making it a prevailing microanalysis technique. The EDS measurement is quick, which allows line profiling and mapping, on the other hand the detected peaks are relatively broad ($\sim$ 100 eV) and can overlap for some elements (e.g. O Kα with Ti Lα and V Lα, Zr Lβ with Nb Lα, etc.). The overlapped peaks are then difficult to deconvolute, decreasing the absolute accuracy of the quantification. On the other hand, the relative accuracy (i.e. point-to-point concentration differences and trends) are affected to a lesser extent and thus more reliable. EDAX Octane Elite detector was used for EDS measurement in the thesis, processing of the measured data was done using vendor-provided APEX software with eZAF (enhanced ZAF) correction.

In the wave dispersive X-ray spectroscopy (WDS), the collimated X-ray beam coming from the specimen is diffracted on a grating and the intensity is measured as a function of an angle (and thus the photon wavelength). WDS provides much narrower peak (in order of eV), but at a cost of significantly longer acquisition times, effectively barring line profiling and mapping. Also, calculating the concentrations is possible only using standards, as the measurement is more device-specific and no standardized corrections (as ZAF for EDS) are available. WDS analysis was performed at the Institute of Petrology and Structural Geology, Charles University, using JEOL JXA-8530F microanalyzer.

3.4 X-Ray Diffraction

The X-ray diffraction (XRD) was used for identification of phases in bulk materials in a transmission geometry, using a Rigaku Rapid II diffractometer operated at 50 kV, equipped with Mo Kα radiation source. We have used a curved 2D image plate detector, resulting in a higher total signal and better detection of weak diffractions peaks.

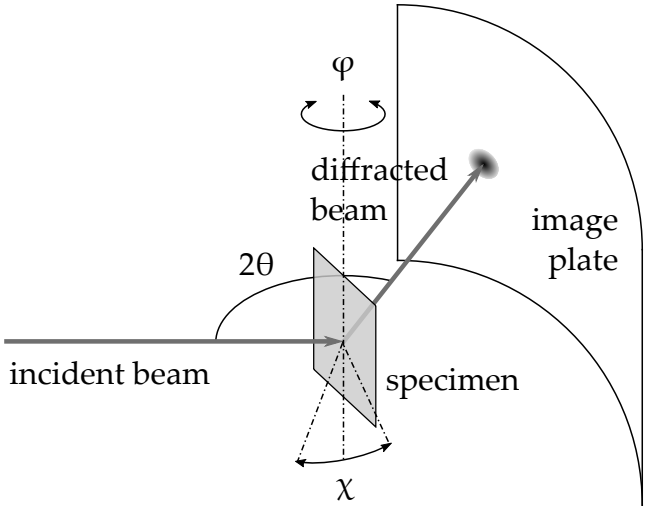

Figure 3.2: The XRD experimental setup in a transmission configuration

Thin samples of approximately $300 - 400\,\mu m$ in thickness were used for the measurements. The specimen was placed in a goniometer with motorized axes, the parallel incident beam, having 0.3 mm in diameter, was aimed onto an eucentric position and the specimen is oscillated in ϕ axis ($\pm 20^\circ$) and χ axis ($\pm 15^\circ$) during the measurement. This allowed us to scan larger portion of the reciprocal space, i.e. bring more grains into the diffracting position. The resulting 2D diffraction patterns/rings were then processed into 2θ vs. intensity diffractograms by azimuthal integration.

3.5 Mechanical Testing

Three methods of mechanical testing were employed in the thesis – microhardness measurements, tensile testing and a three-point flexural test. Acoustic

emission and digital image correlation were used as supplementary methods for more thorough analysis of the three-point flexural test. Finally, resonant ultrasound spectroscopy was used to measure elastic constants.

3.5.1 Microhardness

This method was used in Chapters 5 and 6. It provides information about local hardness / strength of the material. It is fast, easy to use and allows mapping of the hardness across the specimen.

The method is based on measuring a trace size of a specified indenter pushed into the material under a given load. A pyramidal Vickers indenter was used in the thesis.

An automatic microhardness measurement device Qness 10A was employed in the thesis, using HV0.5 method (0.5 kgf load).

3.5.2 Tensile Testing

Tensile testing was used in Chapter 5. It is a standard method for measuring ductility, yield strength and ultimate tensile strength of materials. Engineering stress and strain are calculated from the force measured by a load cell in the crosshead and from the specimen elongation from the initial length. Considering the change of the specimen cross-section, true stress and true strain should be used to evaluate the geometry independent properties of the material.

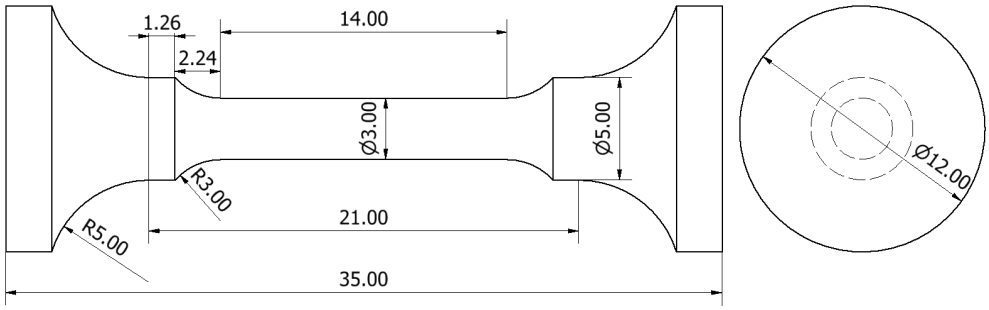

Figure 3.3: A circular specimen geometry for the tensile testing of Ti5553 alloy. All dimensions are given in millimeters.

Yield stress is determined as a stress necessary to plastically deform the material to the true plastic strain of 0.2 %. Material ductility is determined as a true strain at failure.

A circular specimen geometry was used, drawn in Figure 3.3. The specimens were prepared by turning and the surface was polished using #2000 grit sandpaper as a final step before deformation. The tensile testing was performed using an Instron 5882 universal testing machine at the constant strain rate of $10^{-3}\,\mathrm{s}^{-1}$.

3.5.3 Three-Point Flexural Test

This method was used in Chapter 4 and it is commonly also referred to as a three-point bending (3PB). The test geometry is illustrated in Figure 3.4. The

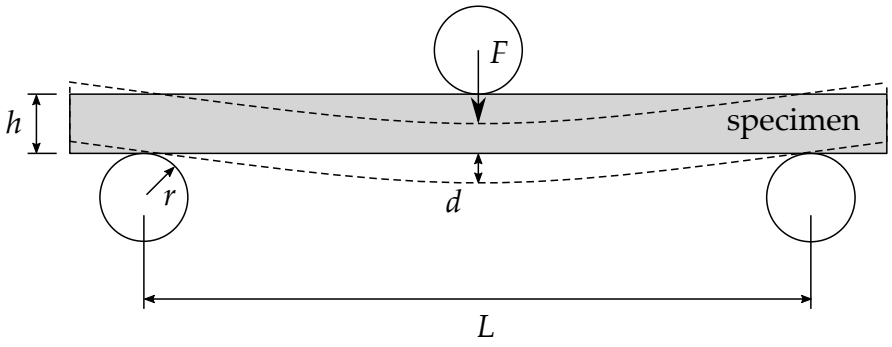

Figure 3.4: Geometry of the three-point flexural test

specimen, a rectangular beam of the height h and width w, is placed on two cylindrical pins of a radius r and having length span L. The specimen is loaded by a third cylindrical pin in the middle between the supporting beams. Load F and the deflection d is registered during the experiment.

For small deflections, tensile stress σ and strain ϵ are calculated for the bottommost layer (called outer thread) of the specimen according to the following formulae:

$$\sigma = \frac{3FL}{2wh^2}$$

$$\epsilon = \frac{6dh}{L^2}$$

The three-point bending was carried out at the Instron 5882 universal testing machine with a dedicated fixture for small specimens. The support length span was 8 mm with a 0.25 mm pin radius. The rectangular specimen dimensions were 2 mm × 1 mm × 20 mm ($w \times h \times$ length). The test was performed at a constant strain rate of $2 \times 10^{-3}\,\mathrm{s}^{-1}$ (0.002 mm/s).

3.5.4 Acoustic Emission

This method was used as complementary to the three-point bending in Chapter 4. Acoustic emission (AE) refers to the elastic waves in a material created by sudden localized deformation events [102]. These include a release of stress during collective movement of dislocations, twinning or a crack propagation. These waves can be subsequently detected on the surface of the specimen by an ultrasound piezoelectric sensor. As such, AE is generally assigned to non-destructive testing methods and can be used, e.g., for investigations of structural damage in civil engineering.

The signal from the piezoelectric sensor is amplified and electronically processed. There are several methods of the signal analysis, out of which a simple parameter-based approach [103] is used in the thesis. The incoming signal is monitored and when its amplitude exceeds a given threshold, it is recorded as an AE event. A typical waveform of such event is illustrated in Figure 3.5. Each event is then characterized by its timestamp, amplitude, energy, duration

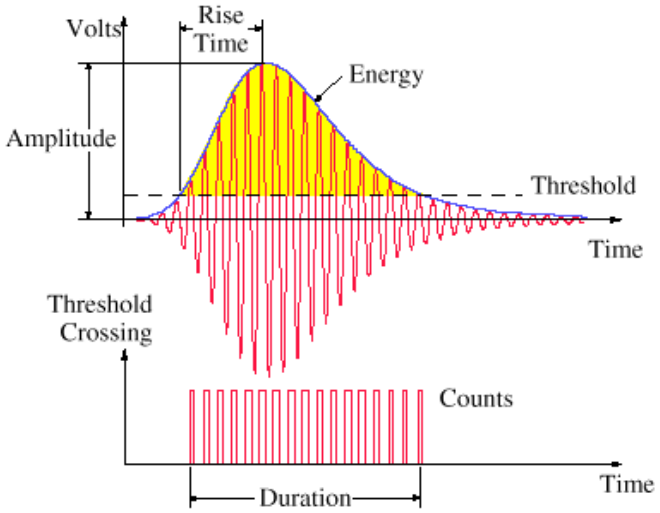

Figure 3.5: A typical waveform of an acoustic emission event and its parameters [103]

and rise-time. These events can be subsequently correlated with the deformation curve and time intervals of a high acoustic emission activity (i.e. intervals of high slip activity or cracking) can be traced.

The AMSY-6 computer-controlled AE system with the ASIP-2 signal processor (Vallen Systeme GmbH) was employed for the raw AE data acquisition at the sampling rate of 2 MHz. The Micro-80S AE sensor (Physical Acoustic Corporation) was used coupled to the Vallen AEP5 preamplifier having a 40 dB gain. The sensor was attached to the lower steel block with the supports using a plastic clip, a good acoustic contact was facilitated by the Apiezon M vacuum grease. By this, identical testing conditions (especially the acoustic 'contact' and signal path) were maintained for all the specimens. The AE activity was evaluated by means of the cumulative evolution of AE counts, i.e. the number of data points exceeding the threshold level (21 dB_{AE}, slightly above the background noise level).

3.5.5 Digital Image Correlation

This method was employed along with the AE as complementary to the 3PB in Chapters 4. Digital image correlation, usually abbreviated as DIC only, is used to determine local strain fields at the surface of the specimen during deformation.

A digital camera takes images of the specimen surface (patterned by a conventional black paint spray) in regular time intervals during the test. After the test is finished, the images are subdivided into small windows and a transformation matrix is calculated for each time interval in all windows. The strain component of this transformation matrix then corresponds to the local strain at the specimen surface.

Image recording was performed using the high-speed camera PHOTRON FastCam Mini WX100 and the Nikon 60 mm f/2.8 G ED AF-S Micro lens. The acquisition rate was 50 fps and the image resolution was 1536 px × 416 px (reduced from the default 2048 px × 2048 px to increase the available recording

time while still capturing the entire area of interest). The images were processed utilizing the commercial Dantec Dynamics Istra4D (v4.4.6) DIC software. For the analysis, the facet size was set to 27 px, the grid spacing was 13 px, and the other parameters were kept default.

3.5.6 Resonant Ultrasound Spectroscopy

The resonant ultrasound spectroscopy (RUS) method is used for measurements of elastic constants in Chapter 6 with higher precision than available from the deformation tests.

Free vibrations are generated in a rectangular specimen having dimensions 3 mm $\times$ 4 mm $\times$ 5 mm by an infrared pulsed laser focused on the sample bottom surface. The vibrations are then registered at the top surface by a scanning laser vibrometer, which can be then recalculated to the spectrum of resonant frequencies. The elastic constants are determined by an inverse method – by iterative fitting of the spectrum calculated from the unknown elastic constants to the measured spectrum [104].

The measurement was undertaken at the Institute of Thermomechanics of the Czech Academy of Sciences on an in-house built device using Quantel ULTRA Nd:YAG laser as a vibration source and Polytec Micro System Analyzer MSA-600 laser vibrometer.

4 Architectured Titanium-Aluminum Composites

This chapter was inspired by a paper [77], presented at the Euromat 2017 conference in Thessaloniki, investigating the coupling of electron beam melting and spark plasma sintering by sintering a 3D printed Ti-6Al-4V lattice with Ti Grade 2 matrix. We wanted to explore the idea even further – to investigate a possibility of joining dissimilar materials, namely a Ti or Ti-6Al-4V lattice with an Al6061 matrix.

4.1 Material Preparation

Materials

The prealloyed powder of the Al6061 alloy was supplied by TLS Technik. Its composition, as taken from the supplier's datasheet, is presented in Table 4.1. The powder was prepared by gas atomization method, the particles have spherical shape with the size distribution of $10 - 45\,\mu m$ in diameter.

Simple titanium wires were used instead of the 3D printed lattice for the proof-of-concept sintering and for the investigations of the interface between Ti and Al. Ti Grade 2 and Ti-6Al-4V wires having 0.5 mm in diameter were supplied by Inkosas.

In the next step, the lattice was prepared by selective laser melting (SLM) at VSB – Technical University of Ostrava (VŠB-TUO) from Ti-6Al-4V ELI (extra low interstitial) powder. The laser was operated at 150 W, with the scanning speed of 1200 mm/second and the layer height of 20 µm. The octahedral unit cell is shown in Figure 4.1a. Size of the cell is 1 mm × 1 mm × 1 mm with the designed strut thickness of 200 µm (this is about the minimum thickness

Table 4.1: Chemical composition of the Al6061 alloy according to the supplier's datasheet

	Si	Mg	Fe	Cu	Cr	Ti	Mn	Zn	Al
wt%	0.75	0.93	0.30	0.33	0.21	0.01	0.05	< 0.002	bal.
at.%	0.72	1.04	0.15	0.14	0.11	0.01	0.02	< 0.001	bal.

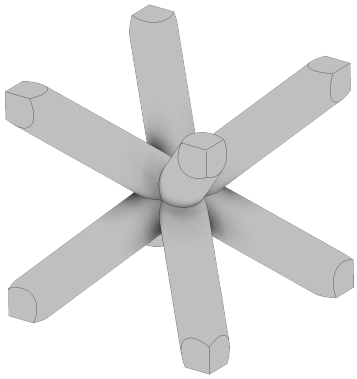

(a) A unit octahedral cell ($1 \times 1 \times 1\,\mathrm{mm}^3$)

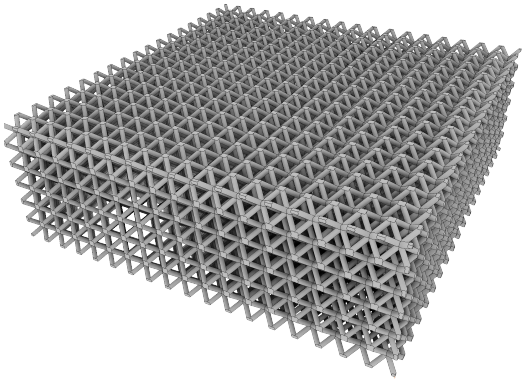

(b) The whole lattice model ($18 \times 18 \times 6$ unit cells)

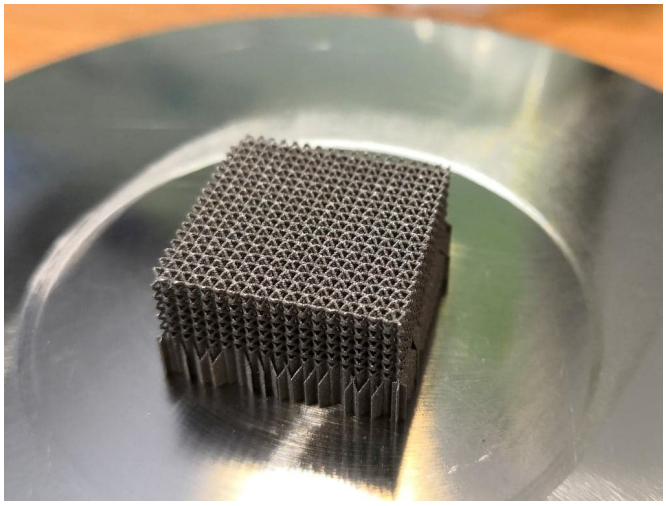

(c) The as-built lattice (photo by Jiří Hajnyš, VŠB-TUO)

Figure 4.1: The reinforcement lattice drawings and the result

achievable by SLM). The whole model consists of $18 \times 18 \times 6$ cells, as shown in Figure 4.1b. This geometry corresponds to the theoretical volume fraction of 17.8 %. Figure 4.1c then shows the actual as-built lattice.

Unlike the plain wire used for the proof-of-concept sintering, the surface roughness of the as-build lattice is very high, with non-melted particles attached to the structure (see the Figure 4.10a below in the Results section). To investigate the influence of the roughness on the sintering process and interface quality, one lattice was etched using Kroll etchant (3 % $HF + 6\,\%$ HNO_3 solution in water) for 2 min at room temperature prior to the sintering.

Sintering

The die was first filled with a layer of Al6061 powder, then the wire or the lattice were inserted and the die was topped with additional Al6061 powder. The sintering program was designed with following considerations:

1. Temperature must be high enough to promote diffusion between Al matrix and Ti reinforcement.

2. Temperature must be below the solidus temperature of Al6061 alloy (582 °C, [85]).

3. Temperature should be above the solvus temperature of intermetallic phases (see Figure 4.2a).

4. Piston pressure should be low and applied slowly to limit the deformation of the lattice.

The filled die was preloaded with a pressure of 2.5 MPa. The sample was heated at the rate of 50 K/min to 560 °C, followed by a 10 min dwell. The piston pressure was then increased to 10 MPa during the beginning of the dwell at the rate of 1 MPa/min. After the dwell, the sample was cooled to the room temperature. The sample cannot be cooled actively, only via partial heating i.e., only the minimum cooling rate can be limited. In this case, the cooling rate was set to 50 K/min, which slowed the cooling during the first few minutes. The process parameters acquired during the sintering are plotted in Figure 4.2.

The sintered samples were then cut and mechanically ground and polished. Due to difficulties with preparing a high-quality surface on a sample consisting of two dissimilar materials, ion polishing was employed as a final step, using Leica EM RES102 system.

Heat Treatment

A subset of specimens sintered with the lattice was heat treated to reach the maximum strength of the Al6061 matrix prior to the mechanical testing. A standard heat treatment program, denoted as T6 [105] was applied, consisting of two steps: solution treatment at 530 °C for 30 min, followed by a water quench, and ageing at 160 °C for 18 h, followed by air cooling.

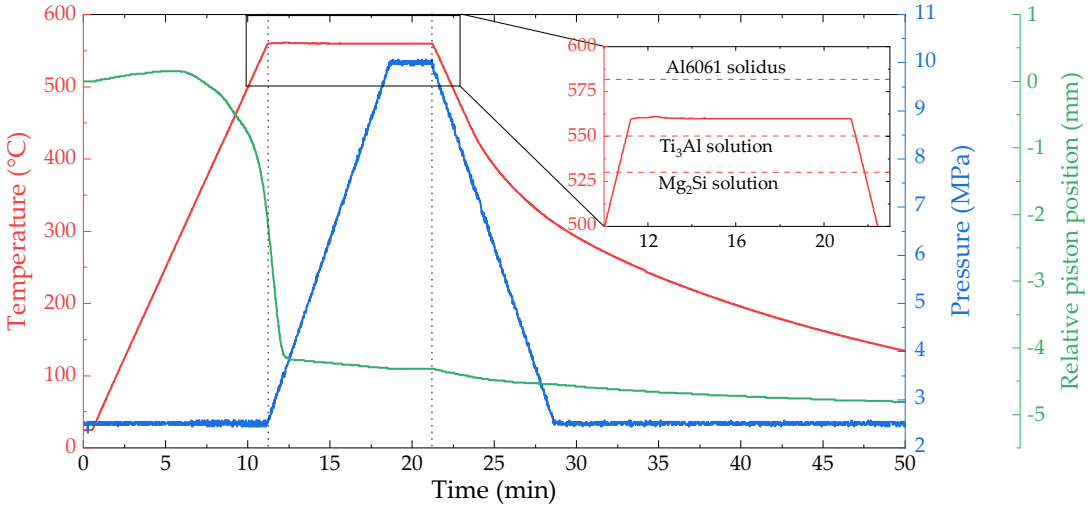

(a) The proof-of-concept samples

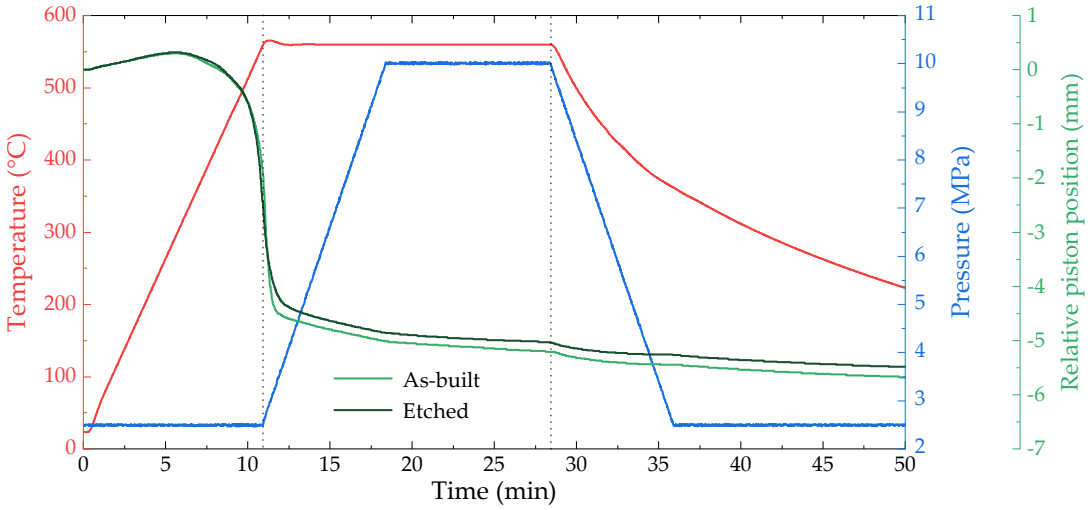

(b) The samples with the lattice reinforcement

Figure 4.2: The course of temperature, piston pressure and piston position during the sintering process. The relative position is calculated with the starting position as a reference, positive and negative values indicate sample and piston dilation and shrinkage, respectively. Solution temperatures of the intermetallic phases are taken from [105].

4.2 Results

4.2.1 Proof-of-Concept & Interface Investigations

The first series of samples was sintered to test the designed sintering program and to investigate the interface prior to the sintering with the printed lattice. The detailed micrographs of the microstructure are shown in Figure 4.3, along with the EDS line profiles across the interface.

Major features of the interface are common to both reinforcement materials. The Ti wire has a Si and Al enriched diffusion layer (marked DL) at its surface. Precipitates of a similar composition (marked P) are found embedded in the Al matrix along the interface. As measured by EDS, a Mg, Al and O enriched transition layer (T) is found between the diffusion layer (DL) and the precipitates adjacent to the interface (P) in the Ti Grade 2 sample (Figure 4.3a), while the composition of this Mg enriched layer coincides with the composition of DL in the Ti-6Al-4V sample (Figure 4.3b). It should be noted that the EDS signal depth can reach 1 µm, so it may be influenced by the interface tilt underneath the specimen surface. The DL seems to be thinner at the interface when Ti-6Al-4V is used than in the case of Ti Grade 2. Also, the precipitates in the matrix are fewer and there is some porosity along the interface.

A more detailed chemical analysis of the phases at the interface and diffusion profiles cannot be done in SEM due to the abovementioned spatial resolution limitations. Moreover, electron diffraction experiments are necessary for phase identification within the diffusion layer and precipitates. Therefore, cross-section lamellae for TEM investigations were prepared from the interfaces. The finished lamellae are shown in Figures 4.4a and b.

The TEM investigations started with repeating the EDS analysis and bright-field (BF) imaging, shown in Figure 4.5. According to the BF micrographs, the diffusion layer consists of very fine grains ($\sim$ 50 nm in diameter) in both samples. The chemical analysis reveals that both diffusion layer and the precipitates are chemically homogeneous. Mg is entrapped between these two layers, rejected from the newly formed precipitates and unable to diffuse into the diffusion layer and the Ti wire.

There is no significant chemical gradient in neither the Al matrix, nor the Ti wire – all diffusing atoms are incorporated either into the precipitate, or into the diffusion layer. Ti is practically insoluble in Al, as well as Si in Ti, but numerous intermetallic phases can be formed [106, 107].

The chemical composition of the individual phases was extracted from the EDS maps and the data are summarized in Table 4.2. The measured values were not corrected for the specimen thickness and are thus only semiquantitative, i.e. with an accuracy $5-10$ at.%. Within this margin, all observed phases – precipitates and diffusion layer alike – consist mostly of Ti and Si ($38-55$ at.%) with a minor addition of Al ($6-12$ at.%). The measured content of Mg and V is negligible.

There are two intermetallic phases reported in the literature with the corresponding chemical composition, denoted as τ_1 (orthorhombic) and τ_2 (tetragonal) [108]. Their basic crystallographic data are provided in Table 4.3 and the unit cells are visualized in Figure 4.6.

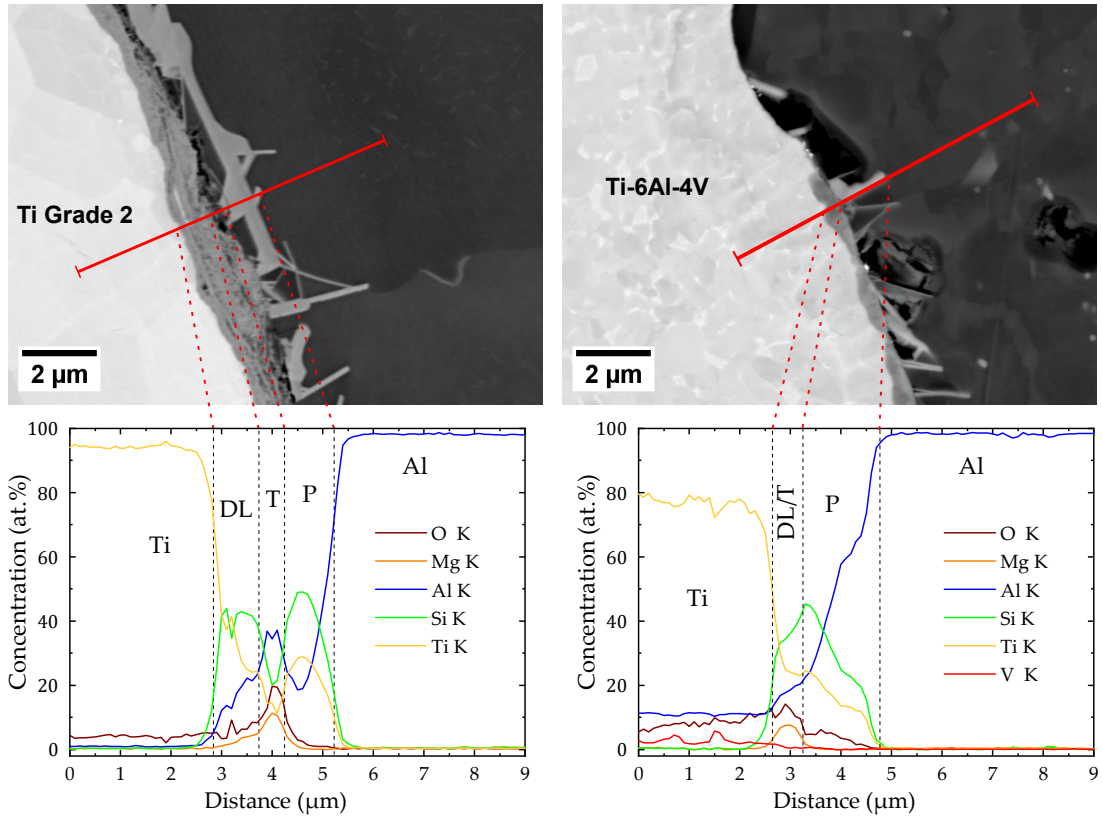

(a) Sample with Ti Grade 2 wire

(b) Sample with Ti-6Al-4V wire

Figure 4.3: A detail of the Ti/Al6061 interface, along with the EDS concentration profile across the interface with major regions labeled: Ti/Ti-6Al-4V wire (Ti), Al6061 matrix (Al), diffusion layer (DL), precipitates (P) and the transition layer with Mg segregation (T).

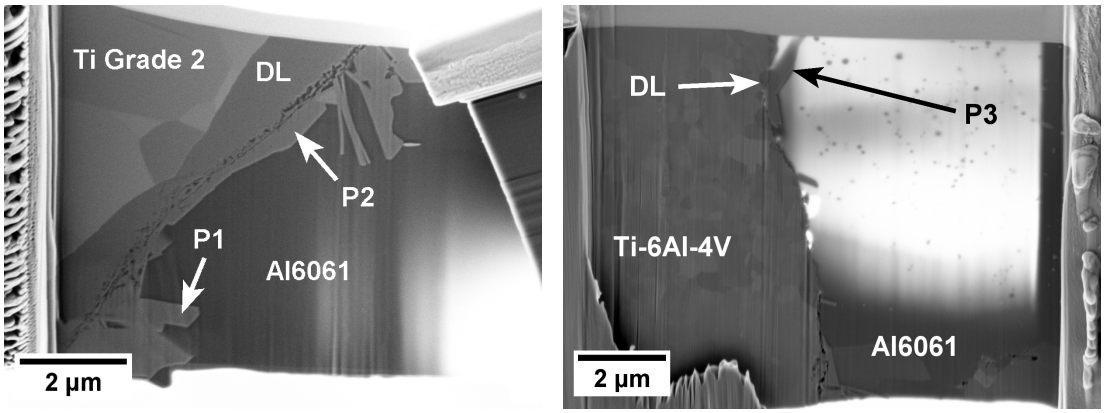

(a) The Ti Grade 2 sample lamella

(b) The Ti-6Al-4V sample lamella

Figure 4.4: Preparation of the cross-section lamellae from the interface. The features marked at the lamellae were further investigated by TEM.

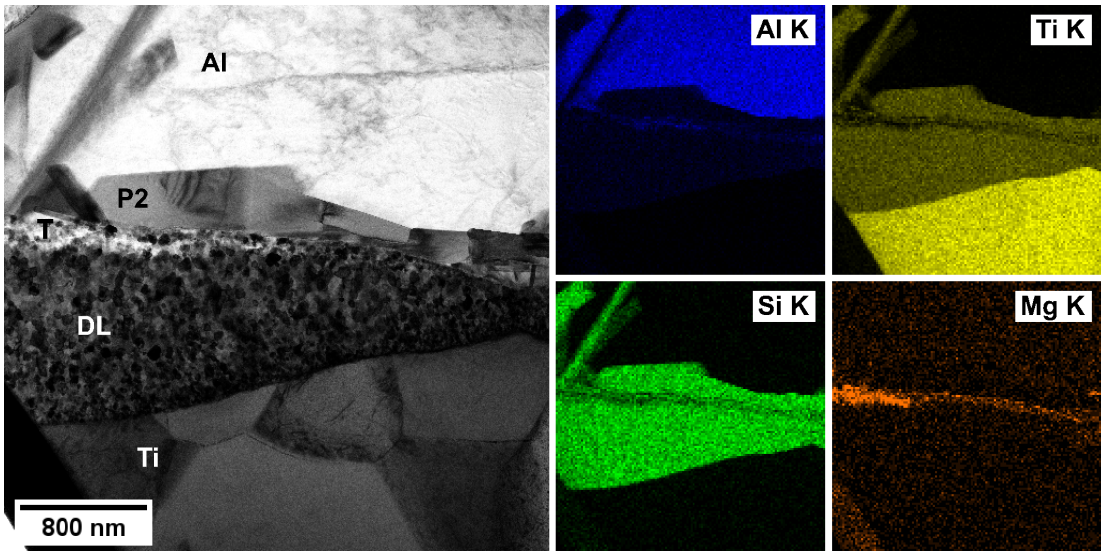

(a) Ti Grade 2 sample

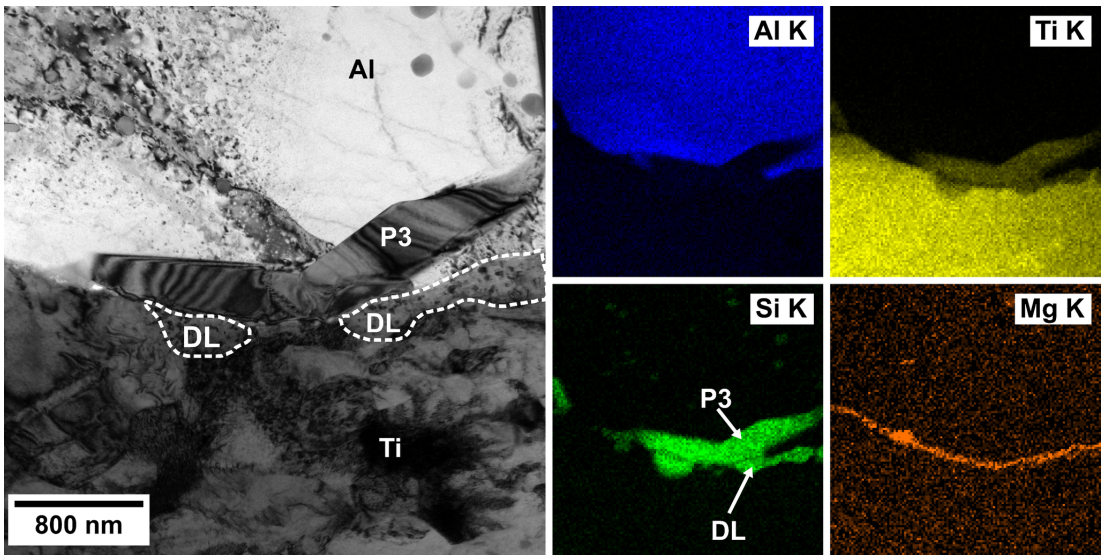

(b) Ti-6Al-4V sample

Figure 4.5: BF micrographs and EDS maps of the interface with precipitates (P) and the diffusion layer (DL). Both diffusion layer and precipitates have a homogeneous chemical composition, consisting of mostly Si, Al and Ti. Mg is segregated between the diffusion layer and precipitates.

Table 4.2: EDS analysis of the diffusion layer and individual precipitates, the labels correspond to the labels in Figure 4.4. The data are semi-quantitative only.

		Mg (at.%)	Al (at.%)	Si (at.%)	Ti (at.%)	V (at.%)
Ti Grade 2	Diffusion layer (DL)	< 0.1	10	48	42	—
	Precipitate 1 (P1)	< 0.1	10	38	52	—
	Precipitate 2 (P2)	< 0.1	12	47	41	—
Ti-6Al-4V	Diffusion layer (DL)	2	7	51	39	1
	Precipitate 3 (P3)	0.1	6	55	38	1

The crystallographic information file (CIF) of the τ_2 was taken directly from the International Crystallographic Database [109], the CIF of the τ_1 phase was constructed from the CIF of its prototype phase $Zr_3Al_4Si_5$ by replacing Zr with Ti and adjusting the lattice parameters to those reported in [110].

Even though the different space group suggest otherwise, the two phases are crystallographically similar. As seen from Table 4.3, the a and b lattice parameters are almost identical and the c lattice parameter of the τ_1 phase is twice that of the τ_2 phase. The unit cell visualizations in Figure 4.6 show that the structure is based on the fcc lattice stacked along the c direction, with some preferential occupation of lattice sites. The τ_1 unit cell essentially consists of two stacked τ_2 unit cells, one of them mirrored and rotated. Both structures have two types of sites – the first occupied by Si and Al atoms and the second by Ti and Al atoms.

Diffraction experiments were performed in TEM as a next step. The ring patterns of the polycrystalline diffusion layers are shown in Figures 4.7c and d. The diffraction patterns were azimuthally integrated and the radial profiles are shown in Figure 4.7e, along with the simulated peak positions of the τ_1 and τ_2 phases.

A mixture of τ_1 and τ_2 was identified in the Ti Grade 2 sample, while only τ_2 could be detected in the Ti-6Al-4V sample. The τ_1 phase is manifested by the minor peaks at 3.3 and 4.9 nm^{-1}, which are not found in the Ti-6Al-4V sample profile. The peaks at 3.55 and 4.05 nm^{-1}, corresponding to the τ_2 phase, are found in both profiles. The strong reflections at 4.5, 5.5 and 7.5 nm^{-1} are common to both phases.

Three precipitates (P1, P2 (Ti Grade 2 sample) and P3 (Ti-4Al-4V sample)), marked in Figure 4.4, were investigated by TEM. Analysis of the latter two proved to be easier and is shown first.

The SAED patterns of the precipitates P2 and P3 are shown in Figure 4.8. The labels P2 and P3 correspond to the labels in the Figures 4.4a and b, respectively. Both diffraction patterns correspond to the τ_2 phases with the c axis of the lattice perpendicular to the longitudinal axis of the precipitate.

The analysis of the P1 precipitate is more complex. Figures 4.9a and b show overall and detailed micrographs of the precipitate tip. Three different regions

Table 4.3: Crystallographic parameters of τ_1 and τ_2 phases.

	Space group	a (nm)	b (nm)	c (nm)	Reference
τ_1	$I4_1/amd$	0.3576	0.3576	2.715	[108, 110]
τ_2	$Bmmb$	0.3600	0.3600	1.353	[108, 109]

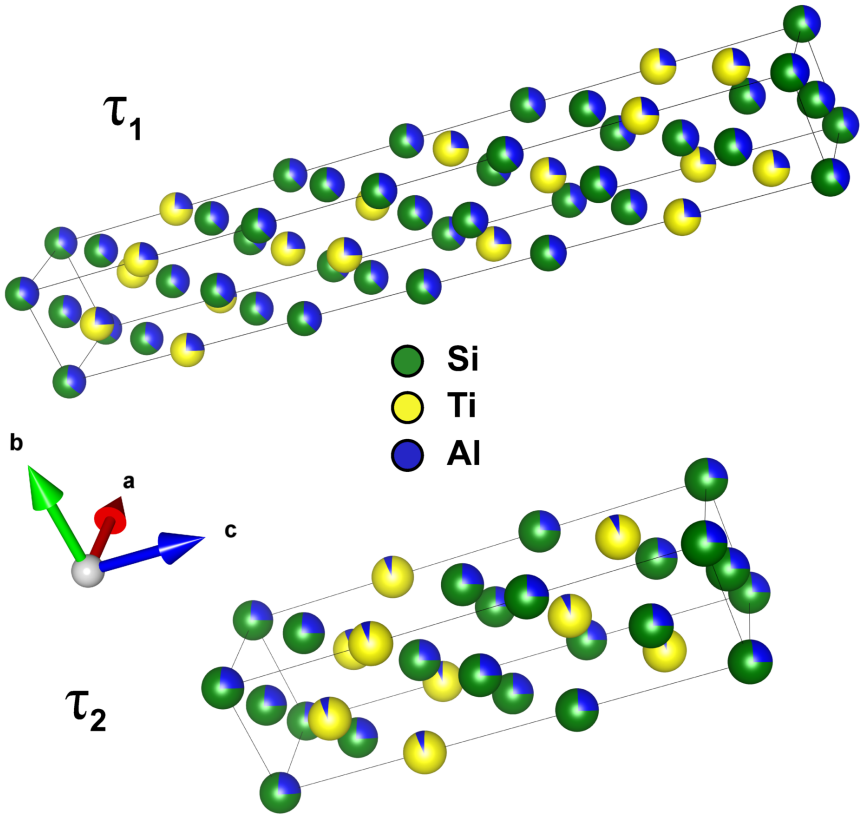

Figure 4.6: Unit cells of the τ_1 and τ_2 phase. The τ_1 phase is adapted from its prototype $Zr_3Al_4Si_5$. Coloring of individual atoms represent relative occupancies according to the CIFs. Visualizations were prepared using the VESTA software [111].

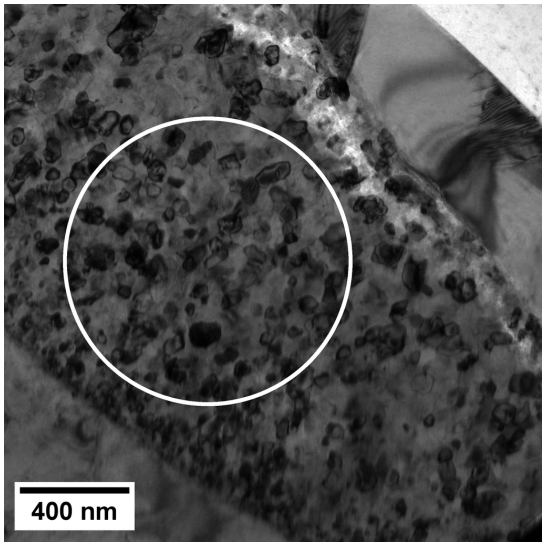

(a) BF TEM micrograph, Ti Grade 2 sample

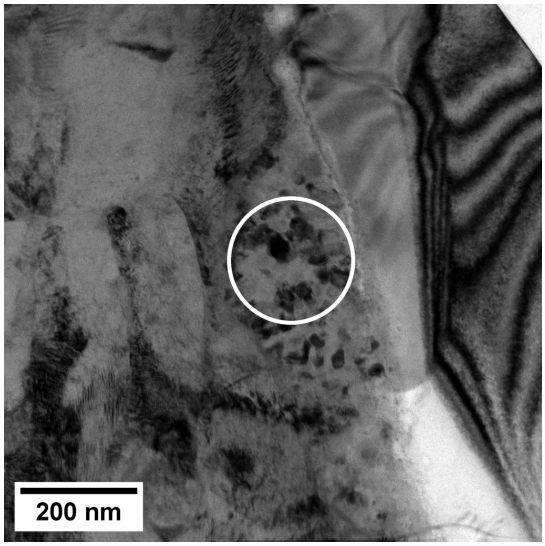

(b) BF TEM micrograph, Ti-6Al-4V sample

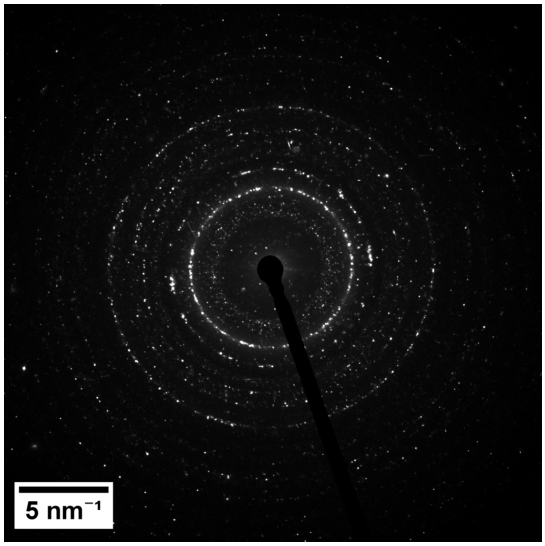

(c) SAED ring pattern, Ti Grade 2 sample

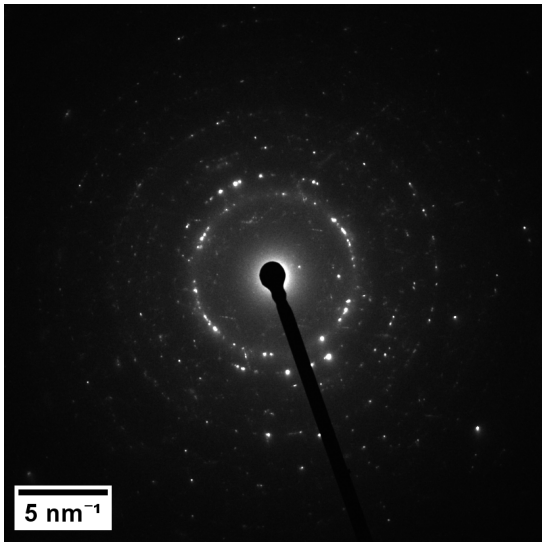

(d) SAED ring pattern, Ti-6Al-4V sample

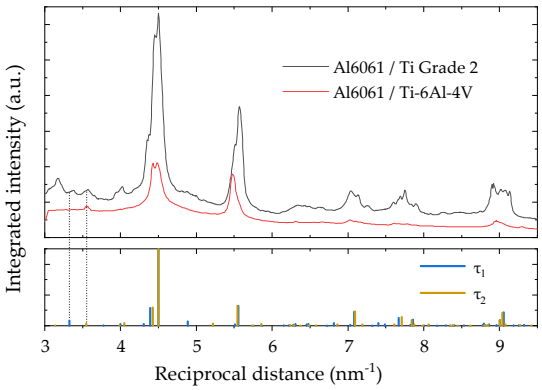

(e) The azimuthally integrated ring patterns with calculated positions of the τ_1 and τ_2 lines

Figure 4.7: The BF micrographs and SAED ring patterns of the diffusion layers at the interface. The line height in the azimuthally integrated profiles corresponds to the relative peak intensity.

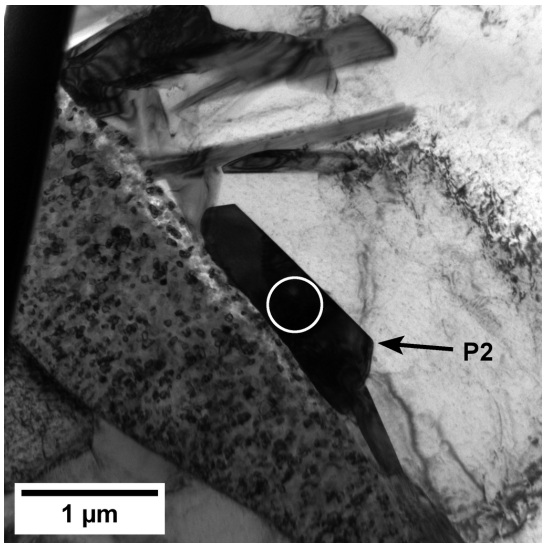

(a) BF TEM, Ti Grade 2 sample

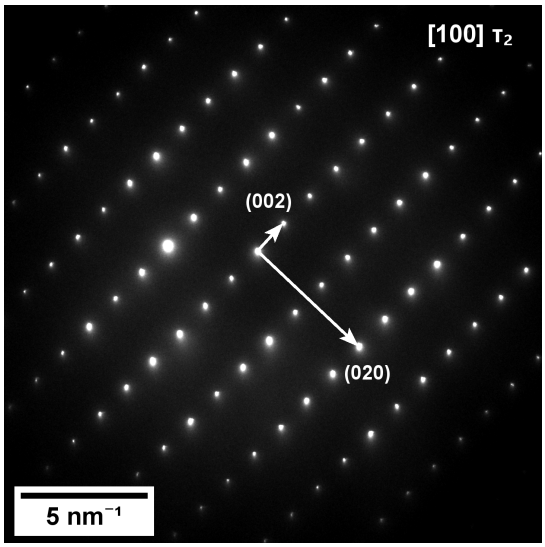

(b) SAED of τ_2 phase along [100], preicpitate P2 in Ti Grade 2 sample

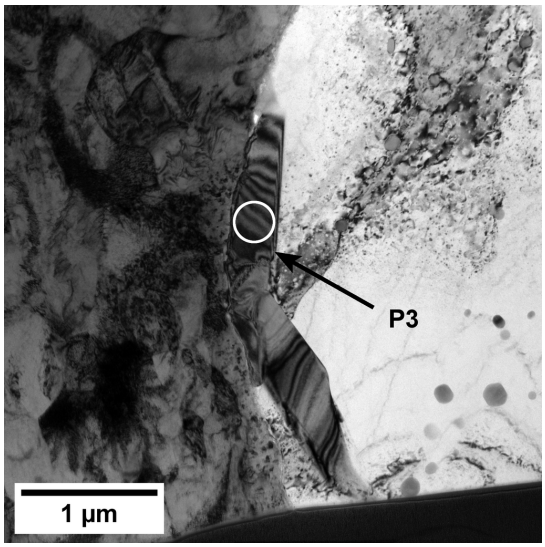

(c) BF TEM, Ti-6Al-4V sample

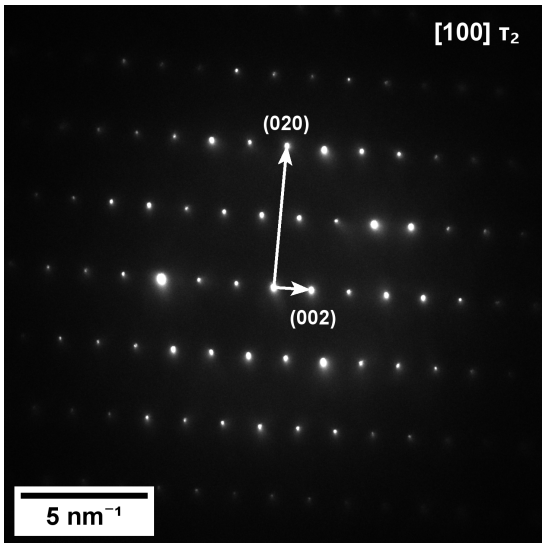

(d) SAED of τ_2 phase along [100], preicpitate P3 in Ti-6Al-4V sample

Figure 4.8: The BF micrographs and SAED patterns of the τ_2 precipitates at the interface. The SAED pattern was taken from the areas marked with circles. The labels correspond to the labels in Figure 4.4.

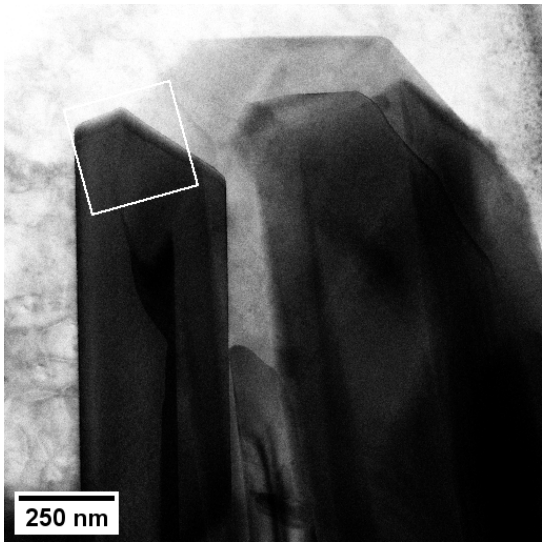

(a) STEM micrograph of the precipitate with the area shown in detail in (b)

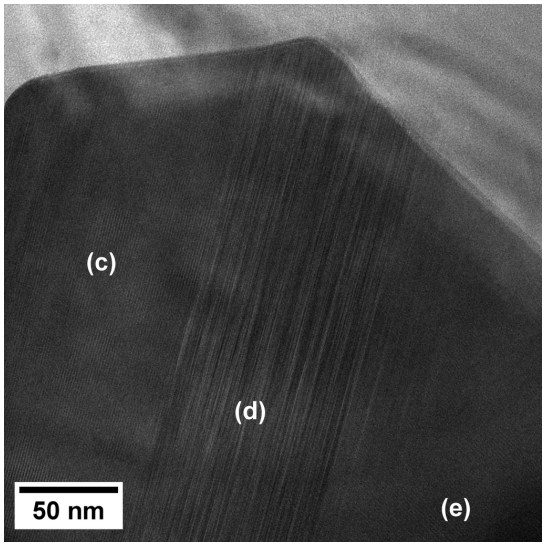

(b) High-resolution TEM micrograph with SAED areas marked

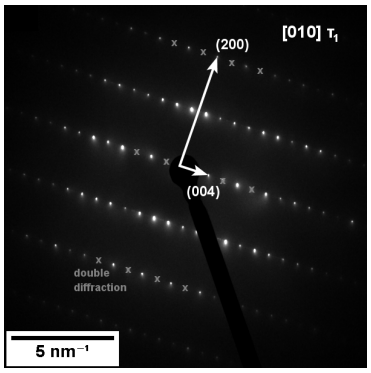

(c) τ_1 phase in [010] direction

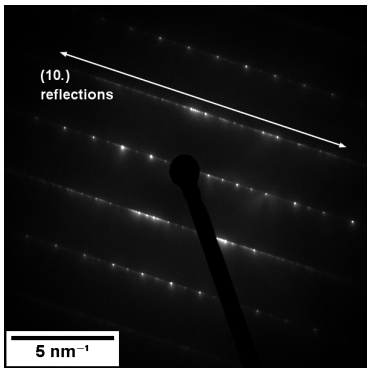

(d) Complex stacking sequence along c axis, creating extra $\{10l\}$ type reflections (blending into streaks)

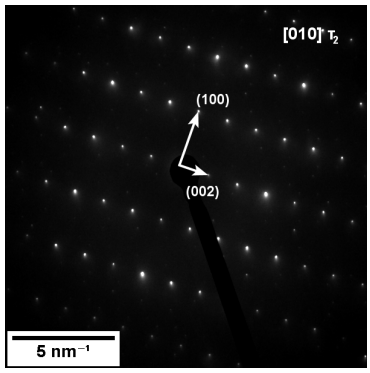

(e) τ_2 phase in [010] direction

Figure 4.9: A TEM analysis of the P1 precipitate (marked in Figure 4.4a). Three different crystal structures were found in a single precipitate. Double diffractions in SAED patterns are marked by grey. crosses.

were identified in Figure 4.9b, corresponding to the three SAED patterns in Figures 4.9c–e. τ_2 phase is identified in the (e) region (right) and τ_1 phase in the (c) region, both aligned with the c axis perpendicular to the longitudinal axis of the precipitate. The modulated structure between them has many additional diffraction spots (Figure 4.9d) of a $\{10l\}$ type, but it still remains aligned with the τ_1 and τ_2 phases This corresponds to a greatly increased c lattice parameter, equal to the complex stacking sequence of the τ_1/τ_2-like unit cells. The a and b lattice parameters are preserved.

We have shown that the interface of Al6061 with Ti-6Al-4V is qualitatively the same as the interface with the Ti Grade 2, as the same phases emerged. It was therefore decided that the 3D printed lattice would be made of Ti-6Al-4V, as it is a more common construction material with a higher strength than unalloyed Ti Grade 2. The duration of the isothermal sintering step was increased

to increase the thickness of the diffusion layer at the interface to match the thickness observed in the Ti Grade 2 sample and reduce the porosity observed at the interface (Figure 4.3).

Furthermore, the Al6061 was not thermally treated, though it is an age-hardenable alloy. In order to reach the maximum strength of the whole composite, the samples for mechanical testing would be subjected to additional heat treatment after sintering in the second step of manufacturing described in the next section.

4.2.2 Sintering with the Ti-6Al-4V Lattice

The lattice was manufactured by SLM on demand at VŠB-TUO according to the drawings in Figure 4.1b. The SEM micrographs of the as-built lattice are shown in Figure 4.10a. The designed thickness of the lattice strut in was 200 µm, while the measured thickness of the as-built strut is as high as 297 ± 23 µm. This difference is understandable, because the designed thickness is at the limit of the printer resolution and there are nonmelted spherical particles attached to the printed lattice, increasing the strut thickness even further.

The presence of such particles on the surface is generally undesirable, because they increase the surface roughness and would prevent a proper attachment of the Al matrix during sintering. The lattice was therefore etched for 2 min using Kroll etchant and the result is shown in Figure 4.10b for comparison with the as-built lattice. It can be seen that the spherical particles were removed from the surface and the surface roughness has decreased. Moreover, the strut thickness was measured to be 218 ± 26 µm, much closer to the designed thickness. This corresponds to the volume fraction of 20.8 %, assuming simple cylindrical struts with the measured thickness.

The sintering was carried out according to the program described in detail in the Material Preparation section. The samples were cut and polished, the overview light microscopy images are shown in Figure 4.11. It is immediately visible that the sintering was not very successful – the Al powder did not fully penetrate into the Ti-6Al-4V lattice. The penetration was slightly deeper for the etched lattice than for the as-built lattice due to smoother surface and smaller strut thickness. On the other hand, thanks to the low piston pressure used, the titanium lattice has remained undeformed with the 1 mm spacing preserved in both directions.

The detailed SEM micrographs are shown in Figure 4.12. The sample with the as-built lattice was sufficiently sintered less than 1 mm in depth (i.e. less than one lattice cell). The sample sintered with the etched lattice was sintered $1 - 1.5$ mm deep. The original plan of doing compression tests could not be fulfilled, but it was possible to perform a simple the three-point bending test from the subsurface layer (shown in Figure 4.12d) for evaluation of properties of the interface under mechanical loading. Only the etched sample was mechanically tested, because the properly sintered region of the as-built sample is too small.

The material with the etched lattice was tested in the as-sintered condition and after the T6 heat treatment. Before the three-point bending test, the mi-

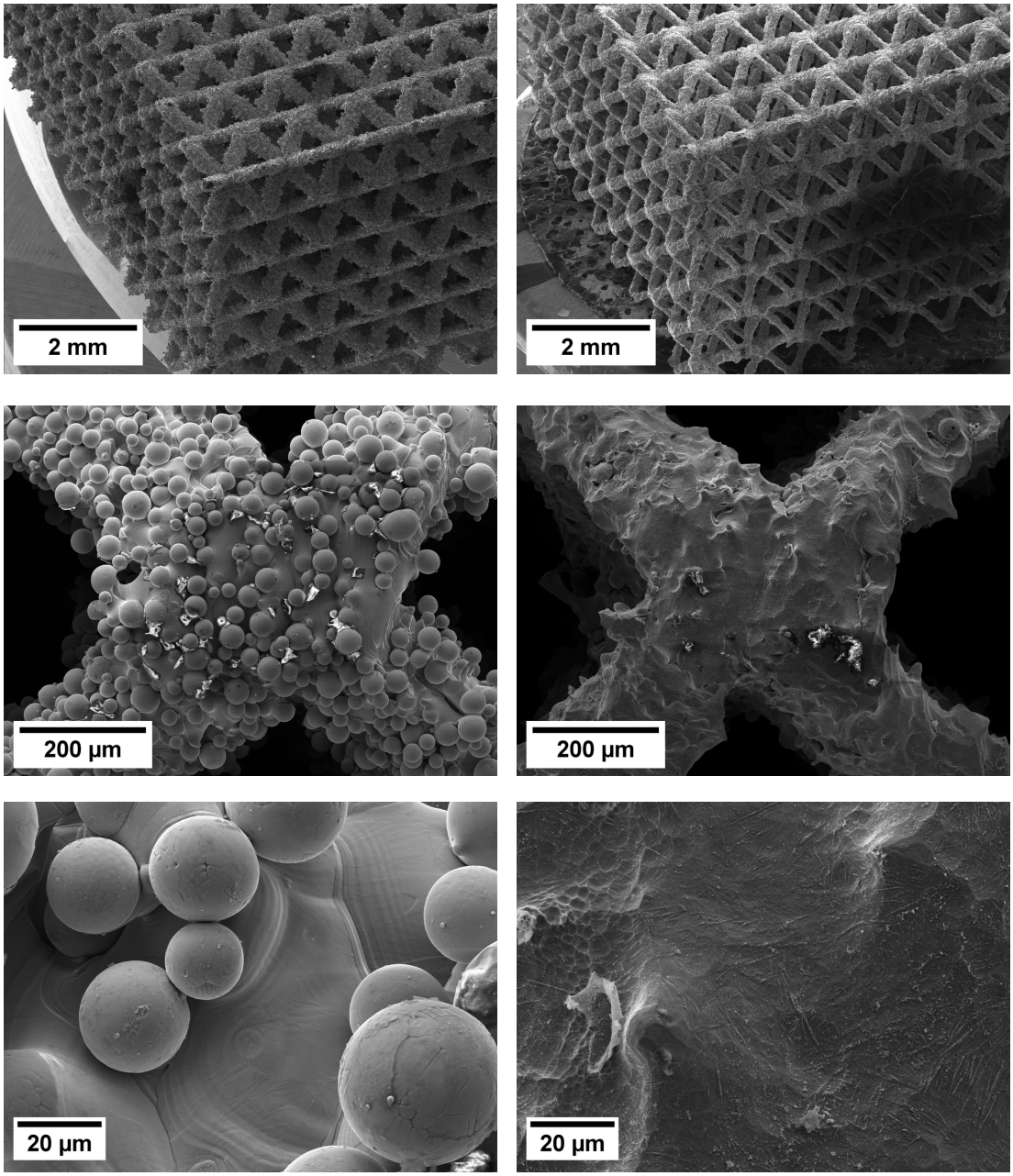

(a) As-built lattice (b) Etched lattice

Figure 4.10: A comparison of the as-built and etched Ti-6Al-4V lattices (SE SEM micrographs) in a range of magnifications.

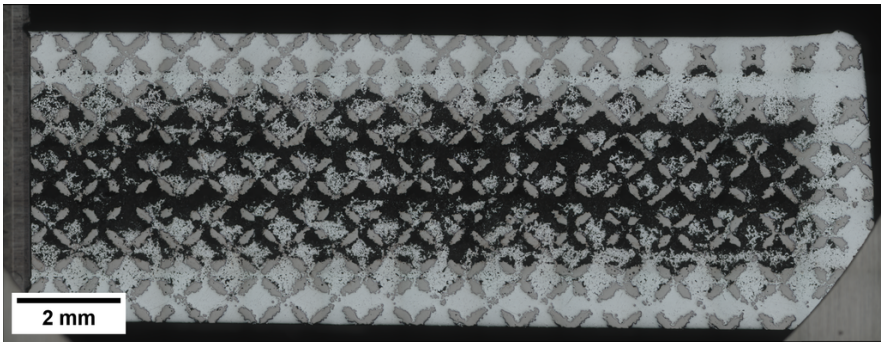

(a) As-built lattice

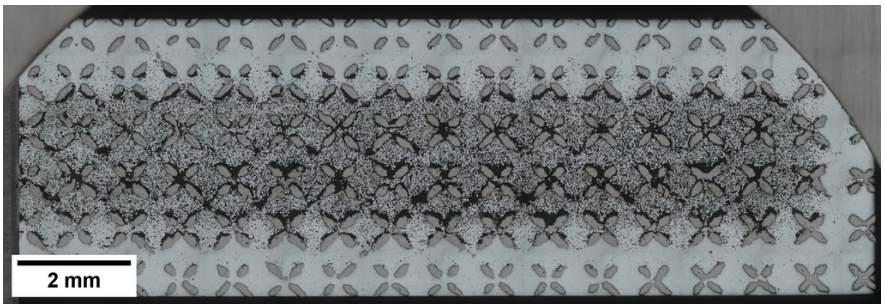

(b) Etched lattice

Figure 4.11: Low-magnification light micrographs of the as-sintered cross-sections

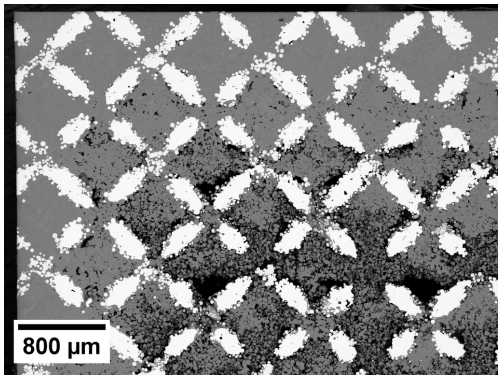

(a) As-built, BSE micrograph

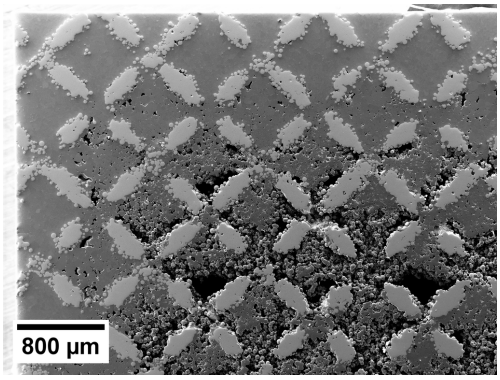

(b) As-built, SE micrograph

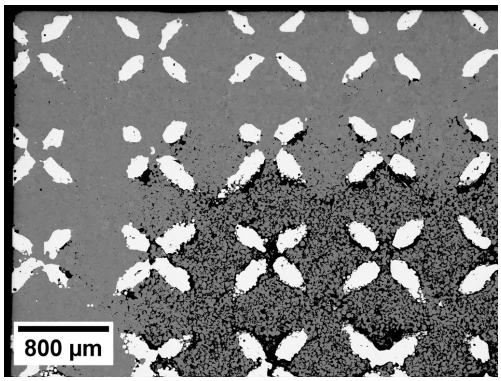

(c) Etched, BSE micrograph

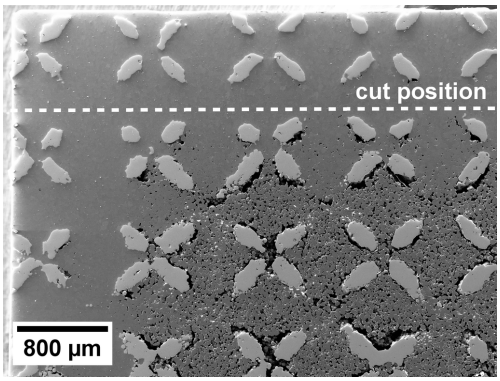

(d) Etched, SE micrograph

Figure 4.12: A comparison of the microstructure of the corner of the sintered sample. The difference in porosity is clearly visible. The cut position for preparation of specimens for three-point bending tests is marked in (d).

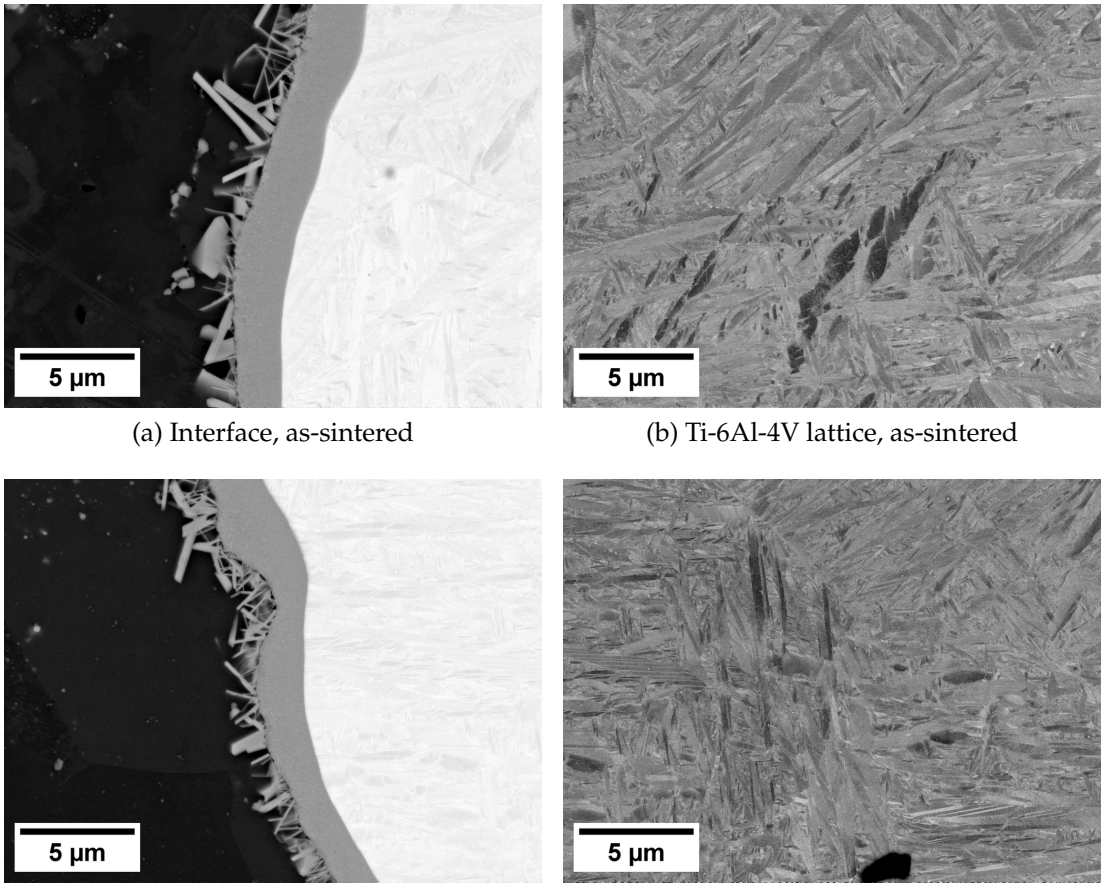

(a) Interface, as-sintered

(b) Ti-6Al-4V lattice, as-sintered

(c) Interface, T6 heat treated

(d) Ti-6Al-4V lattice, T6 heat treated

Figure 4.13: Detailed BSE micrographs of the as-sintered and T6 aged samples prepared from the etched lattice

crostructure of the samples was checked, the micrographs of the interface and the lattice are presented in Figure 4.13.

The interfaces of both as-sintered and aged sample, shown in Figures 4.13a and c are similar, having a homogeneous diffusion layer of 2 µm in thickness and without interfacial porosity (as observed earlier in Figure 4.3b, thanks to the prolonged sintering time. Figures 4.13b and d show that the lamellar martensitic microstructure is still present after sintering, and even after the ageing treatment (Figures 4.13d).

Four different conditions were tested by the three-point flexural test in total: the as-sintered and aged composite samples (two conditions, four specimens each) and the as-sintered and T6 aged pure Al6061 alloy for comparison (two conditions, three specimens each). The acoustic emission (AE) and DIC were acquired during all measurements to provide a deeper insight into the deformation mechanisms.

All deformation curves are plotted in Figure 4.14a for easy comparison. Individual samples are then shown in Figures 4.14b–e, accompanied by the AE signal (a cumulative count of AE events). The DIC maps (engineering strain along X axis) at the positions marked by arrows are shown.

The pure Al6061 alloy samples show excellent plasticity (the test was stopped before any fracture occurred) accompanied by very low AE activity,

especially in the as-sintered sample (Figure 4.14b). Note that the AE scale is about two orders of magnitude lower than for the composite samples. The bending yield strength was significantly increased by the T6 ageing from 100 to 450 MPa. The deformation curves are well repeatable.

The deformation of the as-sintered Al6061/Ti-6Al-4V composite sample (Figure 4.14d) is much less repeatable; both yield strength and ductility vary significantly. Two specimens failed during the test (as visible on both load drops and rise in AE events), while the other two have endured until the end of the test. The DIC map reveals a periodicity in strained regions, corresponding to the lattice period. It seems that the deformation is mostly accommodated by the Al matrix and the lattice itself remains relatively undeformed, apart from the necessary bending to accommodate the macroscopic geometry change.

The T6 aged composite is significantly more brittle than the as-sintered composite. The yield stress is similar to the plain T6 aged Al6061 alloy, but first signs of cracking occur almost immediately after the elastic part of the curve (Figure 4.14e, note that the horizontal axis is shortened to show all the features). The AE activity is high during deformation of all specimens, marking ongoing crack propagation. The DIC map shows a highly localized deformation and a crack formation as well.

The deformed samples were imaged by SEM on the longitudinal cross-section, the micrographs are shown in Figure 4.15. The white rectangle in Figure 4.15d indicates the orientation and position of the micrographs within the samples. While no cracks are visible in the as-sintered sample Figure 4.15b), a large crack can be observed in the aged composite sample in figure 4.15c, propagating along the interface between the matrix and the lattice. Its detail is shown in Figure 4.15d, the crack propagates between the diffusion layer and the precipitates in the matrix. Some minor cracks of the diffusion layer are also observed.

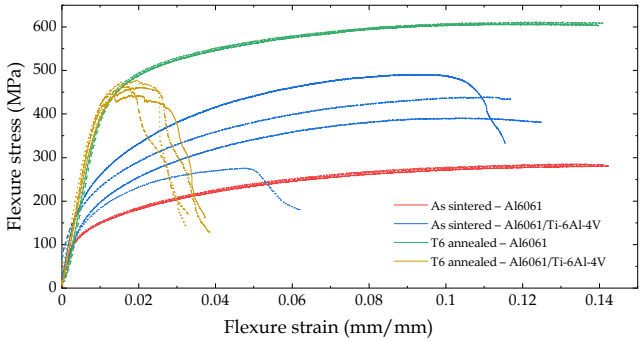

(a) A comparison of all deformation curves

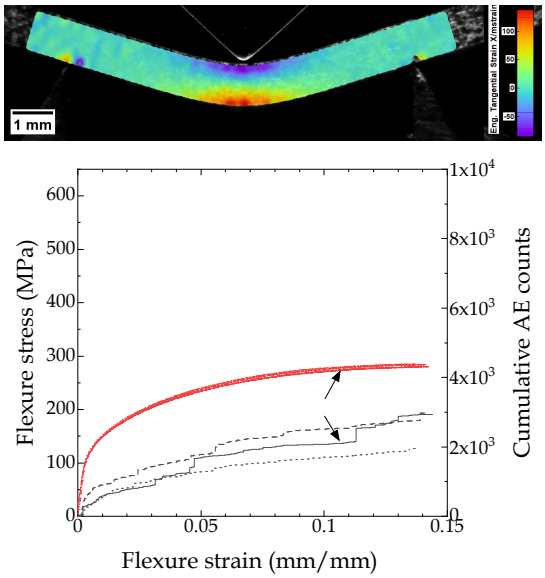

(b) Al6061 matrix, as-sintered

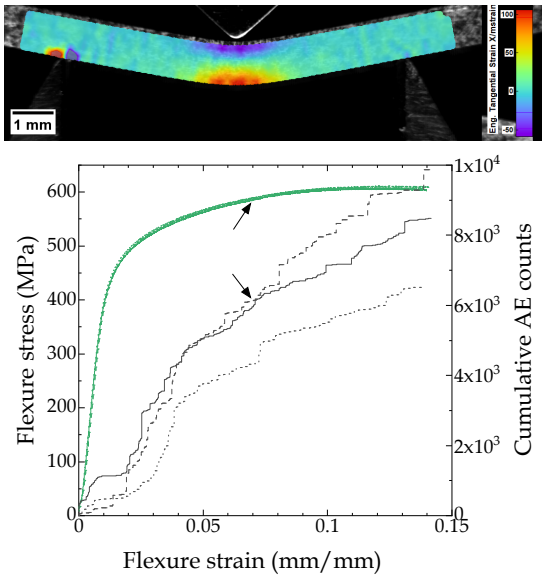

(c) Al6061 matrix, T6 heat treated

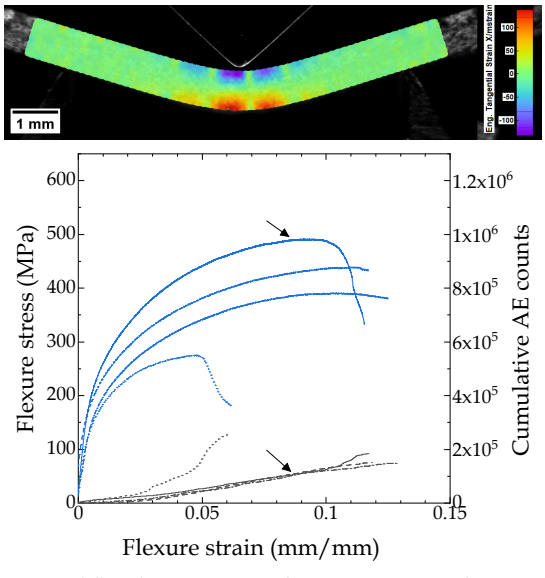

(d) Al6061 + Ti6Al-4V, as-sintered

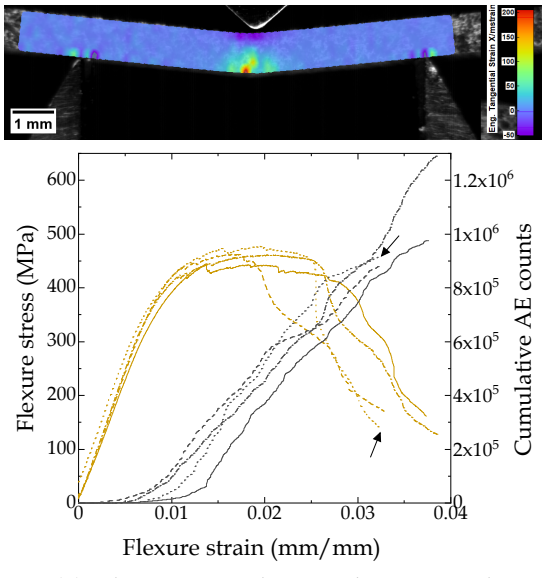

(e) Al6061 + Ti6Al-4V, T6 heat treated

Figure 4.14: Results of the three-point flexural test on the sintered samples after different ageing regimes. The non-reinforced Al6061, prepared under the same conditions, was also measured for reference. AE signals and the DIC maps (engineering strain in X direction) are shown for all samples in (b)–(e). Note that the scale of the AE signal is higher by two orders of magnitude for (d) and (e).

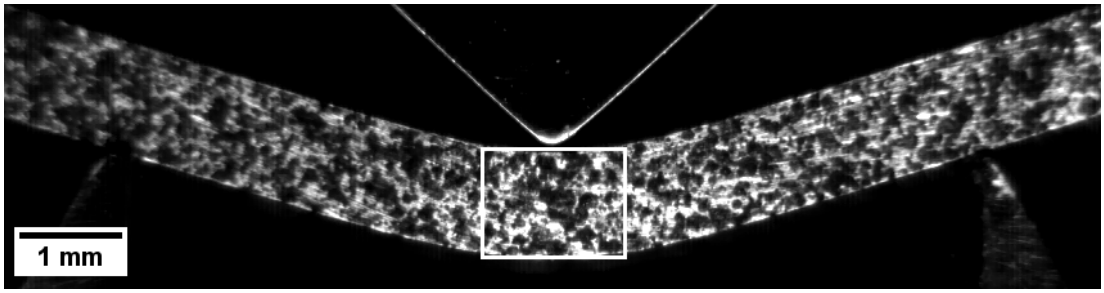

(a) Schematic position of the micrographs in (b) and (c)

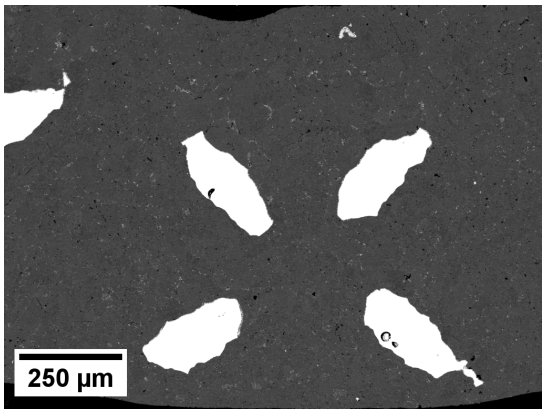

(b) Al6061 + Ti6Al-4V, as-sintered

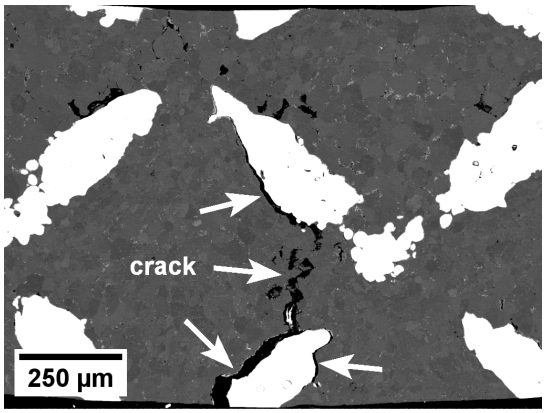

(c) Al6061 + Ti6Al-4V, T6 heat treated

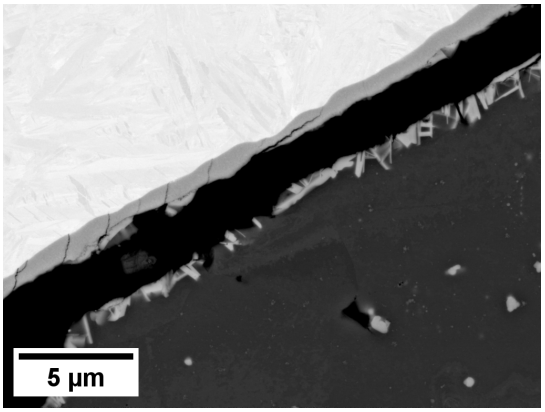

(d) Detail of the crack in (c)

Figure 4.15: Cross-section of the deformed samples. The crack propagation in the T6 heat treated compostite sample is visible.

4.3 Discussion

Both τ_1 and τ_2 phases are observed in the literature with a range of compositions. The available literature data are summarized in Table 4.4. τ_1 is generally reported with a lower concentration of Al than τ_2, but the difference is not very significant. Sometimes, only one of the phases (τ_1 / τ_2) is reported in experimentally constructed phase diagrams, despite the same annealing temperature (cf. [112] and [113] at 550 °C). It is therefore not clear whether only τ_1 or τ_2 or both are the equilibrium phases. The τ_1 and τ_2 phases investigated in this chapter have slightly higher concentration of Ti and lower concentration of Si. However, it should be noted that in our case, the phases may not be in a thermodynamic equilibrium – for example, the Si content may be limited by a diffusion rate from the Al matrix. Finally, the accuracy of the TEM EDS data may not be sufficient for resolving such differences.

The ambiguities in the reported phases in the literature are consistent with the observed complex stacking sequences – both τ_1 and τ_2 phases were observed together in a (kind of) single-crystalline precipitate, as shown in

Table 4.4: Composition of τ_1 and τ_2 phases: comparison of the literature data and our results. This work's data are marked in the same way as in the micrographs. Ti G2 and Ti64 stand for Ti Grade 2 and Ti-6Al-4V, respectively.

Phase	Condition	Source	Mg (at.%)	Al (at.%)	Si (at.%)	Ti (at.%)	V (at.%)
τ_1	45 d 550 °C	[112]	—	7.1– –13.9	51.9– –59.1	33.5– –34.2	—
	45 d 700 °C	[108]	—	6.2– –9.3	57.5– –60.9	32.4– –34.0	—
τ_1 & τ_2	10 min 560 °C	this work Ti G2, DL	< 0.1	10	48	42	—
		this work Ti G2, P1	< 0.1	10	38	52	—
τ_2	132 d 550 °C	[113]	—	10.4– –14.2	50.8– –53.7	33.9– –35.4	—
	45 d 700 °C	[108]	—	10.0– –11.6	53.9– –55.6	34.2– –34.5	—
		this work Ti G2, P2	< 0.1	12	47	41	—
	10 min 560 °C	this work Ti64, DL	2	7	51	39	1
		this work Ti64, P3	0.1	6	55	38	1

Figures 4.9c and e. The transition phase (Figure 4.9d) closely resembles the long-period stacking order (LPSO) phases observed in Mg-Zn-RE alloys [114], having a similar complex stacking sequences and diffraction patterns. Such phenomenon was already reported in the directed laser deposited TiAl alloys [115], but not in the ternary Al-Si-Ti system yet.

Other intermetallics can be also found in Al-Ti-Mg-Si system [108, 112, 113, 116, 117]. In [118], heat treatment of friction stir welded (FSW) CP Ti + Al alloyed with Mg produced Ti-Al-Mg intermetallics at the interface, growing into the Al. During mechanical testing, cracking occurred between Ti and the intermetallic layer. The layers up to 80 µm in thickness have grown after 40 h of annealing of FSW Al + Ti [119]. The Al-Ti-Si intermetallics were found to be exceptionally thermodynamically stable, producing 1.5 µm thick layer (after 1 h at 600 °C) even when joining Ti with Al alloy containing only 0.12 at.% of Si [120].

From the microstructural point of view, a continuous intermetallic interface without thermal stress cracking was produced in the thesis. This is comparable with the results by [121] for diffusion bonding of Ti Grade 2 with Al7075 alloy (510 °C, 17 MPa for 37 min), with the diffusion layer reaching 7 µm and able to withstand a shear stress up to 82 MPa. Unfortunately, the composition of the interfacial layer was not assessed in the report. Their alloy contained Cu and Zn, which may improve the bonding [122]. The diffusion bonding between Ti Grade 2 and Al6061 was also performed (520 °C, 6 MPa, 60 min), resulting in a continuous intermetallic layer 1 µm thick, without the precipitates in the Al matrix. However, this was carried out below the Mg_2Si solvus temperature (526 °C), meaning that Mg is found in the precipitates within the matrix and does not segregate at the interface.

In [123], Ti Grade 2 and Ti-6Al-4V were diffusion bonded to Al6016 (Al-1.2Si-0.4Mg) and Al5056 (Al-5Mg-0.1Mn-0.1Cr) alloys. Only the Ti Grade 2 + Al5056 combination produced a 1 µm thick intermetallic zone after 60 min at 520 °C, while no diffusion zone was reported for other combinations. Cracking occurred in the Al near the interface. In ultrasonic-assisted friction stir welded Ti-6Al-4V + Al6061, intermetallic layer of $2 - 3$ µm thick was reported [124], the tensile properties having improved with the thicker interface.

From macroscopic point of view, the penetration of the Al powder into the printed lattice is very poor. This is caused by the lattice having too small openings for the given particle size. This is also demonstrated by the differences between the as-built and etched lattices, with the latter showing better penetration both due to smoother surface and reduced strut size. Moreover, when the powder was already consolidated at the top and bottom part, the piston pressure could not be transmitted further into the lattice, despite the Al being just below the solidus temperature and having very low yield stress. In the paper which inspired this chapter [77], the unit cell of the reinforcing lattice was an order of magnitude larger (10 mm × 10 mm × 10 mm) with the struts relatively thinner (1 mm), while the powder size was $100 - 300$ µm in diameter. Similar dimensions were reported in [78] – the lattice size of 8.5 mm with the 1 mm strut size and a particle diameter of $20 - 60$ µm. Powder penetration was better in both cases, with no reported issues with the porosity in the sample centre.

The three-point bending tests have revealed that the composite can be considered effective only when reinforcing the soft and ductile solution treated Al alloy, which can accommodate the strain. However, the reinforcement is not effective with the properly aged Al6061 alloy, which has high strength and the load is thus transferred to the interface in full. The crack propagates between the diffusion layer and the precipitates, i.e. along the Mg rich layer. The strain localization is highlighted by the DIC measurements from the very beginning of the deformation. It follows that the interfacial strength could be increased by using a different Al alloy, not containing Mg.

4.4 Summary

Two composite materials – Al6061 + Ti Grade 2 or Ti-6Al-4V were prepared by the field-assisted sintering technology. Intermetallic layer and precipitates are formed at the interface, corresponding to the τ_1 and τ_2 Al-Si-Ti phases. It was shown that these phases are closely related and intermediary phase with a complex stacking sequence can be formed, resembling the LPSO phases observed in Mg alloys.

The sintering of the 3D printed Ti-6Al-4V lattice resulted in the same interfacial microstructure, but it was not successful on the macroscopic scale due to poor penetration of the powder into the lattice. The material was sintered only 1 mm into the depth. Therefore, only three point bending deformation tests could be performed.

The deformation tests with the DIC have shown that the mechanical properties were improved only when using a very soft matrix. The properly aged Al6061 alloy has the same strength and a significantly better ductility than the composite material.

The first part of the chapter was published as a journal paper:

Kozlík, J., Veselý, J., Stráský, J., Chráska, T. & Janeček, M. Interface of a Al6061/Ti Composite Prepared by Field Assisted Sintering Technique. *Metals* **11**. DOI: 10.3390/met11010073 (2021).

Even though the ageing of the composite was not very successful, it brought us to the idea of performing the annealing treatment directly in the FAST device within a single process. Al alloys are, however, not suitable for this approach due to long annealing times (unsuitable for FAST) and low annealing temperatures (making the standard heat treatment easy to perform). Metastable Ti alloys are different matter due to a strong dependence of mechanical properties on even short thermal treatments, which are performed at higher temperatures and often require controlled environment preventing contamination – this all can be provided by FAST.

5 Blended Elemental Powder Metallurgy of Ti-5Al-5V-5Mo-3Cr Alloy

In this chapter, we would like to show that it is possible to sinter, homogenize and age a sample in the FAST furnace in a single run – starting from the blended elemental powders, ending with a sample ready for standard sized tensile testing. This approach was tested on a commercially available Ti-5Al-5V-5Mo-3Cr alloy (abbreviated as Ti5553).

One of the challenges of the FAST is a limited size of specimens available for mechanical testing. In particular, when the samples are prepared from blended elemental powders at high temperature, the grain size is large and the specimen cross-section contains only few grains, compromising the test. Therefore, upscaling of the process is crucial – not only for the sake of mechanical testing, but also to be able to produce larger parts. A custom FAST assembly was designed, able to withstand the sintering pressure at the high temperatures necessary for BEPM.

The microstructural optimization was done first using standard small-scale specimens and the process was then upscaled to prepare standard-sized samples for mechanical testing.

5.1 Material Preparation

Powders

The Ti5553 alloy was prepared using FAST from two raw materials – a blend of elemental powders (hereafter referred to as BE) and a prealloyed powder (referred to as PA) for comparison. The basic information about the powder supplier, morphology, size distribution and chemical composition are presented in Table 5.1. Elemental Ti, Al, V and Cr powders were used. However, Ti-15Mo master alloy powder was used instead of pure Mo, to promote the homogenization, since the diffusion of Mo is significantly slower. All powders were handled in air, with the notable exception of V powder, which is most sensitive to oxidation at ambient conditions and which was handled in an Ar filled glovebox. Two batches of V were used for sintering – the first one for the BE samples sintered at 1400 °C, but this V powder was found to be extensively contaminated by O. Another supplier was selected for the second batch of samples (sintered at 1500 °C) and for the sintering of a long rod. The similar

Table 5.1: The powders used for sintering. The particle size and morphology are taken from the supplier's datasheet, the chemical composition was measured independently by CGHE (carrier gas hot extraction). The numbers in parentheses are standard uncertainties of the last digits calculated from measurements of three specimens.

Powder	Manufacturer	Particle size & morphology	O (wt%)	N (wt%)	H (wt%)
Ti-5Al-5V-5Mo-3Cr	AP&C	spherical $20 - 63\,\mu m$	0.107(2)	0.015(1)	0.002(1)
Ti	TLS Technik	spherical $10 - 80\,\mu m$	0.163(1)	0.008(1)	0.001(1)
Ti-15Mo	TLS Technik	spherical $10 - 80\,\mu m$	0.198(5)	0.014(1)	< 0.001
V (BE 1400 °C)	Alfa Aesar	irregular $< 45\,\mu m$	2.263(6)	0.029(1)	0.049(1)
V (BE 1500 °C)	Goodfellow	irregular $< 45\,\mu m$	0.765(7)	0.046(1)	0.015(1)
Cr	Alfa Aesar	irregular $< 45\,\mu m$	0.636(3)	0.004(1)	0.015(1)
Al	Alfa Aesar	irregular $< 45\,\mu m$	0.428(27)	0.002(1)	0.009(1)

size of all powders is desirable for easier mixing and to prevent formation of agglomerates.

The powders were mixed using an in-house built rotational mixing device (a half-filled vial, eccentrically placed in a rotating drum). Morphology of the powders and homogeneity of the blend are shown in Figure 5.1. The EDS mapping (Figures 5.1b and c) has shown that no clusters or agglomerates are formed during mixing and that the powder blend is homogeneous.

Sintering

The sintering was done in two series – the first set consisted of standard-sized specimens (30 min in diameter, 10 mm in height) and was used for investigations of the ageing schemes and optimization of the process. The optimized program was then used for sintering of the second batch – the long rod for mechanical testing. The sintering programs are plotted in Figure 5.2.

The sintering starts with applying the pressure of 20 MPa, the sample is then heated to 600 °C and held there for 15 min. This step is used for reaction of the Al particles with other materials to prevent their sudden melting further in the process. The heating is then resumed at the rate of 100 K/min up to the designated sintering temperature (1000, 1400 or 1500 °C). After reaching it, the pressure is increased to 30 MPa and the sintering and the 30 min homogenization step starts. Then, the heating is turned off and the sample cools down

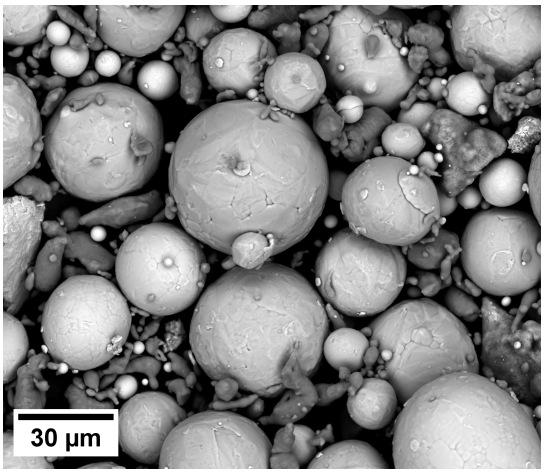

(a) Detail of the BE powder morphology

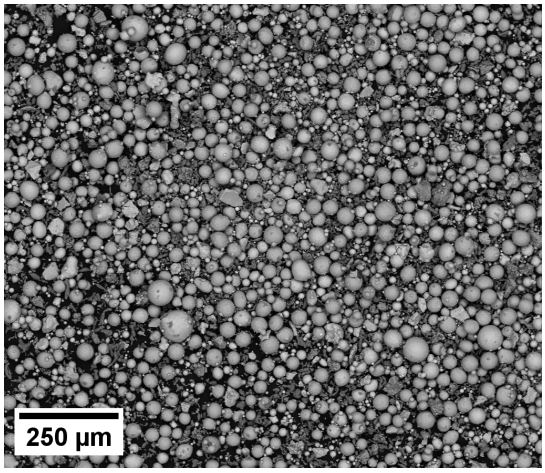

(b) Low magnification micrograph corresponding to (c)

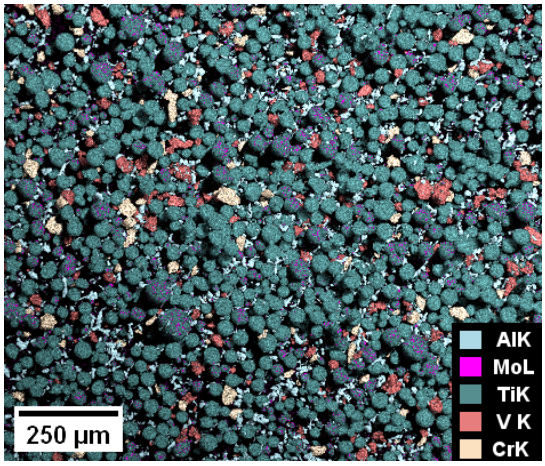

(c) EDS map showing the homogeneous blend

Figure 5.1: BSE micrographs of the powder morphology and a homogeneity of the blend. The EDS map in (b) corresponds to the BSE micrograph in (c).

freely, mostly by conduction of heat to the water-cooled pistons. The cooling rate is not actively controlled, its rate is comparable to air cooling (an order of 100 K/min). The cooling either continues all the way down to the RT (black line in Figure 5.2), or the heating is resumed and the process continues by an ageing step. The first program (red line in Figure 5.2) has two ageing steps – 30 min dwell at 800 °C, followed by 30 min at 600 °C, the second program (orange line in Figure 5.2) has only a single ageing step at 600 °C for 30 min. Both samples are then cooled to the RT after the ageing. Both programs with ageing simulate conventionally used treatment of the Ti5553 alloy [50]. The temperature overshoot of the as-sintered sample (black line in Figure 5.2) at 5 min was caused by a malfunction of the temperature regulator, but it is considered to have no effect on the outcome of the sintering, as the main stage occurs at 1500 °C.

The temperature was controlled by a C-type thermocouple in the bottom piston (cf. Figure 3.1). A tungsten foil was used as an inner spacer to prevent carbon contamination and formation of carbides due to high sintering temper-

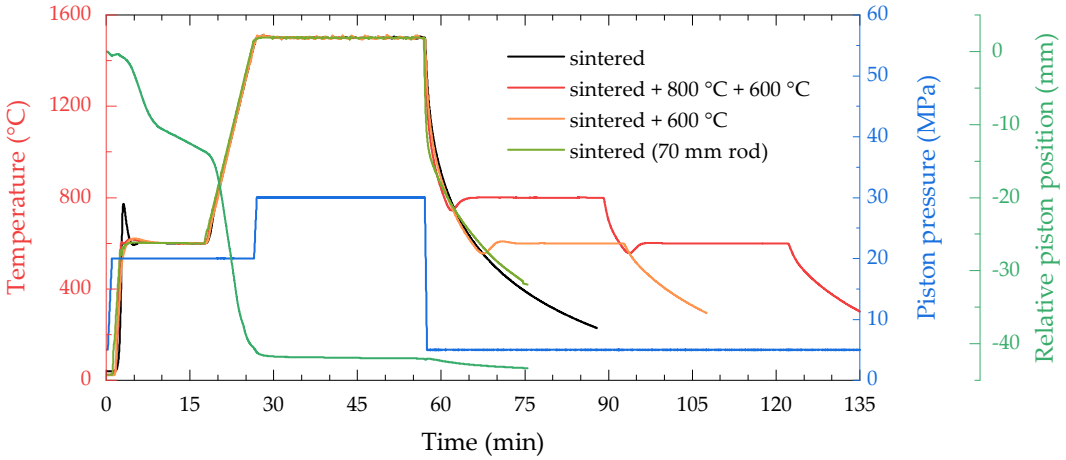

Figure 5.2: The sintering process parameters during three different programs – sintering only (black line) and two different in-situ ageing schemes (red + orange lines). The applied piston pressure was identical for all samples and programs (blue line). The presented records relate the BE samples sintered at 1500 °C. The temperature spike at the black line at 5 min is caused by a fault in the temperature regulator, but it is considered to have no effect on the outcome of the sintering and homogenization process. The temperature and piston position data for the long rod are shown as well (green lines).

atures. The resulting samples have the diameter of 30 mm and the height of approximately 10 mm.

As a next step, the die was upscaled for long rod production to compare its mechanical properties with the conventionally cast and forged (CF) Ti5553 alloy produced by TIMET. We have designed a special assembly for preparation of a long rod (having 15 mm in diameter and approximately 75 mm in length), allowing us to prepare tensile specimens of a standard size (see the Figure 3.3 for the drawing).

The experimental setup and the die assembly were designed in cooperation with the Institute of Plasma Physics. While it is easy to manufacture a long graphite die, large radial forces in the middle of the die height caused by the piston pressure would lead to its failure at high temperatures. Therefore, an outer shell for the graphite die had to be manufactured from a Ti-Zr-Mo (TZM) alloy (supplied by Plansee) with a good creep resistance and high temperature strength. The whole assembly is shown in Figure 5.3.

Heat Treatment

We could not perform an absolutely equivalent in-situ ageing of the cast + forged (CF) rod inside the FAST furnace. However, for the sake of comparison, maintaining a similar thermal history for both sintered and CF conditions is crucial. As illustrated in Figure 5.4, the sintered rod (green line) was cooled directly to the RT after the sintering stage with no additional heat-treatment in the FAST device. Consequently, both sintered rod and as-received CF rod were heat treated together using the scheme shown in Figure 5.4 (green-purple line).

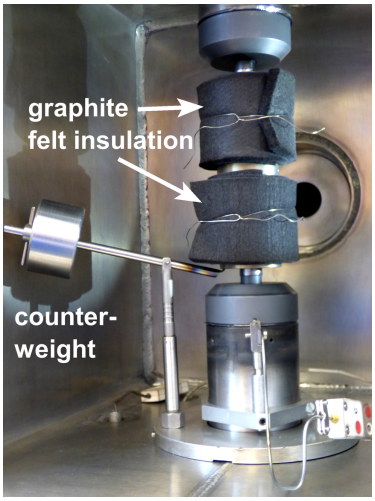

(a) The assembly within the sintering chamber prior to the sintering (the counterweight is necessary to prevent sliding of the heavy TZM housing down).

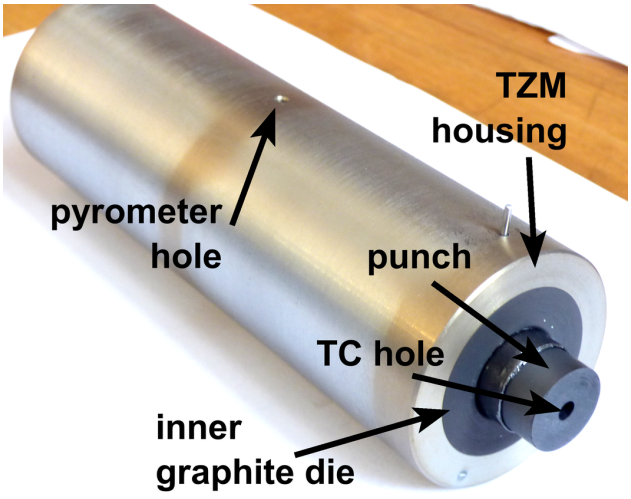

(b) A detail of the die design showing the inner graphite die in the TZM housing.

Figure 5.3: The experimental setup for high temperature sintering of large rods

This heat treatment was designed to imitate the in-situ ageing in the FAST furnace, namely the 'sintered + 600 °C' program in Figure 5.2 (the orange line), as closely as possible. However, simple heating to 600 °C from RT would be wrong, because the ageing temperature during in-situ sintering is approached from temperatures above the beta-transus temperature. Therefore, both rods (sintered and CF) must be exposed to the temperature above the beta-transus temperature before the final ageing step. A following procedure was designed: annealing treatment at 900 °C for 1 h, direct aging at 600 °C for 30 min and air cooling. Two pre-heated furnaces (at 900 and 600 °C) were used and the rods were encapsulated in a fused quartz tube under high vacuum to prevent any oxidation. The critical part is the change of temperature from 900 to 600 °C without undercooling.

A simple 1D temperature simulation of the cooling from 900 to 600 °C during the sample transfer between the two furnaces is plotted in Figure 5.5, along with the experimental temperature data of the in-situ ageing in the FAST furnace ('sintered + 600 °C' program, orange line in Figure 5.2). It can be clearly seen that while there are some differences, such as faster initial cooling of the samples transferred between furnaces, the steady state of 600 °C is reached after 10 min for both conditions. It can be therefore concluded that the designed alternative heat treatment method is a satisfactory representation of the in-situ ageing in the FAST furnace and that the samples of the first batch (small specimens) and second batch (rods) can be compared. This is also further justified by a microstructural correspondence, shown later in the Results and Discussion section.

The tensile tests were then performed at the rate of $10^{-3}\,s^{-1}$. For the tensile specimen geometry, please refer to the Experimental methods, section 3.5.2.

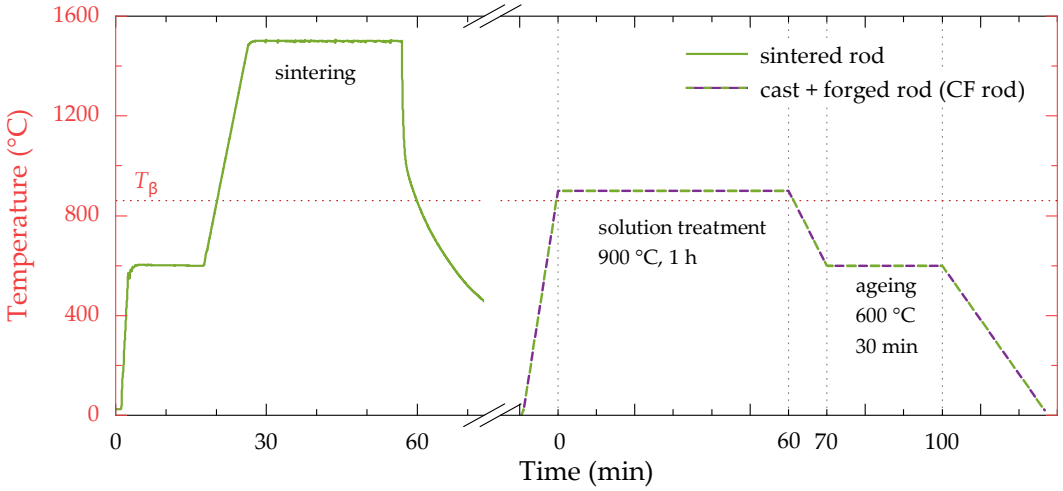

Figure 5.4: The heat treatment program for the samples used for measurements of mechanical properties. The green curve on the left, showing temperature evolution in the sintered rod, is the same one as that in Figure 5.2. The heat treatment is schematically drawn on the right. The points in circles (crossing 900 °C during cooling from sintering temperature and the end of solution treatment) correspond to microstructurally equivalent conditions, allowing to match the in-situ FAST aged samples with the conventionally heat-treated rods. T_β stands for the β transus of the alloy (845 °C).

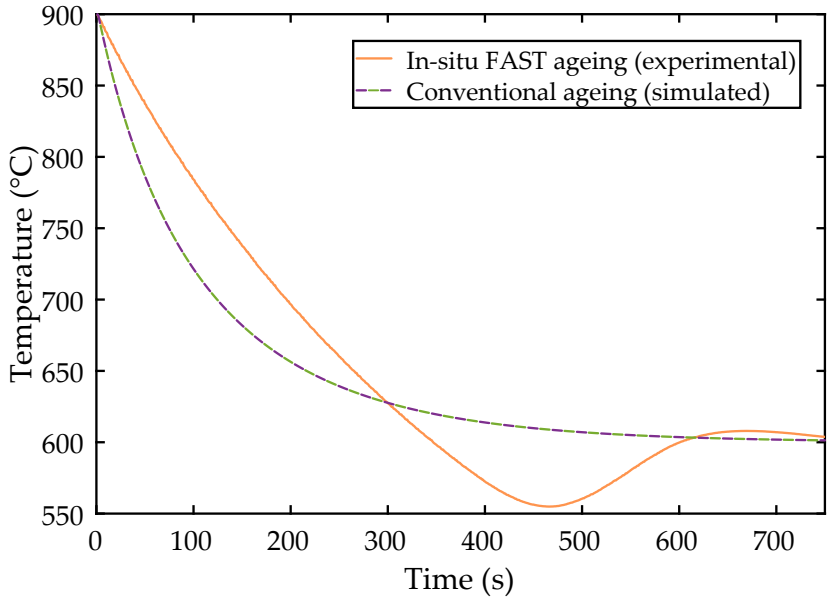

Figure 5.5: Simulated cooling of a cylindrical rod (15 mm in diameter, cylinder bases are neglected). Initial temperature was 900 °C, ambient temperature was set to 600 °C, only radiative heat transfer is permitted at the domain boundary (the rods are sealed in a fused quartz tube under high vacuum). The simulation data are plotted for the rod center ($r = 0$ mm) by a green-purple line, the experimental data of the 'sintered + 600 °C' program (cf. Figure 5.2) are plotted for comparison (orange line).

Table 5.2: The results of a chemical analysis by a carrier-gas hot extraction (CGHE) method on selected samples. The numbers in parentheses are standard uncertainties of the last digits calculated from measurements on three specimens. The data for the blended elements (BE) powder were calculated as weighted averages of the measured powder data (given in Table 5.1): using the actual weight ratios for mixing. The composition of the prealloyed powder is shown again for comparison.

Material	Condition	O (wt%)	N (wt%)	H (wt%)
Prealloyed	1000 °C	0.099(1)	0.012(1)	—
Prealloyed	1400 °C	0.096(2)	0.012(1)	—
Prealloyed	1500 °C	0.095(3)	0.010(1)	—
Blended elements	1400 °C	0.320(9)	0.016(1)	—
Blended elements	1500 °C	0.199(14)	0.014(2)	—
Blended elements	1500 + 800 + 600 °C	0.191(5)	0.012(2)	—
Blended elements	1500 + 600 °C	0.187(6)	0.013(2)	—
Prealloyed	*powder*	*0.107(2)*	*0.015(1)*	*0.002(1)*
Blended elements	*powder (V by Goodfellow) calculated*	*0.232*	*0.012*	*0.002*

5.2 Results and Discussion

5.2.1 Microstructure Optimization

The as-sintered samples were subjected to chemical analysis, its results are summarized in Table 5.2. As the hydrogen concentration was low in the powders already and there is no source of possible hydrogen contamination during the sintering process, it was not measured in the bulk samples.

The oxygen concentration decreased during sintering of the PA powder with only negligible differences between the sintering conditions. The decrease can be attributed to desorption of volatile compounds (e.g. water vapor) from the powders during heating in vacuum. While the powders are measured with the adsorbed compounds, the measurement of the bulk samples is performed after the desorption takes place, i.e. without the adsorbed compounds. The negligible difference between the sintering temperatures proves that its increase does not have an impact on the oxygen contamination.

The oxygen concentration of the blended elements (BE) samples is significantly higher due to the higher contamination of the raw powders. The highest concentration is measured for the BE sample at 1400 °C, as the contaminated V powder was used, however the contamination was resolved only after the sintering. For comparison, theoretical contamination of blended elements powder is also calculated by summing the individual powder contaminations from

Table 5.1 for the BE samples sintered at 1500 °C (with the low-oxygen vanadium powder). This is shown at the bottom of Table 5.2. Despite V, Cr and Al powders having a relatively high oxygen concentration, the overall oxygen contamination is still determined mostly by Ti and Ti-15Mo (containing 0.16 and 0.20 wt% of O, respectively) alloy powders due to their high fractions in the alloy. However, the oxygen content of Ti compiles with the Grade 1 ASTM standard [43], which is the most strict in terms of O content. As in the previous case (PA powder), an overall oxygen content (around 0.19 wt%) is lower than expected from a rule of mixtures (0.23 wt%), which may be again attributed to desorption of volatile compounds during sintering. The difference is even more pronounced here than in the case of the PA powder, because V, Cr and Al have irregular shape and thus higher specific surface available for adsorption and desorption. Once again, only a negligible difference between the samples with different ageing regimes proves that the ageing does not influence the oxygen content of the material. The nitrogen contamination is low in all samples, corresponding to the low concentration of nitrogen in the raw powders.

As a next step, we have analyzed microstructures of the as-sintered samples (those without ageing steps). A total of five conditions were analyzed – the prealloyed (PA) powder sintered at 1000, 1400 and 1500 °C and the blended elemental powder sintered at 1400 and 1500 °C. 1000 °C was not used for sintering form BE powders, because the alloy would not chemically homogenize at this temperature [26, 30]. The low magnification micrographs are shown in Figure 5.6. Grain size of the PA powder increases with the increasing sintering temperature – from below 100 µm at 1000 °C (Figure 5.6a) up to 1 mm at 1500 °C (Figure 5.6d). The grains in the BE samples are generally smaller than in the PA samples sintered at the same temperature, ranging from 300 µm at 1400 °C up to 800 µm at 1500 °C. This is attributed to the higher oxygen content of the BE material, suppressing the β grain growth at the sintering temperature [125, 126].

No porosity was detected in any of the samples due to the high sintering temperature (the occasional black dots at the micrographs in Figure 5.6 are remnants of the polishing suspension). Commercially pure titanium can be typically sintered to full density at the temperatures around 800 °C [127], alloys with high concentration of refractory alloying elements, such as TNTZ alloy are sintered at 1100 °C [25, 128]. However, a touchstone of the sintering process is not reaching a full density in this case, but reaching a good chemical homogeneity. It can be immediately seen from the modulated brightness of the BE sample sintered at 1400 °C (Figure 5.6c), caused by a compositional contrast, that the chemical homogeneity of this sample is not sufficient.

EDS linescans were performed on both BE samples after sintering stage and on the PA sample sintered at 1500 °C as a benchmark. The linescan was measured over the length of 3.2 mm with a 10 µm step size. The measured concentrations are plotted in Figure 5.7 for each of the four alloying elements. It should be noted that a precise quantification is difficult due to overlapping Ti K, V K and Cr K peaks. Smoothing was carried out by a Savitzky-Golay filter with a 10-point window to filter out the noise. The standard deviations were then calculated from the smoothed data and are shown alongside the curves in Figure 5.7.

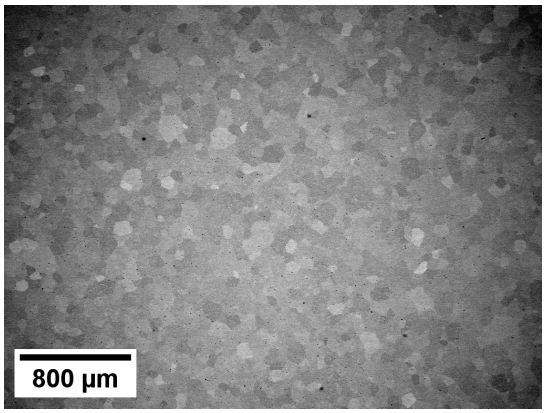

(a) PA, 1000 °C

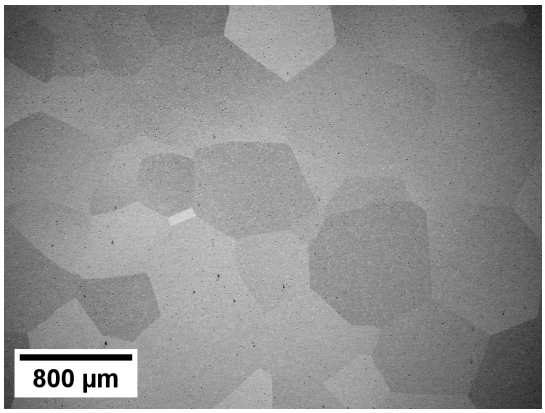

(b) PA, 1400 °C

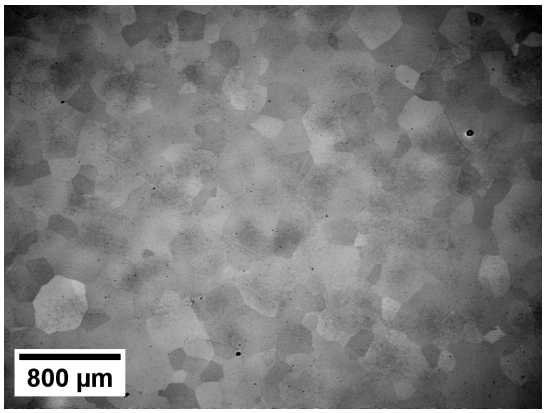

(c) BE, 1400 °C

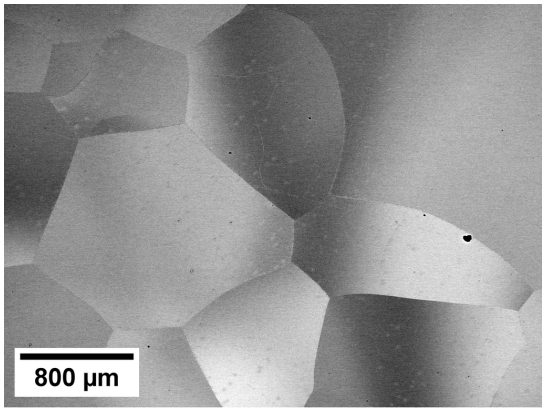

(d) PA, 1500 °C

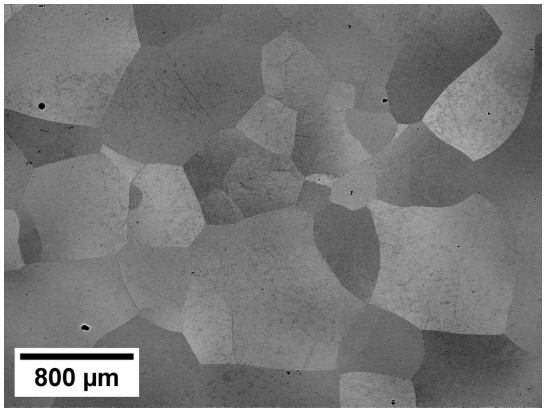

(e) BE, 1500 °C

Figure 5.6: BSE micrographs comparing the as-sintered Ti5553 alloy sintered under different conditions. The small black dots are remnants of the polishing suspension.

The homogeneity of the BE sample sintered at 1400 °C is significantly worse than the PA benchmark in all elements, most notably in V (0.97 vs. 0.09 wt%, respectively – a difference of an order of magnitude). This clearly indicates that 30 min at 1400 °C is insufficient for a full homogenization of the alloy.

The BE sample sintered at 1500 °C is significantly more homogeneous. The homogeneity is comparable to the benchmark PA sample in Al, Cr and Mo concentration, while the V concentration deviation is about two times higher. Nevertheless, the standard deviation of 0.24 wt% is still very good, provided

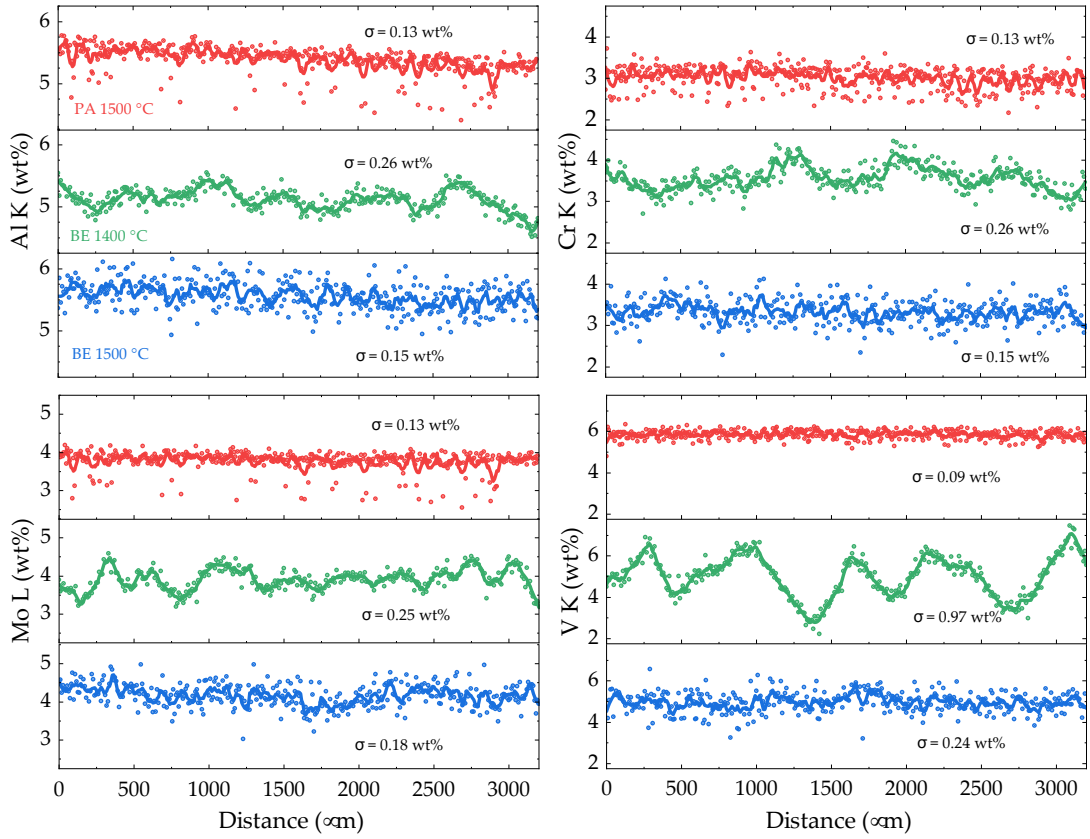

Figure 5.7: A comparison of EDS line profiles and standard deviations of concentrations of four alloying elements. The length of the line is 3.2 mm with 10 µm step size. The raw data were filtered using a Savitzky-Golay filter (shown as lines). The filtered line was used for calculation of σ.

that blended elemental powder was used as a feedstock. From now on, only the BE sample sintered at 1500 °C will be investigated and subjected to the in-situ ageing treatment.

The results of the microhardness measurements can be found in Table 5.3. All PA samples have the same microhardness within the measurement uncertainty. The microhardness of the BE sample is significantly higher than that of the PA samples (390 vs 290 HV, respectively). Moreover, the scatter of the individual measurements of the BE sample is larger. Both phenomena can be attributed to the higher oxygen content in the BE. The effect of oxygen is twofold: first, direct solid solution strengthening, and second, indirect effect through influencing the phase composition. SEM analysis was performed for further explanation.

The detailed SEM micrographs of the as-sintered conditions are shown in Figures 5.8a, b. It can be clearly seen that while the PA sample consists of almost single-phase β microstructure (with a minor fraction of grain boundary α), the BE sample has a two-phase α + β microstructure with very fine α lamellae. This is caused by an increased oxygen content in the BE alloy, which acts as a strong α stabilizer [41] and promotes precipitation of α phase during cooling. Some single phase β regions are preserved in the BE alloy (bottom of Figure 5.8b) thanks to the residual V concentration inhomogeneities (cf. Figure 5.7), which can shift the stability back towards β. These microstructural

Table 5.3: Comparison of a Vickers microhardness of the Ti5553 alloy prepared from prealloyed and blended elemental powders in the as-sintered condition.

Material	Condition	Microhardness (HV0.5)
Prealloyed	1000 °C	290 ± 5
Prealloyed	1400 °C	291 ± 5
Prealloyed	1500 °C	296 ± 7
Blended elements	1500 °C	391 ± 31

heterogeneities then influence the local microhardness and lead to the larger standard deviation of microhardness in the BE sample than in the PA sample (31 vs. 7 HV, respectively).

For the in-situ ageing experiments, the BE samples sintered at 1500 °C and the PA samples sintered at 1400 °C were selected, because their grain size is similar, allowing a direct comparison (Figures 5.6e and b, respectively). Two different ageing heat treatments were employed, as described above in the Material Preparation section. The microstructure of the aged samples is shown in Figures 5.8c–f.

The microstructure of the aged PA and BE samples is similar for both ageing schemes, despite the differences observed in the as-sintered condition. Both samples aged at 800 + 600 °C contain relatively large grain boundary α phase precipitates. These were formed during the 800 °C step, when the nucleation barrier in the grain interior was high and only heterogeneous precipitation at grain boundaries (GBs) as preferential sites was possible. The lamellar α phase particles precipitated in the grain interior during the 600 °C step. The lamellae in the BE sample are finer than in the PA sample. This is due to the higher O content, which increased the β transus temperature and increased the undercooling of the β phase matrix at the ageing temperature, leading to finer α precipitates.

The results of ageing at 600 °C are shown in Figures 5.8e and f. In the absence of the 800 °C step, there is only a small amount of the GB α, contrary to the two-step ageing. Similarly to the previous case, the α lamellae within the grains are finer in the BE sample due to the higher oxygen content and larger undercooling. Such lamellar $\alpha + \beta$ microstructure is commonly observed in the commercial alloys after ageing [49, 50].

The results of microhardness measurements on the aged samples are shown in Table 5.4, the results on the as-sintered samples from Table 5.3 are shown for comparison. There is a significant increase in microhardness of the PA samples from 291 HV in the as-sintered condition to 370 and 380 HV in the aged condition due to the change from the single-phase β microstructure to the two-phase lamellar $\alpha + \beta$ microstructure via precipitation strengthening. The single-step annealed PA sample exhibits slightly higher microhardness due to finer α lamellae (see Figures 5.8c and e).

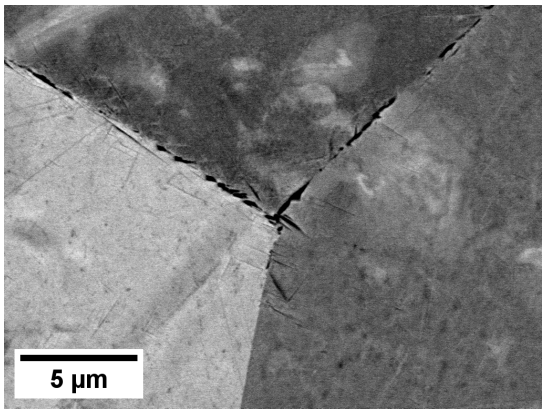

(a) PA, 1400 °C

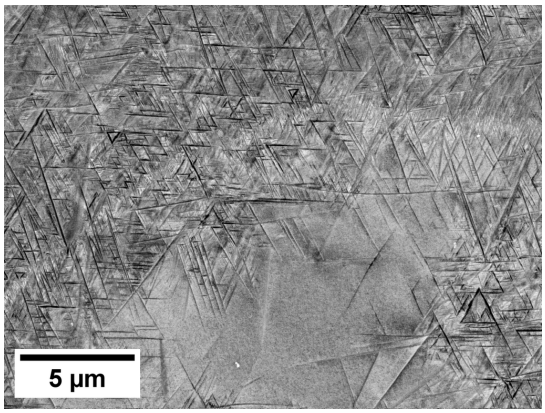

(b) BE, 1500 °C

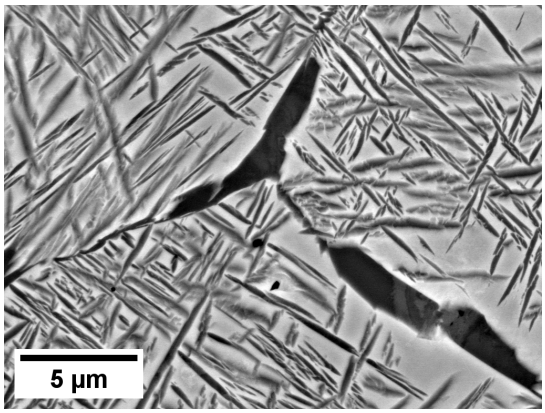

(c) PA, 1400 °C + 800 °C + 600 °C

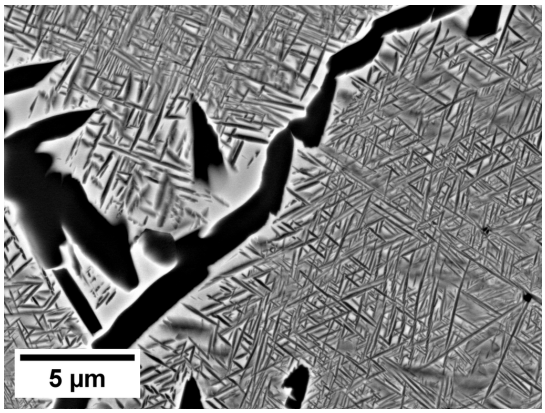

(d) BE, 1500 °C + 800 °C + 600 °C

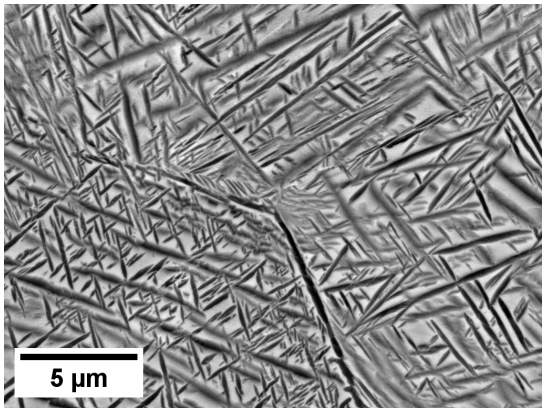

(e) PA, 1400 °C + 600 °C

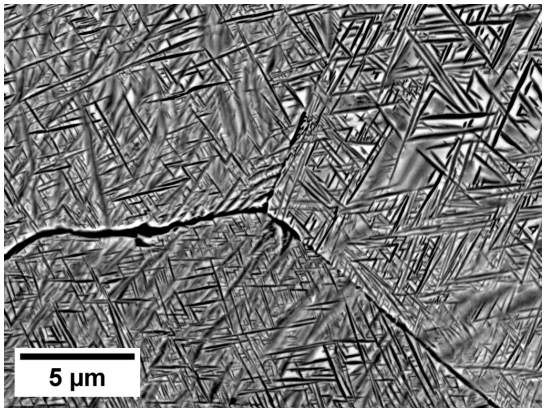

(f) BE, 1500 °C + 600 °C

Figure 5.8: The detailed BSE micrographs of the prealloyed (PA) and blended elemental (BE) samples after the different ageing schemes. Note that while the microstructure is significantly different in the as-sintered condition (a, b), the heat treatments smooth the differences and similar microstructure is produced for both manufacturing approaches – two-step annealing at 800 °C and 600 °C (c, d) and a single-step annealing at 600 °C (e, f).

Table 5.4: Comparison of a Vickers microhardness of the Ti5553 alloy prepared from prealloyed and blended elemental powders in the as-sintered condition.

Material	Sintering temperature	Ageing	Microhardness (HV0.5)
Prealloyed	1400 °C	as-sintered	290 ± 5
Prealloyed	1400 °C	800 °C + 600 °C	370 ± 5
Prealloyed	1400 °C	600 °C	380 ± 5
Blended elements	1500 °C	as-sintered	391 ± 31
Blended elements	1500 °C	800 °C + 600 °C	429 ± 10
Blended elements	1500 °C	600 °C	421 ± 10

The increase in the microhardness of the BE samples is smaller, but only because the microhardness of the as-sintered sample was already high. The microhardness of the aged samples increased from 391 HV to 429 and 421 HV, but the standard deviation decreased from 31 to 10 HV. This is due to more homogeneous microstructure, which now consists only of the lamellar $\alpha + \beta$ microstructure, without any regions with β phase only, observed in the as-sintered sample (Figure 5.8b).

A comparison of the corresponding PA and BE conditions shows that there is still a significant difference in microhardness (370–380 HV and 429–421 HV, respectively), despite the almost identical microstructure. This is caused by higher oxygen content in the BE alloy (cf. Table 5.2), causing solid solution strengthening in both α and β phases.

The presence of GB α is generally considered detrimental for mechanical properties of the alloy. Therefore, the single step ageing scheme was selected to prepare the sintered long rod with optimized microstructure, which will be used to measure the macroscopic mechanical properties.

5.2.2 Sintering of a Long Rod

It was shown in the previous section that the Ti5553 alloy can be sintered from the blended elemental powders, homogenized and aged in a single processing run, and that the microstructure and microhardness are comparable to the alloy sintered from the prealloyed powder. However, only a miniaturized specimen can be prepared from a standard-sized FAST sample, which is unsuitable due to relatively large grains in comparison with the specimen cross-section. Moreover, a standard-sized tensile specimen is desired for a reliable comparison with a conventionally produced alloy.

Therefore, a long rod (15 mm in diameter, 75 mm in length) was sintered by FAST and aged under the conditions imitating the in-situ ageing as closely as possible (Figure 5.9). This alloy was compared to the commercially available cast and forged (CF) Ti5553 alloy, which underwent exactly the same ther-

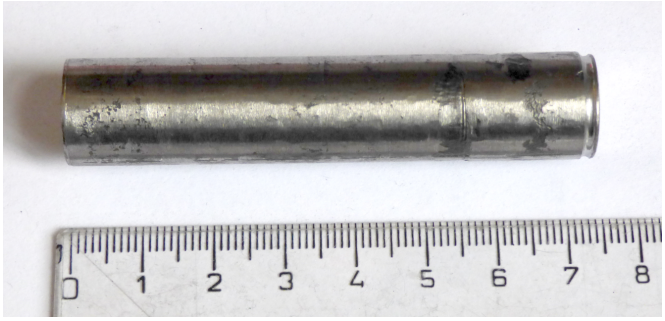

Figure 5.9: A photo of the as-sintered rod

mal processing as the sintered rod. The details were provided in the Material Preparation section of this chapter.

The content of oxygen and nitrogen was checked after the heat treatment in both FAST and CF rods, the results are presented in Table 5.5. The O concentration of the sintered rod is higher than measured in the small specimens, but it corresponds to the concentration estimated from the powder composition (cf. Table 5.2). This could be caused by larger specimen size, which may slow down or prevent degassing of the powders during early stages of sintering, i.e. before the pores of the sample were closed. The value is also slightly larger than the maximum concentration allowed by the alloy specification (0.18 wt%) according to the TIMET datasheet for the CF material. The nitrogen concentration is low in both samples.

The microstructure of the sintered and CF rods was checked before the mechanical testing, the micrographs are shown in Figure 5.10. Both samples have a two-phase lamellar $\alpha + \beta$ microstructure, which is of the same scale and morphology, as was observed in the in-situ aged samples from the first series (Figures 5.8e, f). This validates the thermal simulation results and justifies the heat treatment scheme used. All samples are assumed to represent the same microstructural condition and can be directly compared to each other.

Finally, the tensile specimens were manufactured according to the drawing (Figure 3.3). Two specimens were planned for each sample, but one of the sintered specimens was damaged during preparation and thus not measured. The resulting true stress-strain curves are shown in Figure 5.11a. Both samples exhibit a high yield stress of 1215 ± 4 MPa (CF sample) and 1183 MPa (sintered sample). Moreover, a moderate ductility of 6 % in tension was mea-

Table 5.5: The measured oxygen and nitrogen content of the rod samples for tensile testing. Three measurements were performed for each material. Standard uncertainties of the last digits are given in the parentheses.

	O (wt%)	N (wt%)
Cast + forged rod	0.164(11)	0.007(1)
Sintered rod	0.231(24)	0.005(1)

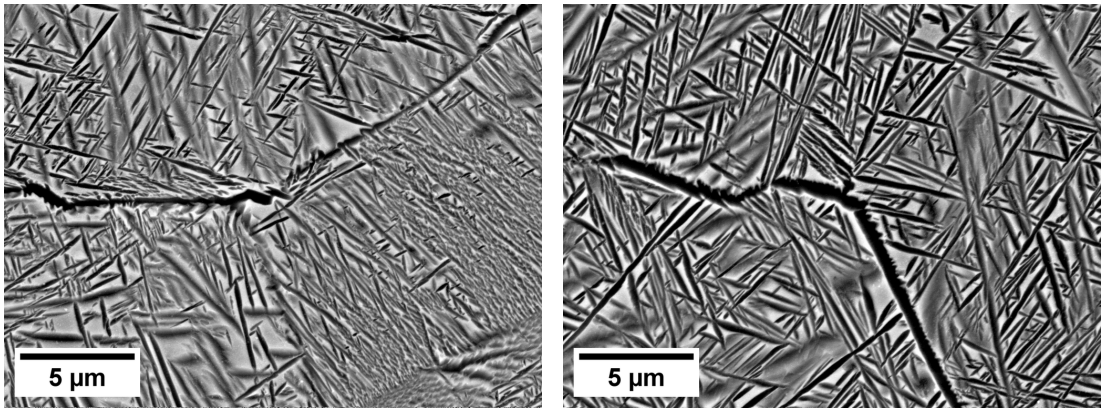

(a) Cast + forged + heat treated (b) Sintered + heat treated

Figure 5.10: The microstructure comparison of the CF and sintered rods (BSE micrographs)

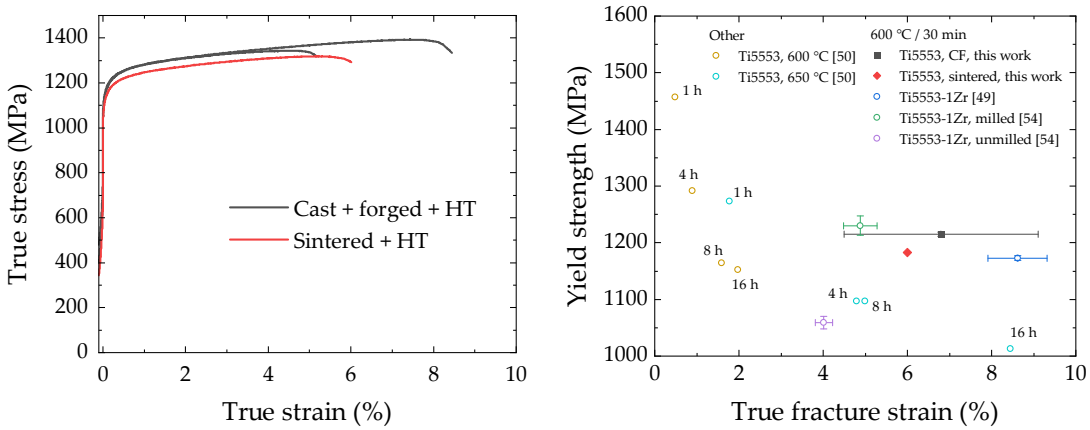

(a) The stress-strain curves

(b) Comparison of the measured yield stress and ductility with available experimental data. The ageing temperature and time is plotted for the datapoints from [50].

Figure 5.11: Results of the tensile test: a comparison of conventionally prepared and sintered Ti5553 rods and comparison with the earlier results after various heat treatments. The mechanical properties of the sintered material are comparable to the cast and forged alloy and to the properties measured on a similar Ti5553-1Zr alloy.

sured for the sintered sample, being comparable with the CF sample, reaching $6.8 \pm 2.3\,\%$. The measured values are plotted in Figure 5.11b and compared with the available literature data.

It is clearly visible that the alloy sintered from the BE powder matches the properties of the conventionally produced similar Ti5553-1Zr alloys, which underwent the identical heat treatment [49, 54]. The values of ductility and strength also exceed those obtained after longer ageing in [50]. The optimal combination of the yield strength of $1000 - 1100\,\mathrm{MPa}$ and ductility of $8 - 16\,\%$ in tension was reported in [50] after more complex heat treatment with an additional intermediate ageing step.

5.3 Summary

We have shown that a fully dense and homogenous Ti-5Al-5V-5Mo-3Cr alloy can be prepared by FAST sintering at 1500 °C from the blended elemental powders. No additional contamination occurred during sintering. After the consolidation, the alloy can be in-situ aged in the FAST device at 600 °C (without intermediate cooling to the RT), resulting in a homogenous two-phase lamellar $\alpha + \beta$ microstructure.

Using an in-house designed sintering assembly, the sintering process can be upscaled for production of long rods. This rod exhibited the high yield strength of 1183 MPa and the ductility of 6 % after ageing scheme simulating the in-situ ageing in the FAST furnace. These results are fully comparable with the commercially produced (cast and forged) material.

The proposed sintering method integrates three steps into a single processing run: the sintering, homogenization and ageing. The possibility of upscaling opens the door for near-net shape production of small, but complex specialized parts, such as fasteners in aerospace industry.

The results presented in this chapter were published in Metallurgical and Materials Transactions A:

Kozlík, J., Preisler, D., Haasová, M., Stráský, J., Chráska, T. & Janeček, M. Mechanical Properties of Ti–5Al–5V–5Mo–3Cr Alloy Sintered From Blended Elemental Powders. *Metallurgical and Materials Transactions A*. ISSN: 1543-1940. DOI: 10.1007/s11661-023- 07048-2 (2023).

Since we have now demonstrated the viability of the BEPM approach, we should exploit it even further – by preparing materials with a compositional gradient by deliberately using lower sintering temperature and slowing the homogenization. The gradient in concentration can be used to optimize the alloy composition towards the desired microstructure and this optimized alloy can be then prepared as a homogenous sample for further investigations.

This will be a topic of the next chapter.

6 Blended Elemental Powder Metallurgy of Ti-Nb-Zr-O Alloys

We have demonstrated in the previous chapter that using blended elemental powder metallurgy (BEPM) to sinter Ti alloys is a viable approach. Now we would like to use the method to investigate the Ti-Nb-Zr-O alloying system – a biocompatible system that has been thoroughly studied at our department. Multiple phases can form in the alloy following rather complex transformation paths, strongly depending on the alloy's chemical composition and thermal processing history. The purpose of the BEPM approach is twofold: it is a tool for easy tuning the chemical composition in homogeneous samples, and moreover, by controlling the level of homogenization, compositionally heterogeneous samples can be prepared to observe the composition-dependent microstructural features in a single sample. Such an approach is an example of high-throughput methods.

In the first part, we will show how can the alloy composition be optimized using heterogeneous samples. We try to make use of the fact that Nb, as a main β stabilizing element in the studied alloys, also has the slowest interdiffusion in the alloy. Therefore, it homogenizes as the last element and gradients in the Nb concentration can be easily prepared. Phase composition can then be investigated along this Nb gradient and the chemical composition measured at regions of interest.

In the second part, several homogeneous alloys within the compositional range of interest determined in the first part (having different Nb and O concentrations) will be prepared by BEPM and subjected to phase and mechanical properties analysis.

6.1 Material Preparation

The alloy was prepared using blended elemental powder metallurgy. Properties of the raw powders are summarized in Table 6.1. Two Nb powders are listed in the table. The first one, with a broad size distribution (up to 500 µm), was used for sintering samples with a compositional gradient, ensuring that the alloy would not homogenize completely. In contrast, the second one has a smaller size to enhance the homogenization rate to prepare homogeneous samples. TiO_2 was introduced as a controllable source of oxygen, an approach used in recently published papers [129, 130].

Zr Grade 702 is a commercially pure grade of Zr, which may contain a small amount of Hf. These elements are chemically similar, and their separation

Table 6.1: The powders used for sintering. The particle size and morphology are taken from the supplier's datasheet, the chemical contamination was measured independently by CGHE (carrier gas hot extraction) method. The numbers in brackets are standard deviations of three measured specimens. An accurate measurement of O content in TiO_2 was not possible by this method.

Powder	Manufacturer	Particle size & morphology	O (wt%)	N (wt%)	H (wt%)
Nb (for heterogeneous sample)	Alfa Aesar	irregular $20 - 500\,\mu m$	0.240(40)	—	—
Nb (for homogeneous samples)	Alfa Aesar	irregular $< 44\,\mu m$	0.412(1)	0.073(1)	0.047(1)
Zr (Grade 702)	TLS Technik	spherical $20 - 80\,\mu m$	0.175(1)	0.009(1)	0.001(1)
TiO_2 (anatase)	Sigma Aldrich	agglomerated $< 1\,\mu m$	—	0.004(2)	0.017(3)
Ti Grade 2	TLS Technik	spherical $20 - 80\,\mu m$	0.177(4)	0.008(1)	0.001(1)

is expensive and therefore performed only when necessary, i.e., for nuclear applications.

The chemical contamination was measured by CGHE (except for Nb for heterogeneous samples when the measurement was unavailable and the supplier's value was used). Contamination of Ti and Zr is within the limits of commercial purity. Contamination of Nb for homogeneous samples is relatively high for all elements, mainly caused by its irregular morphology and a large specific surface area. All handling was performed in the air.

The powders were mixed using an in-house built rotational mixing device (a half-filled vial, eccentrically placed in a rotating drum). The morphology of the powders and the homogeneity of the blend is shown in Figure 6.1, along with the corresponding EDS map. The blend is well mixed and the individual powers are well dispersed, showing no clustering.

6.1.1 Heterogeneous Samples

A powder blend with a nominal composition of Ti-29Nb-7Zr-0.8O (wt%) was prepared. Approximately 9 g of powder was filled into a graphite die (15 mm in diameter). Graphite foils were used as spacers between the sample and the die.

The sintering program started with heating at the rate of 200 K/min up to the temperature 50 K below the sintering temperature when the rate was reduced to 50 K/min to avoid overshooting the target temperature. Then, the piston pressure was increased to 80 MPa and the isothermal stage of the sin-

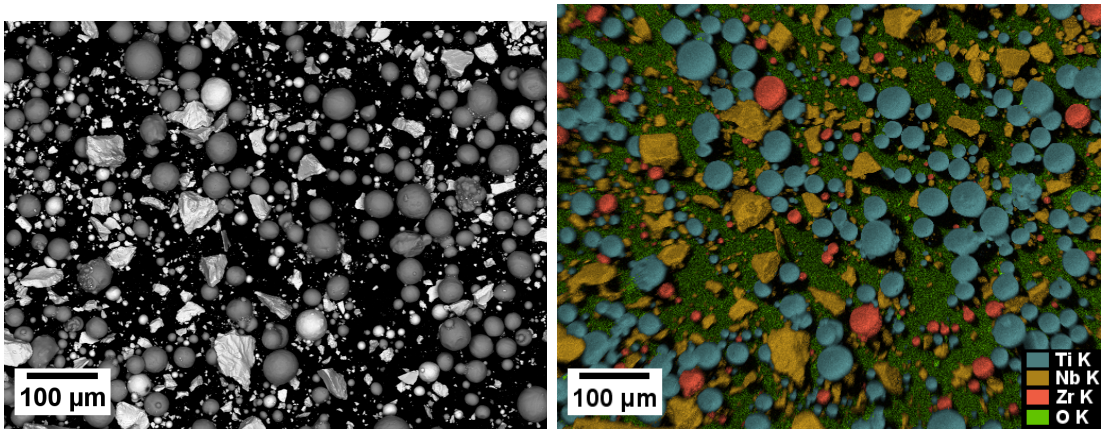

(a) SEM BSE micrograph (b) EDS map

Figure 6.1: The powder blend for sintering of heterogeneous samples showing the size and morphology of the individual elemental powders.

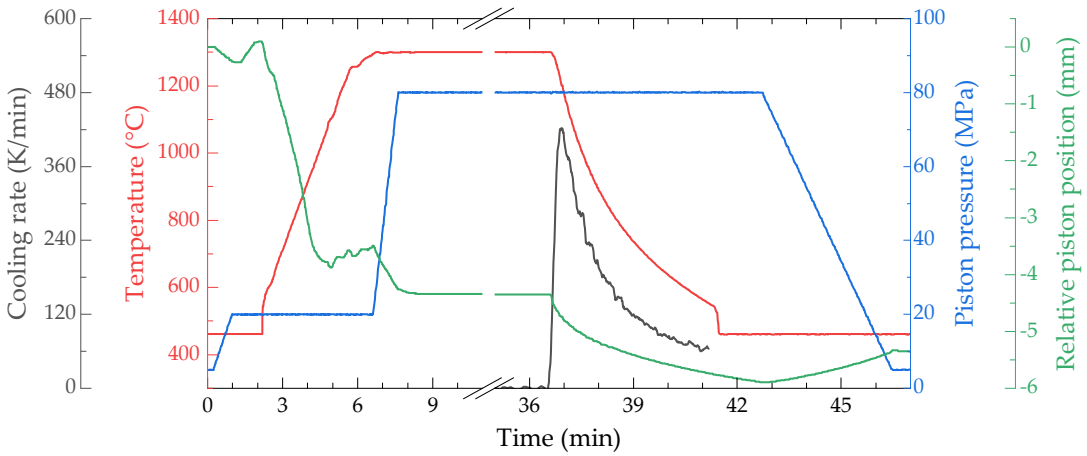

Figure 6.2: Process parameters during the sintering program for the heterogeneous samples (1300 °C for 30 min shown); isothermal part is shown in a reduced length. The cooling rate is also plotted for the cooling stage, it is reproducible for all samples. The pyrometer readings below 600 °C are not reliable and should be used with caution.

tering was carried out. Three samples were prepared at different conditions: 15 min at 1300 °C, 30 min at 1300 °C and 15 min at 1400 °C. The isothermal part was followed by free cooling with a cooling rate of approximately 200 K/min at 800 °C and around 100 K/min at 600 °C; the cooling rate is comparable to air cooling. The actual course of the critical process parameters is shown in Figure 6.2 for the sample sintered at 1300 °C for 30 min. The green line shows the piston movement relative to the initial position (negative = compression). The curve flattens quickly during the isothermal stage, indicating that full density is reached within the first few minutes. The as-sintered cylindrical samples are 15 mm in diameter and approximately 7 mm in height.

6.1.2 Homogeneous Samples

Five compositions were selected based on the results obtained from the analysis of the heterogeneous sample: four with a varying Nb content Ti-**[20,23,26,29]Nb**-7Zr-**0.7O** (wt%) and one with lower O content (Ti-**23Nb**-7Zr-**0.2O** (wt%)). This is achieved by omitting TiO_2 from the powder blend, the residual O content being determined solely by the chemical composition of the raw powders (see Table 6.1), which is about 0.2 wt% of O. Approximately 30 g of the powders per sample was filled into the 30 mm graphite die, yielding samples of 10 mm in height. Graphite foils were used as spacers between the sample and the die.

The sintering program is similar to the program of the heterogeneous samples with a few alterations: the isothermal sintering stage is at 1500 °C for 30 min for all samples and the piston pressure was reduced to 50 MPa to limit the creeping of the alloy into the gaps of the sintering die. The process parameters are plotted in Figure 6.3. The cooling rate is about 50 % lower than in the case of heterogeneous samples (100 K/min at 800 °C) due to a larger sample and assembly. This condition is further referred to as the as-sintered (**AS**) condition.

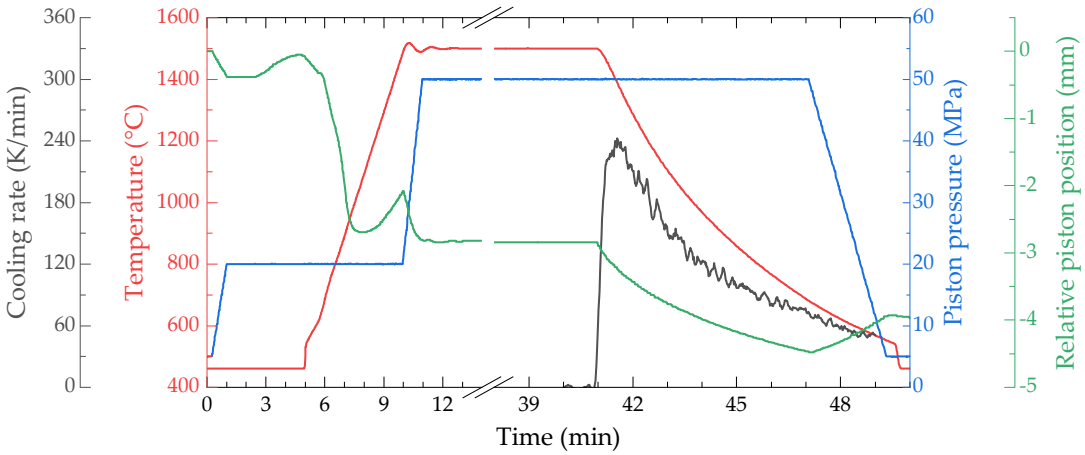

Figure 6.3: The sintering program of the homogeneous samples. The isothermal part is shown in a reduced length. The cooling rate is also plotted for the cooling stage, it is reproducible for all samples.

The samples were cut in half. One half was then subjected to additional solution treatment at 1000 °C for 2 h and water quenched to investigate the influence of composition on martensitic transformation. This condition will be referenced as the **ST+WQ** condition.

The samples for transmission XRD were prepared by mechanical grinding and polishing down to the thickness of 0.3 mm. The samples for the RUS measurements were cut and ground to the cuboidal shape of 2 mm × 3 mm × 4 mm.

All samples for SEM and microhardness measurement were prepared with SiC papers grinding up to #2000 grit. The final polishing was performed using a Vibromet vibratory polisher in three steps – 8 h in 0.3 µm Al_2O_3 suspension, 8 h in 0.05 µm Al_2O_3 suspension and 4 h in 0.05 µm SiO_2 colloidal suspension.

All TEM samples were prepared as lamellae from the specific region of interest by the FIB method.

6.2 Results

6.2.1 Heterogeneous Samples

The samples were successfully consolidated using the above-described sintering conditions. Chemical contamination was measured in the samples sintered for 15 min at 1300 °C and 1400 °C, assuming that the value of the third sample would be in the measured range. Two specimens were measured for each sample, cut from the central region of the sample (to rule out any effect of carbon contamination at the sample boundaries in contact with the graphite foil and die). The results are presented in Table 6.2. The oxygen content does not differ significantly between the two samples, indicating that sintering at higher temperatures does not induce additional contamination. The concentrations of N and H are within acceptable limits for Ti alloys.

The low-magnification SEM images of the as-sintered microstructure are presented in Figure 6.4. The microstructure of all samples is strongly heterogeneous as intended. Undissolved Nb particles (appearing white) are the major feature visible in all samples. Around them, a Nb-rich shell with a single phase β microstructure is formed (appearing grey). Finally, in the regions far from the Nb particles, a two-phase $\alpha + \beta$ microstructure is present, appearing as noisy, dark grey regions. These will be shown below in detail.

Residual porosity was found only as preexisting pores in the undissolved Nb particles, while virtually no pores can be found in the β and $\alpha + \beta$ regions. This is due to comparatively high sintering temperatures close to the melting point (1670 °C for pure Ti [41] and approximately 1750 °C for the Ti-29Nb-7Zr-0.8O alloy (by ThermoCalc)). It was already shown that even more demanding Ti-Nb-Ta-Zr alloys can be readily sintered to full density even at 1100 °C [128]. The occasional black dots are remnants of the polishing suspension.

Because the Nb gradient is similar in all samples, the following investigations were performed on one of them – the sample sintered at 1300 °C for 30 min.

An SEM micrograph + EDS map is shown in Figure 6.5 to show that the bright particles are undissolved Nb particles. No Ti was detected in their in-

Table 6.2: Carrier gas hot extraction analysis of two sintered samples. Two specimens were measured for each sample. It is assumed that the values of the 1300 °C / 30 min sample are within the range between by these two measurements.

Material	O (wt%)	N (wt%)	H (wt%)
1300 °C, 15 min	0.826(35)	0.016(1)	0.015(1)
1400 °C, 15 min	0.870(24)	0.015(1)	0.022(1)

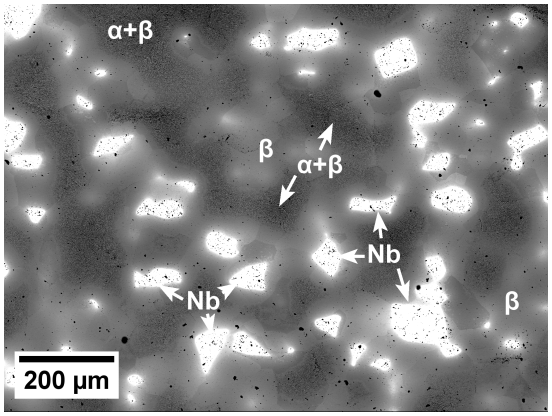

(a) 1300 °C, 15 min

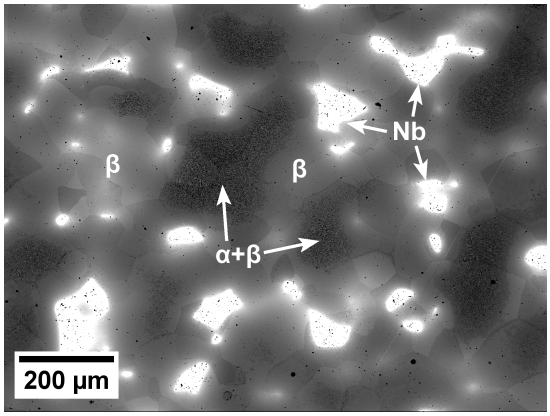

(b) 1300 °C, 30 min

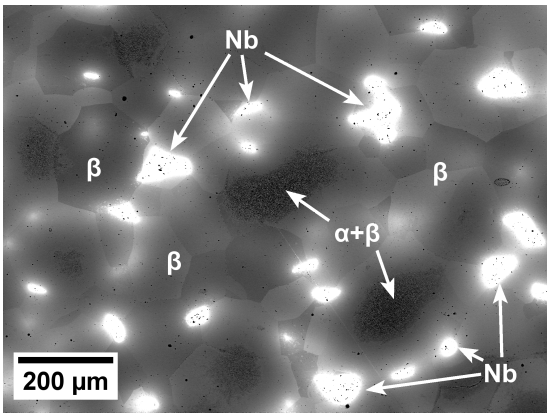

(c) 1400 °C, 15 min

Figure 6.4: Low magnification SEM BSE micrographs showing the heterogeneity of the as-sintered samples. White areas are undissolved Nb particles.

terior. Zr concentration is low and the Zr K line weak, so the relative homogeneity of the map is significantly affected by noise. The $\alpha + \beta$ microstructure is found in the regions far from the Nb particles with lower Nb concentration.

A detail of the microstructural gradient between the $\alpha + \beta$ and β regions is presented in Figures 6.6a and b. An EDS linescan was measured across the gradient to show the range of chemical compositions observed; the results are plotted in Figure 6.6c. The scan is, in fact, performed over a narrow long rectangle (as indicated by black ticks at the end of the line) and composition is averaged across its width to smooth the influence of abrupt concentration changes between α and β. The whole micrograph in Figure 6.6a has an approximate range from $40 - 17$ wt% of Nb, with Zr content being constant and a balance of Ti.

Three different types of α precipitates can be identified in the micrographs: grain boundary alpha (α_{GB}), nucleating and growing along grain boundaries, alpha nucleating heterogeneously either directly at GBs or at the α_{GB}, but growing in a form of parallel lamellae into the grain interior (α_{htg}), and alpha nucleating in the grain interior (α_{int}). The detail of the GB in Figure 6.6b proves that GBs indeed serve as preferential nucleation sites, allowing precipitation of α_{GB} and α_{htg} at higher Nb concentrations compared to the grain interior.

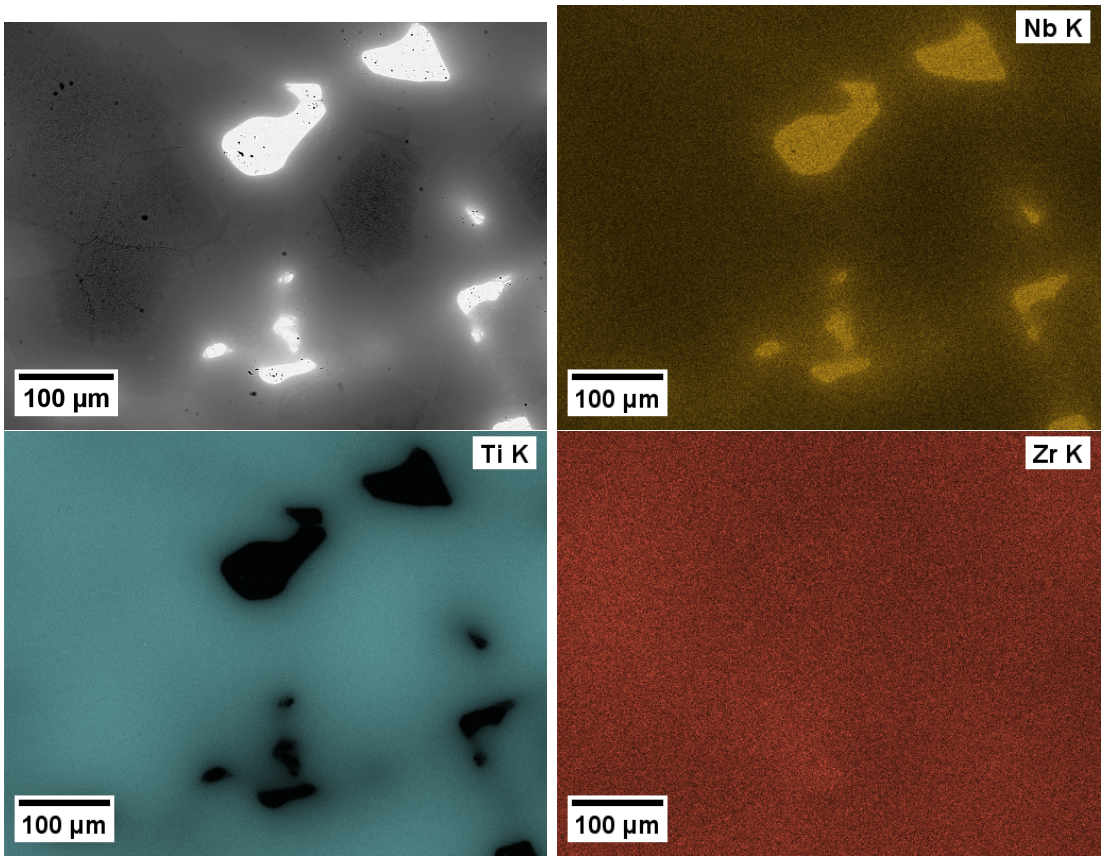

Figure 6.5: An EDS map of the sample sintered at 1300 °C for 30 min with the undissolved Nb particles and $\alpha + \beta$ microstructure in between them in the Nb lean regions.

Size of all α precipitates decreases with increasing Nb concentration, which is predominantly caused by the temperature at which the precipitation takes place given the Nb content. During cooling, α_{GB} always precipitates first as its activation energy is lower at the GB. α_{htg} precipitates at α_{GB} shortly after and starts growing into the grain interior until it meets α_{int}. Nucleation of α_{int} is slower, because the activation energy inside the grain is higher. With decreasing temperature, growth rate of α lamellae decreases due to the slower diffusion, while the nucleation rate increases due to larger undercooling and larger driving force. This leads to more uniform precipitation of smaller α lamellae, limiting the length of α_{htg}. The detail in Figure 6.6b shows the very early stages of nucleation, with just the α_{GB} and α_{htg} present.

The critical concentration of Nb, which is sufficient to suppress precipitation of α phase during cooling is of a great interest from both theoretical (providing information about the alloy phase diagram) and technological (controlling the microstructure) point of view. Figure 6.6c places this concentration between 20 and 25 wt% of Nb, but a different measurement method is necessary for its accurate determination.

First, the concentration should be averaged over a small area at the interface to rule out any effect of the exact positioning. An example of such area is shown in Figure 6.7. Three such areas at different positions were measured in each sample, a single EDS spectrum for each of them.

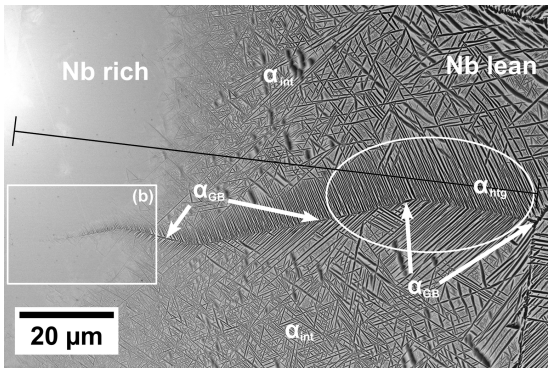

(a) Overview of the area with different α morphologies

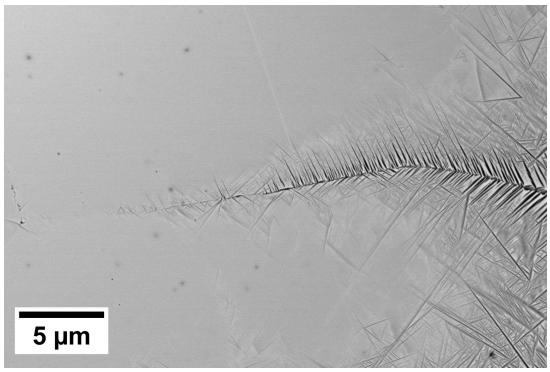

(b) A detail of the GB microstructure marked in (a)

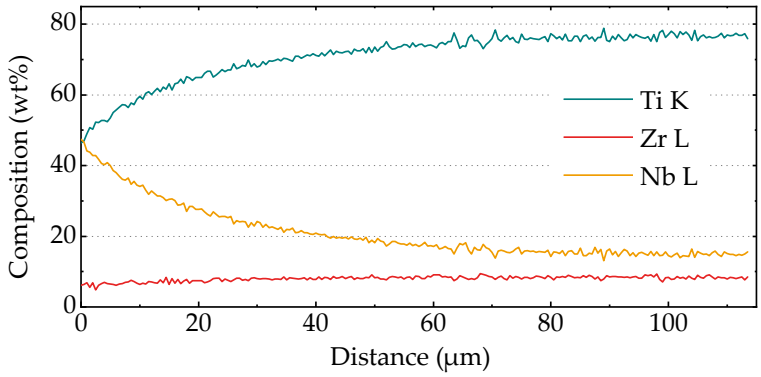

(c) EDS line concentration profile along the black line in (a) showin the Ti/Nb gradient

Figure 6.6: BSE micrographs and EDS composition profile of the microstructural gradient. α morphology at regions with different Nb content, showing the varying lath thickness. The black line marks the position and width of an EDS line profile presented in (c).

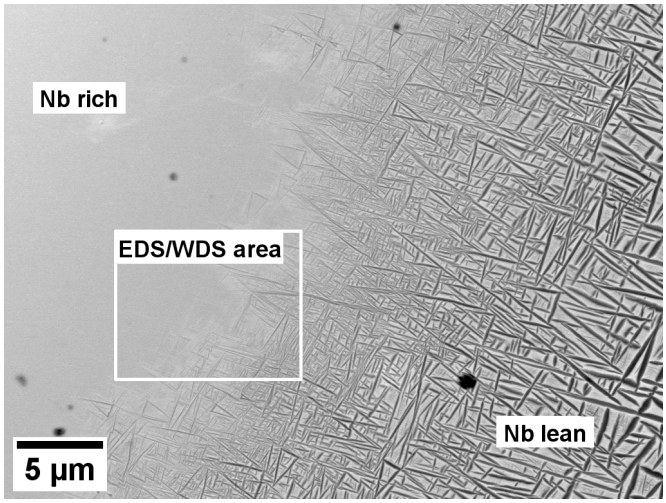

Figure 6.7: A transition region between β and α + β regions with a rectangle showing the approximate positioning and size of the WDS and EDS area scans.

Table 6.3: Composition at the interface of β and α + β region as measured by EDS and WDS. The values are averages of three regions similar to the one shown in 6.7. The errors in brackets (Nb) also include errors from the area positioning (more explanation in the text).

Sample	Method	Ti (wt%)	Nb (wt%)	Zr (wt%)
1300 °C, 15 min	EDS standardless	71.9 ± 0.8	18.6 ± 0.4 (± 0.7)	8.8 ± 1.1
1300 °C, 30 min	EDS standardless	72.9 ± 1.4	20.6 ± 0.9 (± 1.1)	5.8 ± 0.5
1400 °C, 15 min	EDS standardless	71.7 ± 0.7	20.0 ± 0.1 (± 0.6)	7.5 ± 0.7
1300 °C, 30 min	WDS standards	68.7 ± 1.0	22.2 ± 0.6 (± 0.8)	8.0 ± 0.3

Second, to avoid possible inaccuracies caused by overlapping Zr L and Nb L peaks, which must be deconvoluted during the standardless EDS quantification procedure, WDS analysis with elemental standards was also performed on similar areas in the 1300 °C / 30 min sample as a reference. The results of all analyses are summarized in Table 6.3. It is not possible to accurately measure the oxygen content by neither of the methods, so the values from Table 6.2 were used for recalculation.

The uncertainty from the positioning of the rectangle in Figure 6.7 was estimated by measuring the difference in composition across the whole micrograph diagonally. This is approximately 3 wt% of Nb, giving the difference across the EDS/WDS area of 0.5 wt%. This additional uncertainty is added to the measurement deviation and the result is given by the number in parentheses in Table 6.3.

It can be seen that the concentration of Ti is slightly overestimated by EDS when compared to WDS (72.9 vs. 68.7 wt% of Ti, respectively). Thus, the critical concentration of Nb suppressing the α precipitation in this alloy is 22.2 ± 0.8 wt%, according to WDS.

The ECCI micrographs of the transition region are shown in Figure 6.8. The primary β grain forms a darker gray background on the right-hand side of Figure 6.8a, well developed α lamellae are observable on the left-hand side of the picture and a layer of brighter lamellae is found in between. The detail of this transitional region is shown in Figure 6.8b. There are two triangularly arranged dark α lamellae surrounded by other lamellae which are much brighter. The α lamellae forming the triangle are depleted of Nb and thus appear darker than the surrounding β matrix. However, no precipitating phase in Ti alloys is known to be enriched with Nb. Hence, the bright lamellae cannot be visible due to the chemical contrast, but due to the orientation/phase contrast and must be depleted of Nb much less than the stable α triangle.

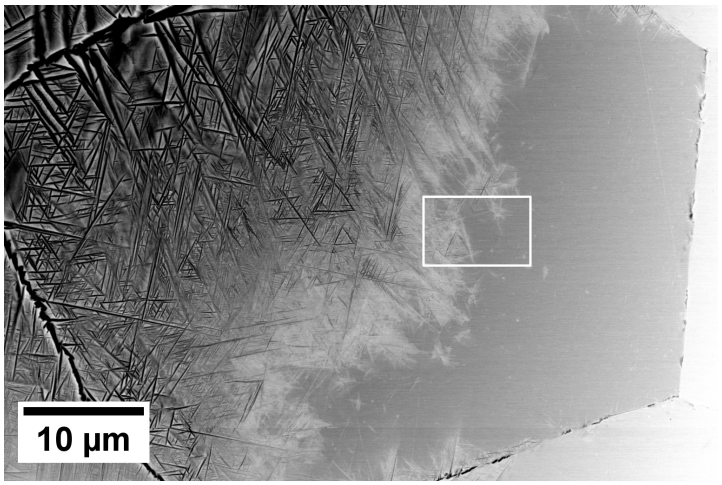

(a) An overview of the transition region

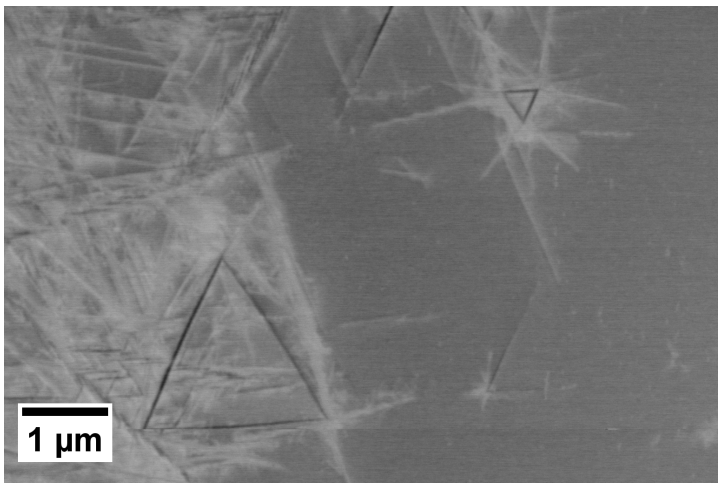

(b) A detail of the area marked in (a)

Figure 6.8: ECCI/SEM micrographs of the transition region with the parent β grain in the channeling orientation. The dark lamellae correspond to the stable α precipitates.

To confirm the phase composition at the boundary, a lamella was prepared by FIB from the 1300 °C / 30 min sample and investigated by TEM. The low-magnification BF and DF micrographs are shown in Figure 6.9a and d, respectively (a stich of three micrographs). The left side is Nb lean ($\alpha + \beta$ region), the right side is Nb rich (β region). The boundary is not very sharp at this scale and isolated α precipitates can be found in the β region as well, growing in clusters around what is probably a preferential nucleation center. A selected area electron diffraction (SAED) was done in the two regions with the results shown in Figures 6.9b and c. It turns out that apart from β or α phases, both regions contain hexagonal ω phase (marked by green hexagons in the SAED patterns). The dark-field micrograph was taken using the ω reflection marked by the dashed circle in Figure 6.9c, shown in Figure 6.9. ω phase is present in large amount in all β matrix, even between the α lamellae in the $\alpha + \beta$ region.

Two regions, marked A and B in Figure 6.9d, were imaged at higher magnification and the DF micrographs are presented in Figure 6.10, showing the ω particles. The particle size is approximately 30 nm in diameter and particles are almost round, corresponding to the chemically stabilized isothermal

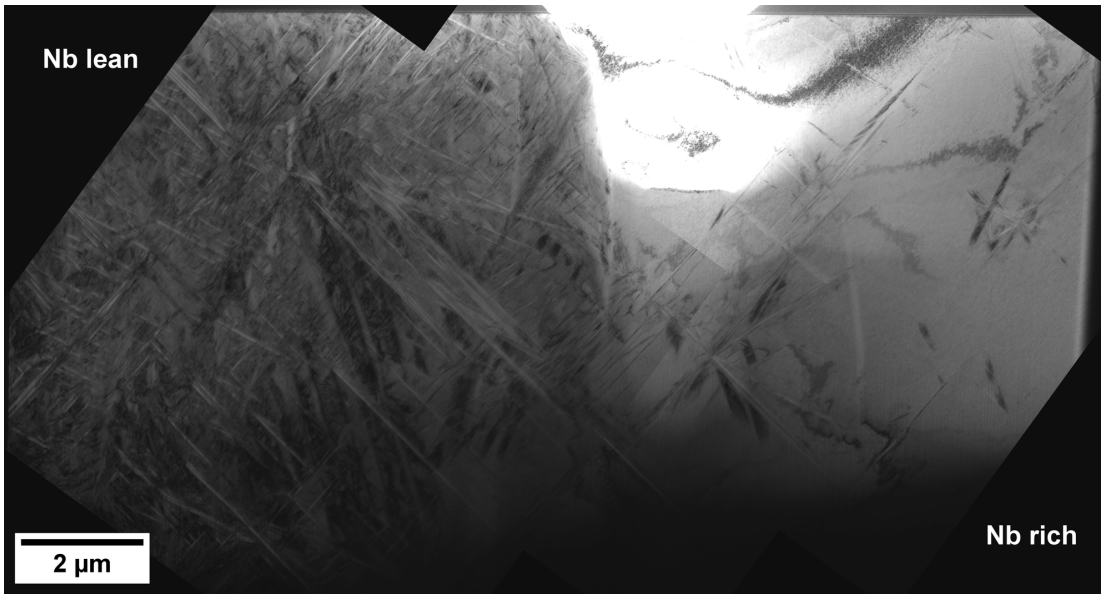

(a) An overview BF micrograph (image gamma adjusted to partially compensate for the non-uniform lamella thickness)

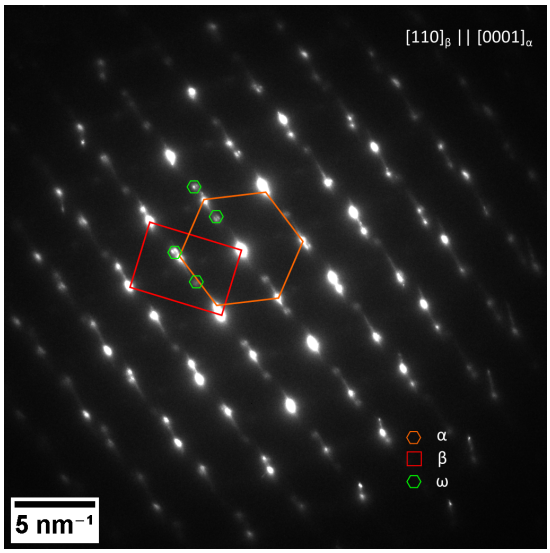

(b) SAED pattern of $[110]_\beta$ zone axis, $\alpha + \beta + \omega$ phases present

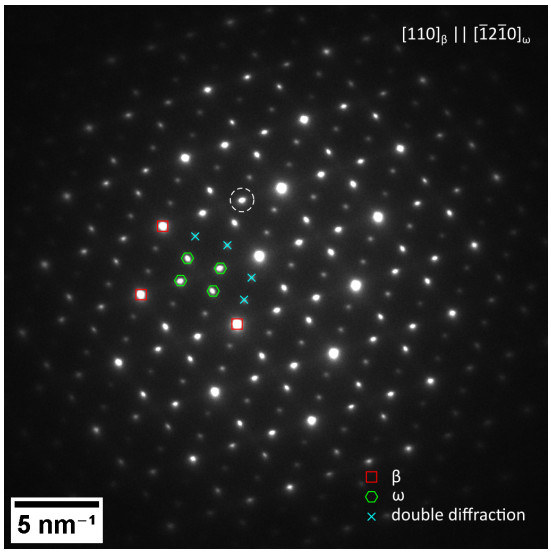

(c) SAED pattern of $[110]_\beta$ zone axis, $\beta + \omega$ phases present

Figure 6.9: TEM investigations of the interface between β and $\alpha + \beta$ regions. The lamella was prepared from the sample sintered at 1300 °C for 30 min.

ω_{iso} particles. This also correlates well with the narrow diffraction spots in Figures 6.9b and c.

We were also interested in the degree of chemical segregation between the α and β phases (the size of ω is too small compared to the X-ray interaction volume and thus the composition cannot be assessed). Three EDS linescans were performed along the lines marked 1–3 in Figure 6.9d and the data are shown in Figure 6.11, along with the corresponding STEM insets. The contrast in STEM is similar to the BSE signal in SEM, i.e. heavier elements (such as Nb) appear brighter. The results show a clear partitioning of Nb out of α particles with the concentration being $10 - 20$ wt% lower inside. Zr concentration is also

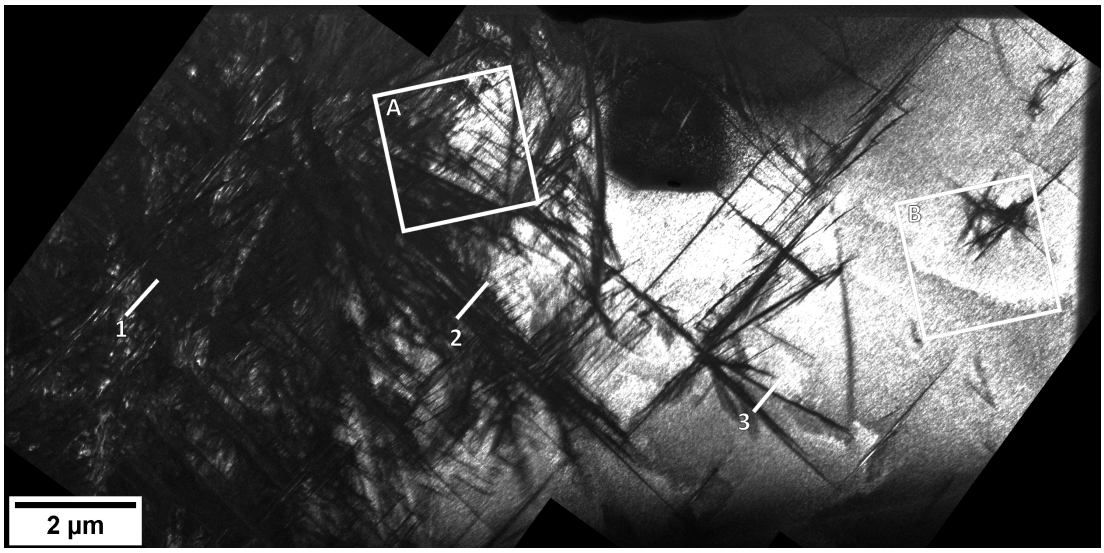

(d) DF micrograph of the lamella using ω reflection showing high density of ω particles in both β and α + β regions. Square areas A and B are shown in detail in Figures 6.10a and b, respectively, lines 1–3 mark the positions of the EDS line scans presented in Figure 6.11.

Figure 6.9: *(Continued)*

slightly lower, suggesting that Zr is only a weak β stabilizer. However, there are two lamellae on the left side of the line 3, which seem to be segregated much less – this may be caused either by their tilt towards the surface, or by observing the very early stage of precipitation when an extensive partitioning has not happened yet.

It was shown that the concentration of Nb at the boundary between α + β + ω and β + ω regions is 22 wt%. As a next step, homogeneous alloys will be prepared around this composition (20 − 29 wt% of Nb) with two different oxy-

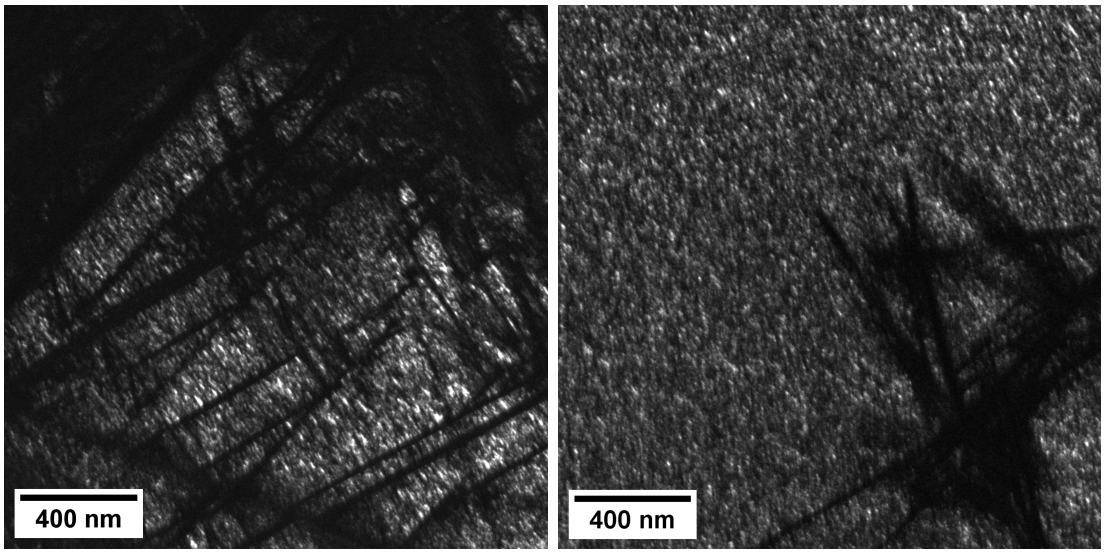

(a) Nb lean region, marked A

(b) Nb rich region, marked B

Figure 6.10: Detailed DF micrographs of ω particles in β matrix, regions marked in Figure 6.9d

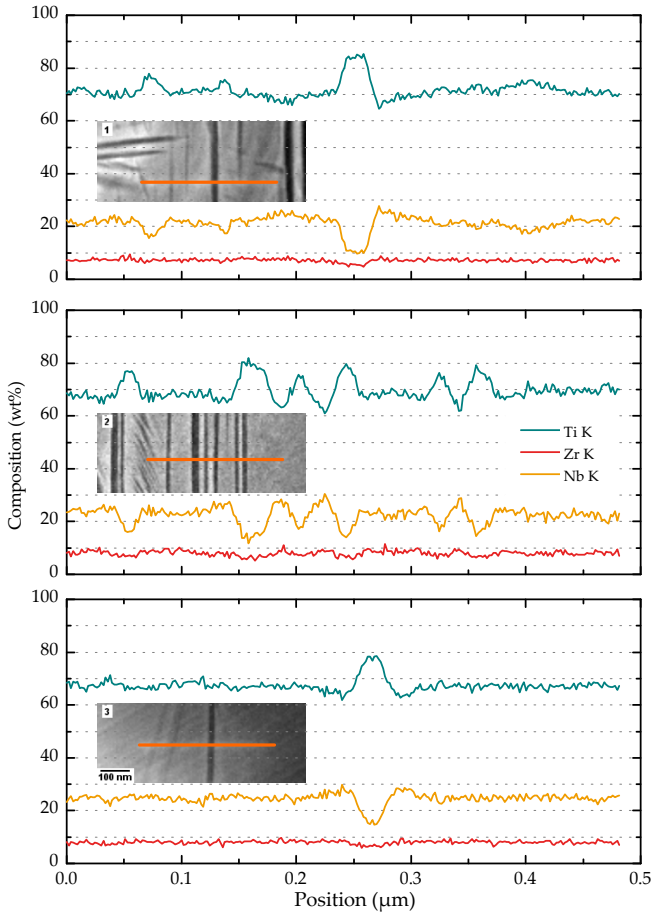

Figure 6.11: EDS line profiles from the three different regions of the lamella, marked in Figure 6.9d. The STEM insets are also shown to provide the correlation between the local composition and the phase present.

gen contents for further investigations by XRD and RUS methods, since these methods cannot be used for characterization of samples with local gradient at such small scales.

6.2.2 Homogeneous Samples

The samples were successfully sintered using the above-described sintering conditions. The chemical analysis of O, N and H elements was performed on all samples in the as-sintered (AS) condition, as each was prepared from a different powder blend. The results are shown in Table 6.4. Nb powder causes the main contamination by N and H, as demonstrated by H content clearly correlating with the increasing Nb concentration. The O concentration of the **-0.7O** samples is slightly lower than intended – the TiO_2 weight was calculated with the measured O concentration of Nb in mind, but some oxygen was adsorbed in the form of volatile compounds at the powder surface and desorbed during sintering in vacuum (a similar behavior was also observed for the sintered Ti5553 in section 5.2.1). As the solution treatment was performed in high vacuum furnace, the same chemical composition is assumed for the samples in the ST+WQ condition.

Table 6.4: The results of the CGHE analysis of the sintered samples, standard deviations of the last digit are given in the brackets.

Material	O (wt%)	N (wt%)	H (wt%)
Ti-**20Nb**-7Zr-**0.7O**	0.642(1)	0.029(1)	0.014(1)
Ti-**23Nb**-7Zr-**0.2O**	0.245(3)	0.030(1)	0.014(1)
Ti-**23Nb**-7Zr-**0.7O**	0.684(8)	0.031(2)	0.018(1)
Ti-**26Nb**-7Zr-**0.7O**	0.646(6)	0.032(2)	0.023(2)
Ti-**29Nb**-7Zr-**0.7O**	0.636(1)	0.034(1)	0.031(1)

The residual chemical heterogeneity was checked by EDS linescans in the AS samples, the results are plotted in Figure 6.12. The residual heterogeneity most pronounced in the local variations of concentration of Nb/Ti (as Nb is the slowest diffusing element) and decreases with the decreasing Nb content. It is relatively high for the Ti-**29Nb**-7Zr-**0.7O** alloy ($\sigma_{Nb} = 1.3$ wt%), but this is in the composition range where the phase composition of alloy is relatively stable and these variations should not play an important role. On the other hand, in the compositionally sensitive range around 23 wt% of Nb, σ_{Nb} is only around 0.5 wt% (see the green and red curves in Figure 6.12). The Zr concentration is relatively homogeneous in all samples. The additional solution treatment does not have any significant effect on the chemical heterogeneity at this scale, as the temperatures used for solution treatment are much lower than the sintering temperature.

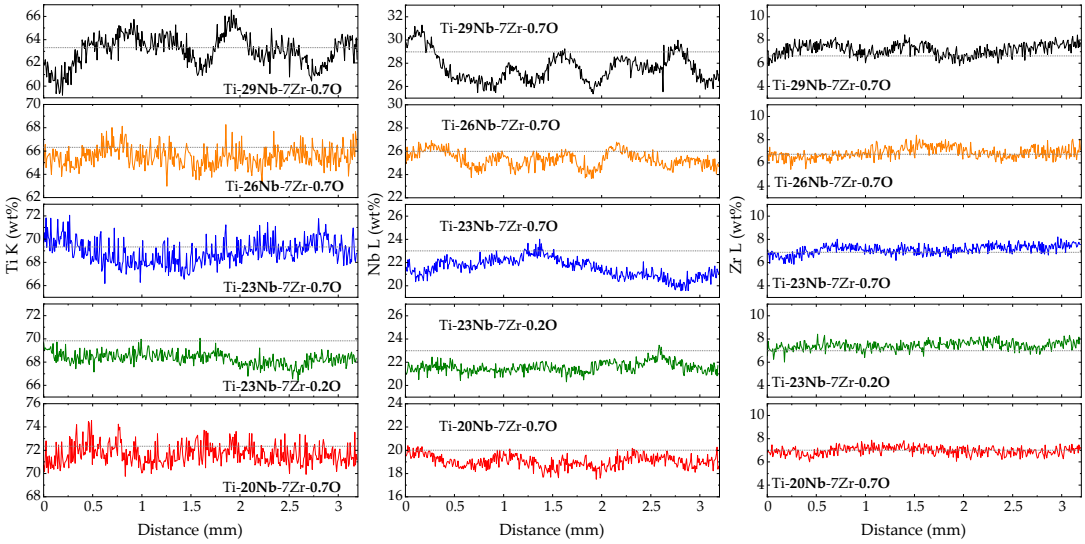

Figure 6.12: EDS line composition profiles showing residual inhomogeneities of the sintered alloys in as-sintered condition. It is assumed that the homogenization effect of the solution treatment at 1000 °C for 2 h is negligible when compared to 30 min spent at 1500 °C during sintering. The homogeneity is increasing with the decreasing overall Nb content. The dashed guides show the nominal composition of the alloy.

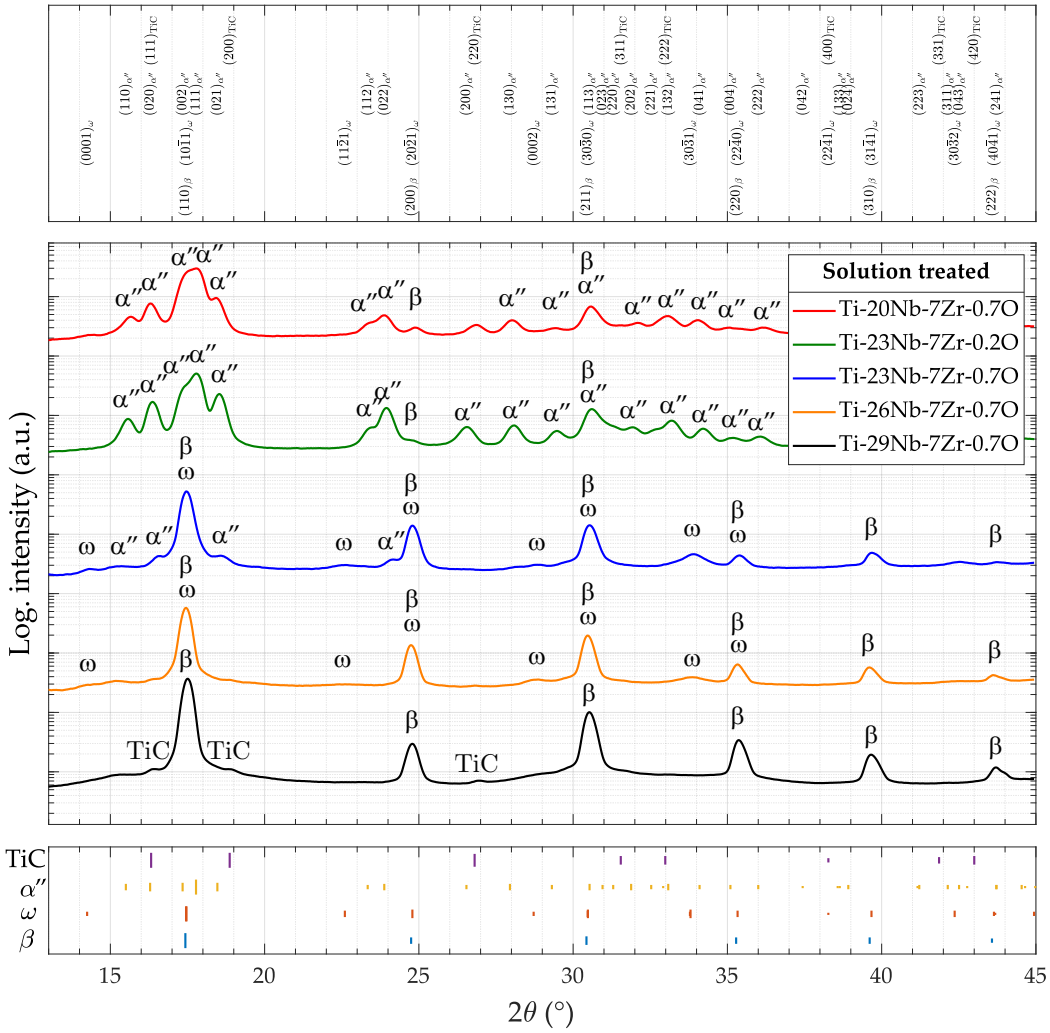

Figure 6.13: XRD diffractograms of the samples in the solution treated and water quenched (ST+WQ) condition. The tick marks in the lower part of the graph show calculated positions of the peaks, their lengths are proportional to the theoretical relative intensity of the peak. Not all peaks of all present phases are indexed on all lines and to increase readability.

Transmission XRD was performed on both ST+WQ and AS conditions and the resulting diffractograms are plotted in Figures 6.13 and 6.16, respectively. The experimental setup is described in detail in the section 3.4. Azimuthal integration was carried out on the raw 2D experimental data. All data are presented in a logarithmic intensity scale to show the weak peaks. The tick marks of the respective phases are plotted below the diffractogram, its length being proportional to the relative line intensity. The corresponding plane indices are plotted above the experimental data.

The XRD measurements were accompanied by SEM to show the microstructure and phase morphology, the BSE micrographs of the ST+WQ and AS conditions are shown in Figures 6.14 and 6.17, respectively. The black dots are remnants of the polishing suspension. The porosity is negligible in

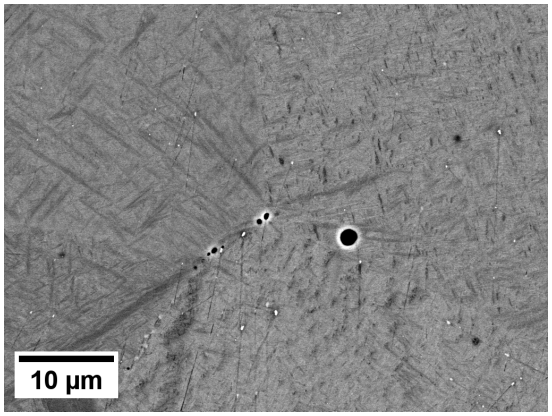

(a) Ti-**20Nb**-7Zr-**0.7O**

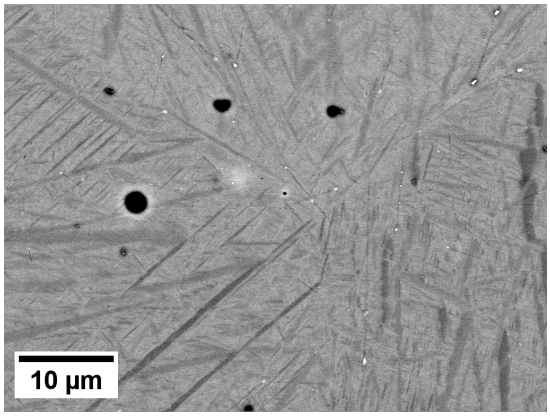

(b) Ti-**23Nb**-7Zr-**0.2O**

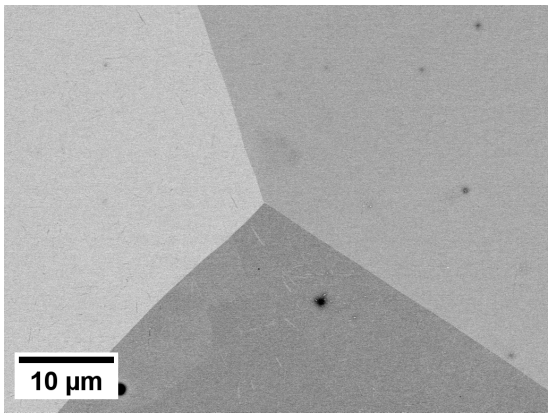

(c) Ti-**23Nb**-7Zr-**0.7O**

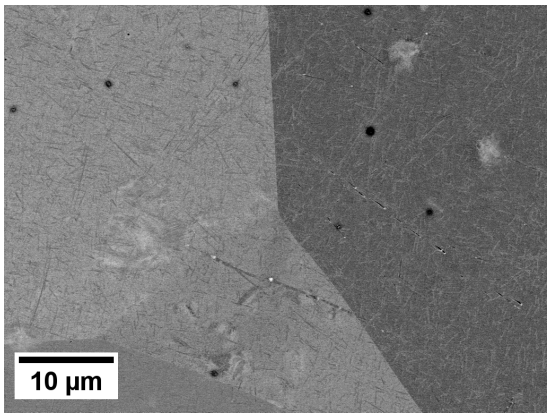

(d) Ti-**26Nb**-7Zr-**0.7O**

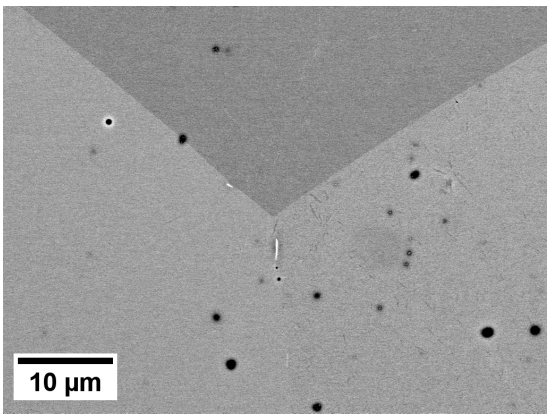

(e) Ti-**29Nb**-7Zr-**0.7O**

Figure 6.14: BSE SEM micrographs of the sintered alloys in the solution treated and water quenched (ST+WQ) condition.

all samples due to high sintering temperatures, resulting in reaching a full density [128].

We will start the description of the results with the ST+WQ samples (Figures 6.13 and 6.14), which are more straightforward to describe and interpret.

The ST+WQ Ti-**29Nb**-7Zr-**0.7O** sample (black line) shows only β peaks and a very small amount of TiC peaks. TiC is formed close to the sample boundary by reaction of Ti from the sample with C diffusing from the graphite foil. A

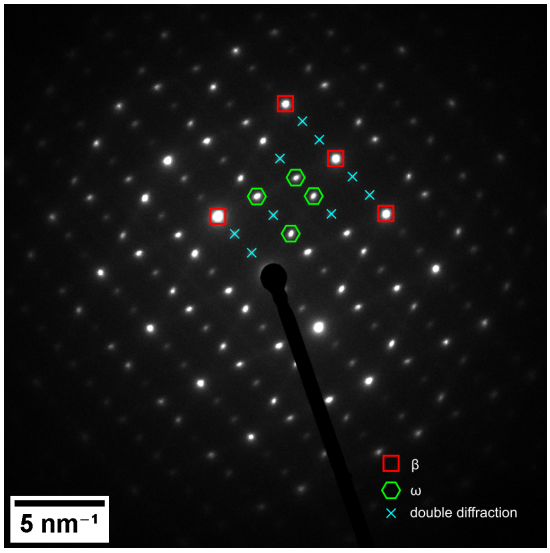

(a) SAED along $[311]_{\beta}$, Ti-**23Nb**-7Zr-**0.7O**

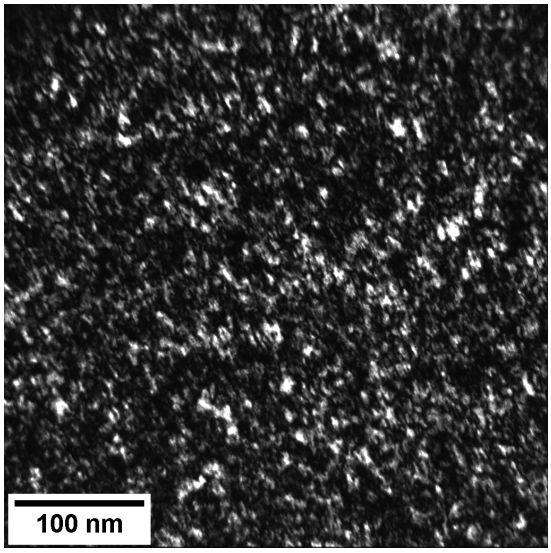

(b) DF micrograph of ω, Ti-**23Nb**-7Zr-**0.7O**

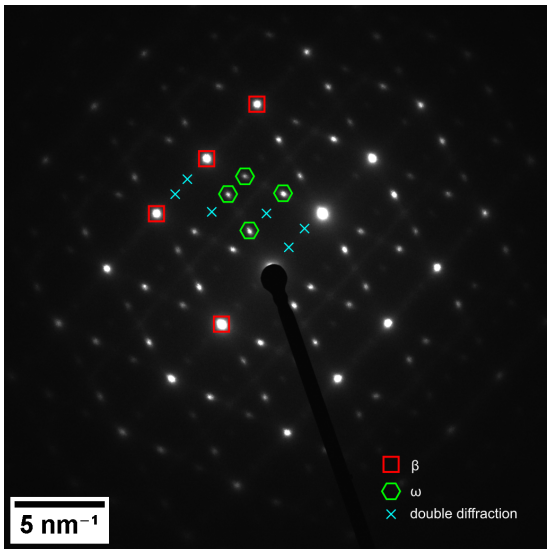

(c) SAED along $[311]_{\beta}$, Ti-**26Nb**-7Zr-**0.7O**

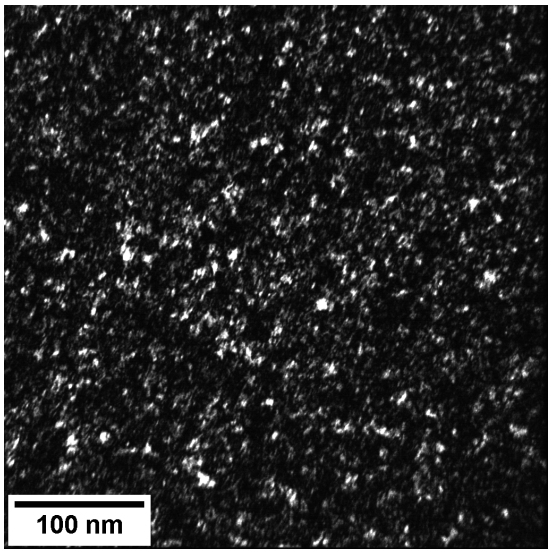

(d) DF micrograph of ω, Ti-**26Nb**-7Zr-**0.7O**

Figure 6.15: TEM micrographs and diffraction patterns confirming the presence of the ω phase in the water quenched Ti-**23Nb**-7Zr-**0.7O** and Ti-**26Nb**-7Zr-**0.7O** samples.

trace amount of the carbide is then captured by a broad X-ray beam. This is a contaminant phase with no effect on the rest of the phase transformations in the alloy. This sample exhibit a single-phase β microstructure in SEM micrograph (Figure 6.14e) as well.

In the ST+WQ Ti-**26Nb**-7Zr-**0.7O** sample (orange line), broad ω peaks are visible, most notably at 29 and 34°. Other peaks are hidden below much stronger β peaks. This appears as a single-phase microstructure in SEM micrograph (Figure 6.14d), since ω phase cannot be detected by SEM.

The two diffractograms of the ST+WQ Ti-**23Nb**-7Zr-**0.2O** (green) and Ti-**20Nb**-7Zr-**0.7O** (red) samples are similar, both consisting mostly of martensitic α'' peaks with some residual β phase present (the peak at 25°). The marten-

sitic microstructure is also clearly visible in the corresponding SEM images (Figures 6.14a and b).

The ST+WQ Ti-**23Nb**-7Zr-**0.7O** sample (blue line) contains both ω phase (peaks at 22.5, 29 and 34°) and a small fraction of α″ phase (peaks at 16.5 and 24°). The weak peaks of α″ martensite is present due to residual chemical heterogeneities – the Ti-**23Nb**-7Zr-**0.7O** is at the stability limit of the β phase and even small deviations in composition can lead to a locally different phase composition. The microstructure still appears to contain the β phase only (Figure 6.14c).

Because the diffraction peaks of the athermal ω_{ath} phase are broad and relatively weak and the phase is not visible in SEM, its presence was further confirmed by TEM observations, shown in Figure 6.15. The lamellae were cut using FIB from the ω-containing samples Ti-**26Nb**-7Zr-**0.7O** and Ti-**23Nb**-7Zr-**0.7O** and the corresponding SAED pattern and DF micrographs are shown in Figure 6.15. ω_{ath} peaks are clearly present in both samples (Figures 6.15a, c) and small ω particles ($< 10\,\text{nm}$) are visible in the DF micrographs (Figures 6.15b, d). The ω particles appear slightly smaller in the Ti-**26Nb**-7Zr-**0.7O** sample than in the Ti-**23Nb**-7Zr-**0.7O** sample (Figures 6.15d and c, respectively), which is consistent with the higher concentration of Nb in the Ti-**26Nb**-7Zr-**0.7O** sample stabilizing the β phase.

The AS samples were characterized in the same way as the ST+WQ samples – by XRD (Figure 6.16) and SEM imaging (Figure 6.17).

Both XRD (black line) and SEM (Figure 6.17e) have confirmed a single-phase microstructure of the AS Ti-**29Nb**-7Zr-**0.7O** sample.

The XRD of the AS Ti-**26Nb**-7Zr-**0.7O** sample (orange line) reveals a two-phase $\beta + \omega$ microstructure (the ω peaks at 14, 22.5 and 29°). The peaks are sharper than in the same sample in the ST+WQ condition, because larger, chemically stabilized isothermal ω_{iso} particles are formed. The micrograph (Figure 6.17d) shows isolated α_{GB} precipitates, but their phase fraction is small, so the α peaks are not detected by XRD.

The diffractogram of the AS Ti-**23Nb**-7Zr-**0.7O** sample (blue line) was most surprising, as it contains peaks of martensitic α″ phase, although the sample was not quenched, but cooled at a moderate rate $\sim 100\,\text{K/min}$. For example, the $(110)_{\alpha''}$ and $(020)_{\alpha''}$ peaks at 16°, or $(022)_{\alpha''}$ and $(200)_{\alpha''}$ peaks 24 and 26.5° clearly belong to α″ phase, as no other phase have peaks at these angles. There is also ω phase present (the peak at 23°) and a small amount of a stable α phase can be assumed by an asymmetrical peak broadening at 17.5 and 24°. The BSE micrograph (Figure 6.17c) shows α precipitates along GBs, which may be identified by a sharp contrast between α (dark) and surrounding β matrix (bright) caused mostly by a chemical segregation. A lamellar microstructure is observed inside grains – this may be both α and α″, since the phases are not distinguishable by SEM when there is only small difference in chemical composition between α and β.

According to XRD, the AS Ti-**20Nb**-7Zr-**0.7O** sample contains stable α and β phases only (red line). A fully lamellar martensite-like microstructure is observed in the micrograph (Figure 6.17a), suggesting that this α was formed by a decomposition of the martensitic phase.

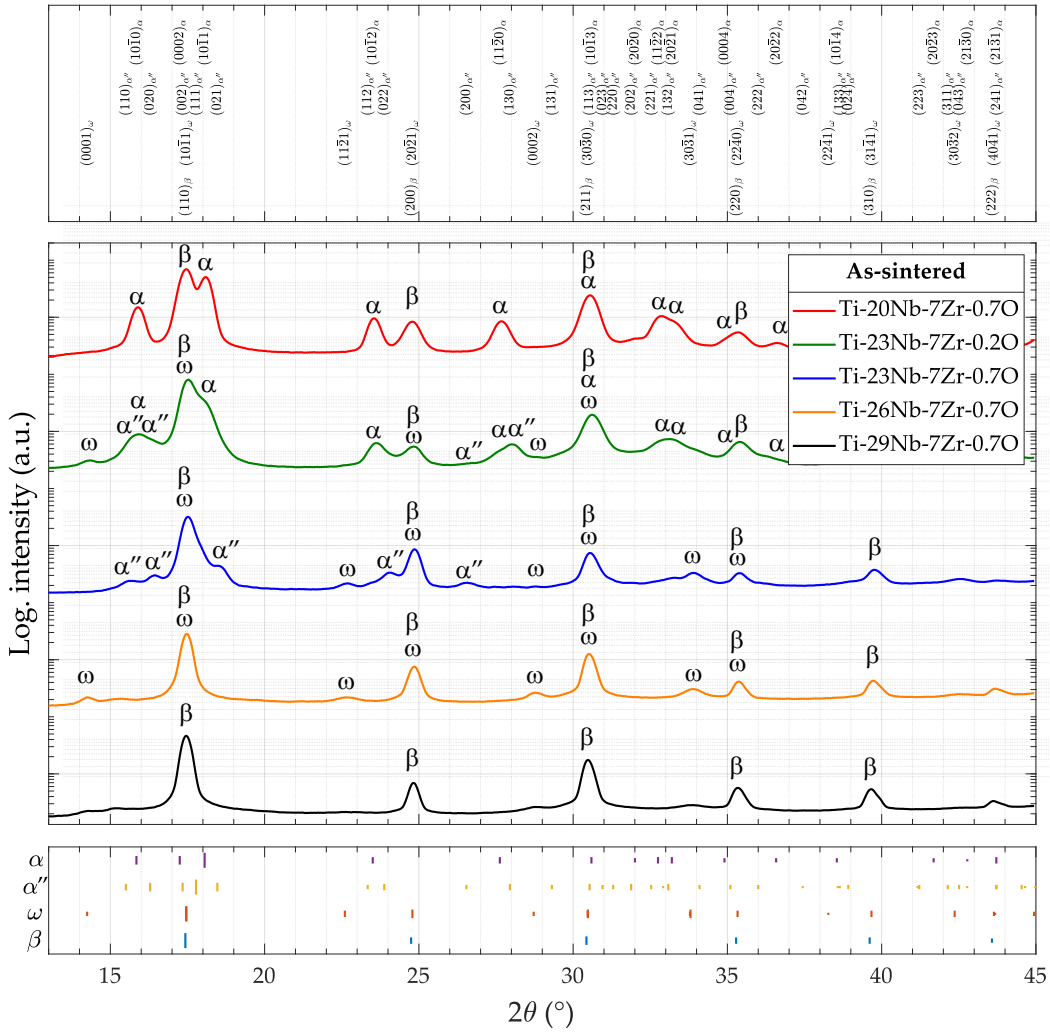

Figure 6.16: XRD diffractograms of the samples in the as-sintered (AS) condition. The tick marks in the lower part of the graph show calculated positions of the peaks, their lengths are proportional to the theoretical relative intensity of the peak. Not all peaks of all present phases are indexed on all lines to increase readability.

The XRD of the AS Ti-**23Nb**-7Zr-**0.2O** sample (green line) confirms the presence of ω phase (the peak at 14°) and a mixture of α and α″ phases, inferred from the broadening of peaks at 16 and 22.5°. The micrograph (Figure 6.17b) shows a lamellar microstructure, which may consist of both α and α″ phases.

Vickers microhardness (HV0.5) was measured on all AS and ST+WQ samples, 30 indents were made per specimen. The results are plotted in Figure 6.18 and the values are repeated in the summary in Table 6.5.

It can be immediately seen that the microhardness is strongly affected by a chemical composition. There are two major factors contributing to the alloy strength – the phase composition and the oxygen content, which affects the microhardness both directly (through solid solution strengthening) and indirectly (influencing phase composition).

The contribution of O can be best demonstrated at the Ti-**20Nb**-7Zr-**0.7O** and Ti-**23Nb**-7Zr-**0.2O** samples in the ST+WQ condition (Figure 6.18b) – the

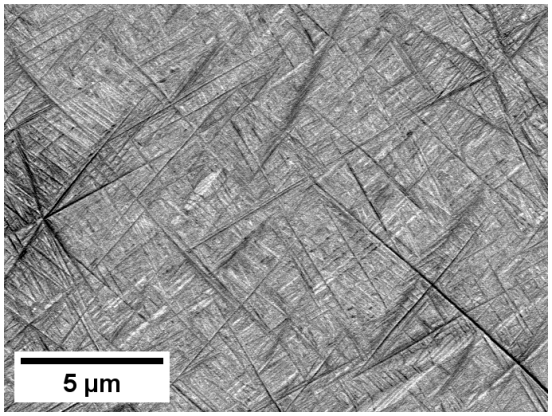

(a) Ti-**20Nb**-7Zr-**0.7O**

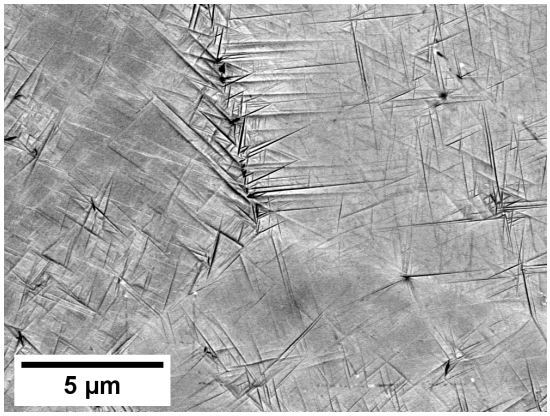

(b) Ti-**23Nb**-7Zr-**0.2O**

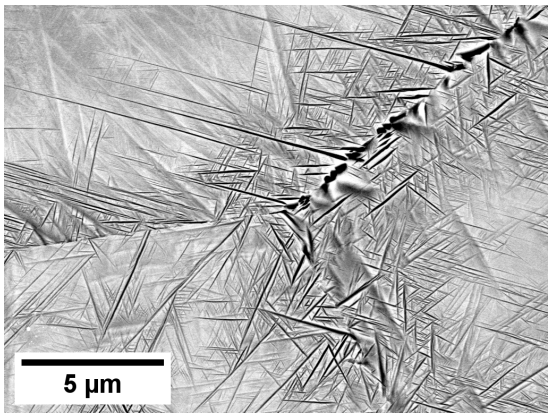

(c) Ti-**23Nb**-7Zr-**0.7O**

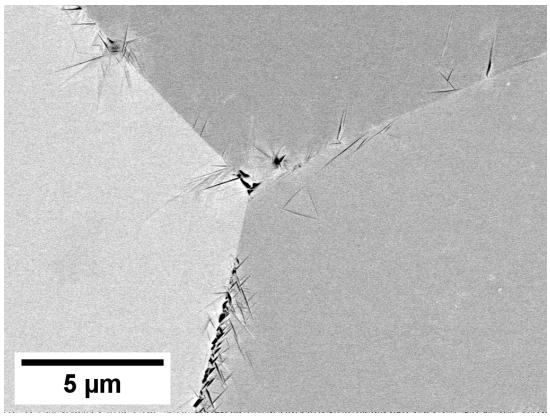

(d) Ti-**26Nb**-7Zr-**0.7O**

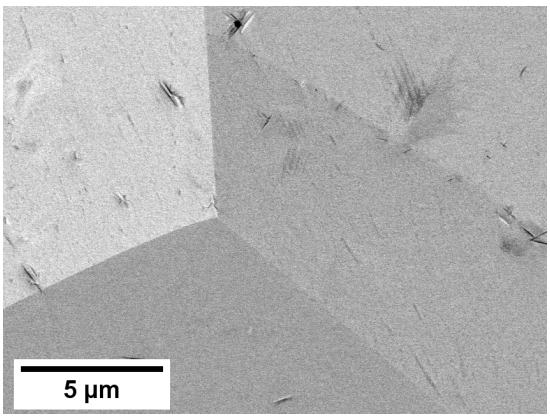

(e) Ti-**29Nb**-7Zr-**0.7O**

Figure 6.17: BSE SEM micrographs of the alloys in the as-sintered (AS) condition

difference in microhardness is 111 HV, while the microstructure and phase composition are the same, as shown earlier. Since the microstructure is fully martensitic in these two samples, the increased strength is attributed to oxygen blocking the twinning. The Ti-**23Nb**-7Zr-**0.2O** and Ti-**23Nb**-7Zr-**0.7O** (ST+WQ) couple demonstrates the indirect influence of oxygen, since the increased oxygen content completely changed the microstructure and ultimately the microhardness as well.

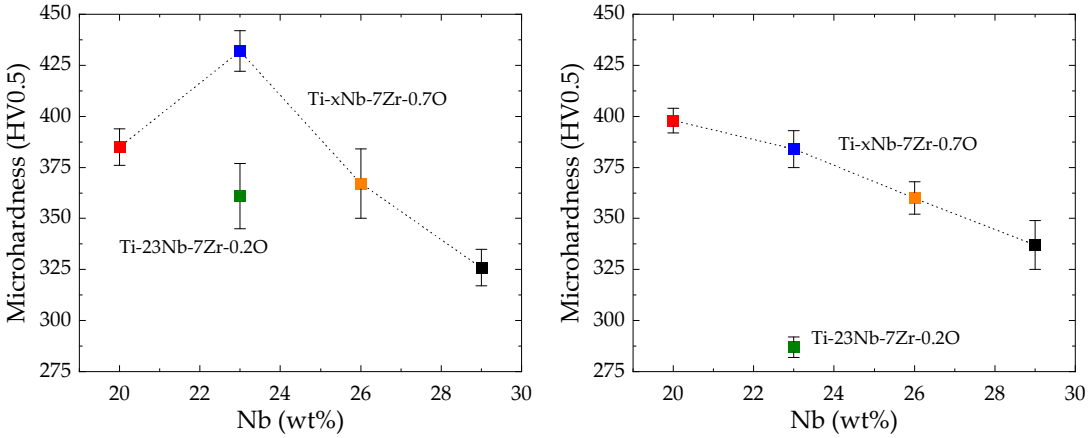

(a) As-sintered samples

(b) Solution-treated and water quenched samples

Figure 6.18: A graphical comparison of Vickers microhardness in the AS and ST+WQ condition. The values correspond to the values reported in Table 6.5. Samples with 0.7 wt% of oxygen are connected by dotted lines to emphasize general trends. The colors correspond to the colors in the diffractograms (Figures 6.13 and 6.16).

The microhardness of the ST+WQ Ti-**(23–29)Nb**-7Zr-**0.2O** samples monotonically increases with decreasing Nb content (Figure 6.18b), which can be attributed to the increasing content of ω_{ath} phase. The increase is even sharper in the AS samples Figure 6.18a) with larger isothermal ω_{iso} particles (cf. Figure 6.10). The highest microhardness (432 HV) was measured in the Ti-**23Nb**-7Zr-**0.7O** in AS condition, containing a combination of α, α'' and ω phases.

Finally, the elastic modulus was measured by resonant ultrasound spectroscopy (RUS). Contrary to microhardness, RUS is a bulk method, measuring an 'average' modulus within the sample. The results are provided in Table 6.5. To simplify the orientation in the data for the purpose of the following discussion, the modulus is shown along with the phase composition and microhardness for all alloys in both AS and ST+WQ condition.

The minimum elastic modulus of 64 GPa is achieved in the single-phase ST+WQ Ti-**29Nb**-7Zr-**0.7O** sample. The modulus of the AS Ti-**29Nb**-7Zr-**0.7O** is higher (75 GPa), which may be attributed to some ω_{iso} formed in residual chemical heterogeneities, although not detected by XRD. ω phase has indeed a strong influence on the elastic modulus – the highest modulus of 101 GPa is measured for the ST+WQ Ti-**23Nb**-7Zr-**0.7O** sample with the highest ω content due to a low amount of β-stabilizing Nb, as shown in Figure 6.15. After change in the phase composition to α'' in ST+WQ Ti-**20Nb**-7Zr-**0.7O** and Ti-**23Nb**-7Zr-**0.2O**, the modulus drops sharply to 81 and 77 GPa, respectively.

Among the AS samples, the modulus is highest in the Ti-**26Nb**-7Zr-**0.7O** sample, reaching 93 GPa. This sample contains largest fraction of ω_{iso} phase. The modulus decreases to $86 - 88$ GPa in the samples containing α/α'' as well.

Table 6.5: An overview table summarizing mechanical properties (Vickers microhardness ($HV0.5$) and Young's modulus E) and the phase composition.

	As-sintered			ST+WQ		
	E (GPa)	HV	Phases	E (GPa)	HV	Phases
Ti-**20Nb**-7Zr-**0.7O**	86	385(9)	α, β	81	398(6)	α''
Ti-**23Nb**-7Zr-**0.2O**	87	361(16)	$\alpha, \alpha'', \beta, \omega_{iso}$	77	287(5)	α''
Ti-**23Nb**-7Zr-**0.7O**	88	432(10)	$\alpha, \alpha'', \beta, \omega_{iso}$	101	384(9)	β, ω_{ath}
Ti-**26Nb**-7Zr-**0.7O**	93	367(17)	β, ω_{iso}	75	360(8)	β, ω_{ath}
Ti-**29Nb**-7Zr-**0.7O**	75	326(9)	β	64	337(12)	β

6.3 Discussion

An expected kinetics of the powder blend homogenization was observed. The alloy was not homogenized at 1300 and 1400 °C with Nb being the slowest diffusing element. This is consistent with the results in [26], showing that even 60 min at 1300 °C was not enough for a full homogenization. A reasonable chemical homogeneity was achieved at 1500 °C, similarly to [29].

As was shown in the previous section, the resulting microstructure of the Ti-xNb-7Zr-yO alloy strongly depends on the local chemical composition and the cooling regime. Because the samples were either water quenched or cooled at a moderate rate of $100 - 500$ K/min, the discussion must be based on non-equilibrium phase diagrams.

One such diagram is shown in Figure 6.19: it is a Ti-Nb binary section of the ternary Ti-Nb-Zr phase diagram, calculated by ThermoCalc using the TCTI3 database (solid lines). The stable $\alpha + \beta$ diagram is plotted in red, the metastable $\beta + \omega$ diagram in blue. The dashed lines denoted as $T_0^{\alpha/\beta}$ and $T_0^{\omega/\beta}$ represent the concentrations where the respective Gibbs energies are equal at the given temperatures. The blue and red T_0 curves were calculated for the system without oxygen, the orange curve was calculated for the oxygen-containing Ti-xNb-7Zr-0.8O system and is plotted for comparison. The ω phase was not calculated for the alloy with O, because there are no thermodynamic data available. The raw Gibbs energies of the individual phases from which these phase diagrams were constructed are shown in Appendix A.

The importance of the T_0 curve is that when we cool the β phase below it, the material can transform diffusionlessly to α. This can be achieved through a massive transformation, but in Ti alloys specifically, martensitic transformation occurs sooner at the supercooling of approximately 50 K below the T_0 [42]. The martensite start (M_S) curves for low and high oxygen content are plotted in purple. These curves were not calculated, but their position and shape were inferred from the experimental results and a general rule that M_S is always below the $T_0^{\alpha/\beta}$ curve.

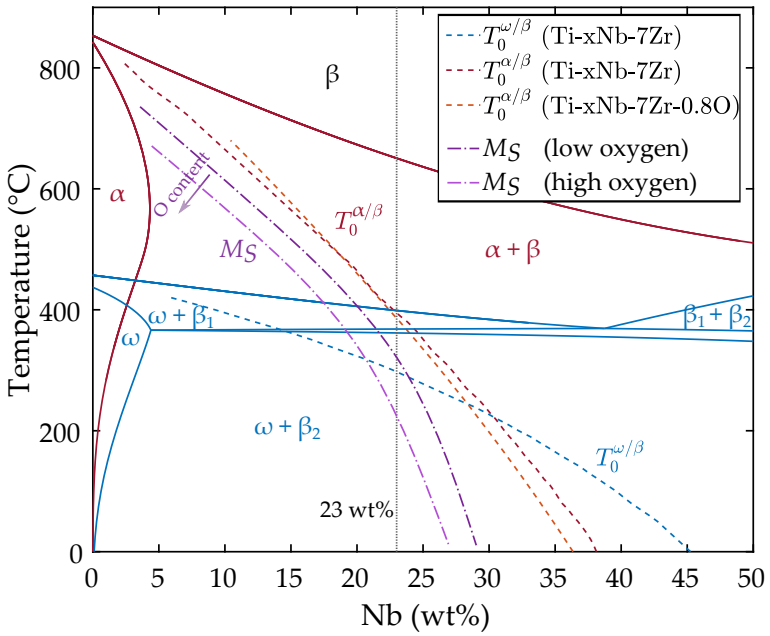

Figure 6.19: The metastable phase diagram of the Ti-xNb-7Zr(-0.8O) system. The phase diagrams and T_0 curves were calculated by ThermoCalc, The M_S lines (purple) were hand-drawn according to the experimental results. The experimentally determined concentration of 23 wt% of Nb is plotted for better orientation.

The phase composition of the quenched samples depends solely on the curve which is crossed first during cooling – either M_S, or $T_0^{\omega/\beta}$. If M_S is crossed first, we get martensitic α'' microstructure, while if $T_0^{\omega/\beta}$ is crossed first, we get two-phase $\beta + \omega$ microstructure. This depends on the alloy composition (Nb content) with respect to the position of the M_S and $T_0^{\omega/\beta}$ intersection. For the homogeneous alloy containing 0.7 wt% of O, this intersection must be placed between 20 and 23 wt% of Nb as the microstructure changes between those concentrations, for the alloy with 0.2 wt% of O, this happens above 23 wt% of Nb (cf. Figure 6.14). The M_S curves in Figure 6.19 are drawn accordingly. The oxygen can be therefore viewed as a β stabilizing element with respect to the $\beta \rightarrow \alpha''$ transformation, as reported earlier for various Ti alloys [67, 70, 74, 131–133].

The cooling rate of the as-sintered samples is in order of 100 K/min, so the diffusion plays an important role in the transformations kinetics. In the heterogeneous sample, the temperature is assumed to be homogeneous, while the β transus is dependent on the local Nb concentration. The precipitation of α can only start when sufficient undercooling below the local β transus is reached. Therefore, α can precipitate first at the places with low Nb concentration, especially at the preferential sites, such as GBs. This happens at a relatively high temperature where the growth kinetics is fast and large lamellae are formed. As the temperature decreases, the precipitation front moves towards higher Nb concentrations, but with the slower kinetics, significantly smaller α lamellae are formed (Figure 6.6).

The observation of the α'' phase in the as-sintered (i.e. not water quenched) Ti-**23Nb**-7Zr-**0.7O** sample, as detected by XRD (Figure 6.16), is actually not that

unique. When the alloy composition is close to the intersection of the Gibbs energies of α and β (i.e. close to the $T_0^{\alpha/\beta}$ curve), orthorhombic α″ phase (as a transitional phase between α and β) can form *isothermally*, by a mechanism described in [134]. According to Figure 6.19, the intersection temperature is 375 °C for the 23 wt% of Nb in the oxygen-containing alloy. This temperature meets the condition of being high enough to unfavor ω formation (i.e. being above the $T_0^{\omega/\beta}$) and sufficiently low to suppress any further chemical partitioning (which would normally lead to the decomposition of α''_{iso} into stable α and β), so the α″ phase is retained when cooled to the RT.

Only ω phase is present in the heterogeneous sample in regions with the Nb concentration above 22 wt%. This agrees well with the possible location of the M_S and $T_0^{\omega/\beta}$ intersection in Figure 6.19, corresponding to the temperature around 300 °C. Below this concentration, the α/α'' phase is formed either clasically, or via a diffusionless $\beta \rightarrow \alpha''$ transformation. Above 22 wt%, ω is formed first and martensitic transformation is no longer possible, but the diffusion of Nb is sufficient for a chemical stabilization of extremely small ω_{iso} particles.

The elastic modulus is mostly influenced by the phase composition. Pure β phase in the ST+WQ Ti-**29Nb**-7Zr-**0.7O** sample has the lowest modulus, which sharply increases with the presence of the ω phase. The ω_{iso} phase has more significant effect than ω_{ath} (93 vs. 75 GPa in AS and ST+WQ Ti-**26Nb**-7Zr-**0.7O**, respectively). This can be attributed to higher ω stability due to chemical segregation.

6.4 Summary

We have shown in this chapter that blended elemental powder metallurgy is a viable approach for sintering of complex titanium alloy, provided that sufficiently high temperature is used to ensure the alloy homogenization.

Furthermore, it was demonstrated that the use of heterogeneous samples can be very useful in determining concentration limits for various phase transformations, entirely in the spirit of high-throughput methods. The upper concentration limit of Nb for α/α'' formation in the Ti-*x*Nb-7Zr-0.8O alloy was measured to be 22 wt%; at higher Nb content, ω phase forms.

The role of oxygen in suppressing the $\beta \rightarrow \alpha''$ martensitic transformation was confirmed by direct comparison at otherwise same conditions. For achieving low elastic modulus, a single-phase β microstructure must be preserved at the RT.

The results from this chapter were published as two journal papers:

Kozlík, J., Preisler, D., Stráský, J., Veselý, J., Veverková, A., Chráska, T., *et al.* Phase transformations in a heterogeneous Ti-xNb-7Zr-0.8O alloy prepared by a field-assisted sintering technique. *Materials & Design* **198**, 109308. ISSN: 0264-1275. DOI: 10.1016/j.matdes.2020.109308 (2021).

Kozlík, J., Preisler, D., Stráský, J., Košutová, T., Corrêa, C. A., Veselý, J., *et al.* Manufacturing of biomedical Ti alloys with controlled oxygen content

by blended elemental powder metallurgy. *Journal of Alloys and Compounds* **905**, 164259. ISSN: 0925-8388. DOI: 10.1016/j.jallcom.2022.164259 (2022).

We have further exploited the method of preparing heterogeneous samples using FAST in [135]. Heterogeneous samples with Nb content varying between layers (2 mm in height) were prepared. This allowed elastic modulus mapping by scanning acoustic microscopy in collaboration with the Institute of Thermomechanics of the Czech Academy of Sciences and investigations of deformation mechanisms (and the presence of a twinning/transformation induced plasticity (TWIP/TRIP) effect) using DIC during in-situ compression testing.

Another extension of results presented in this chapter is a development of a method for high-throughput characterization of refractory complex concentrated alloys (RCCA). The preliminary results of this research will be the topic of the last chapter.

7 Outlook: High-Throughput Characterization of RCCA

In the previous chapter, blended elemental powder metallurgy was used for phase analysis in chemically heterogeneous samples. While not being crucial in relatively simple and well explored Ti alloys, its benefits can be best exploited for investigations of complex concentrated alloys (CCAs).

In this chapter, we would like to present an approach to the experimental exploration of the vast concentration space of refractory complex concentrated alloys (RCCAs). We have designed the method as a part of an ongoing research project. The chapter does not aim at providing complete data about the studied alloying system, but rather at showing the methodology and some preliminary tentative results.

7.1 Material Preparation

A quinary RCCA system $Al_{20}Ti_{20}Ta_xNb_yZr_z$ (at.%) was investigated in this chapter. A two-dimensional ternary section of the four-dimensional phase diagram (Al and Ti concentrations were fixed) was physically sampled in a hexagonal grid as illustrated in Figure 7.1. The corners of the phase diagrams were not investigated, since we focus on RCCAs, i.e. the central region of the phase diagrams.

The properties of the powders used for sintering are summarized in Table 7.1. All powders had spherical morphology, since those usually have also low contamination thanks to small specific surface. Similar particle size was chosen for all powders to facilitate the mutual mixing.

For separation of the powder blends of the different compositions during filling of the die, a special spacer was designed, drawn in Figure 7.2a, and printed using a Prusa i3 MK3S+ 3D printer (PCTG filament, layer height 0.1 mm). To reduce the surface roughness after printing, parts were smoothed by chloroform.

The spacer was then inserted into a sintering die as shown in Figure 7.2b and filled with the respective powder blends. Due to the lack of data, the amount of each blend is calculated assuming the same phase in each compartment and a random occupation of the atomic sites for the given nominal composition. Then, the 'pusher' was inserted into the spacer to hold the powders in place, and the spacer was carefully pulled out. The filled die is shown in Figure 7.2c. Tungsten foils were used to prevent carbon contamination during sintering.

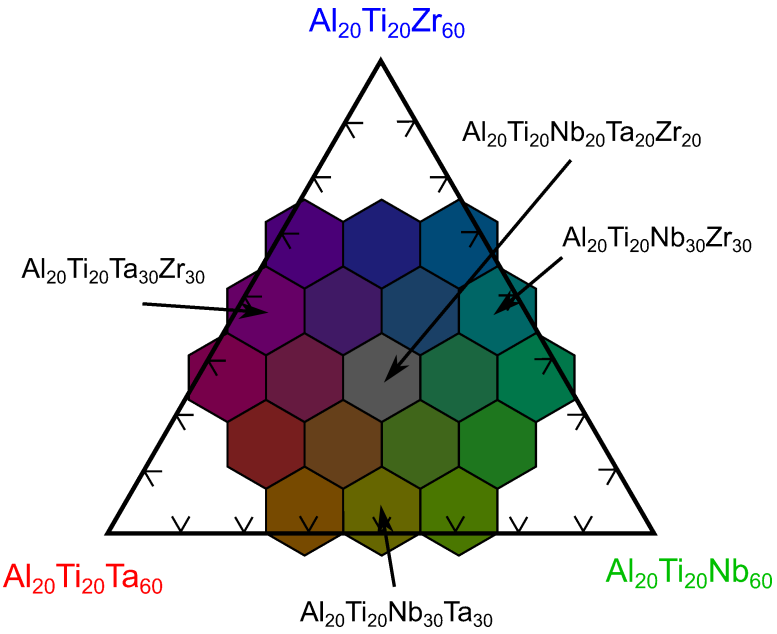

Figure 7.1: A schematics of the mapping strategy – a two-dimensional ternary section of the full four-dimensional compositional space overlaid with the hexagonal compartments, each with a different nominal alloy composition. The concentration step between the compartments is 10 at.%.

The sintering was carried out according to the sintering program plotted in Figure 7.3, which was based on the programs used for sintering of Ti5553 and Ti-Nb-Zr-O alloys. At the beginning, the sample was heated to 600 °C at 400 K/min, followed by a 20 min dwell. This intermediate stage was used for

Table 7.1: The powders used for sintering. The particle size and morphology are taken from the supplier's datasheet, as well as the Ti chemical composition. Other powders were independently measured by CGHE (carrier gas hot extraction) method. The numbers in brackets are standard deviations of three measured specimens.

Powder	Manufacturer	Particle size & morphology	O (wt%)	N (wt%)	H (wt%)
Al	Eckart TLS	spherical 20 – 53 µm	0.083(4)	0.002(1)	—
Ti Grade 1	Eckart TLS	spherical 20 – 53 µm	0.091(4)	0.010(1)	0.002
Ta	CAMEX	spherical 15 – 45 µm	0.076(8)	0.007(2)	—
Nb	Stanford Advanced Materials	spherical 15 – 45 µm	0.221(5)	0.051(4)	—
Zr (Grade 702)	TLS Technik	spherical 20 – 80 µm	0.175(1)	0.009(1)	0.001(1)

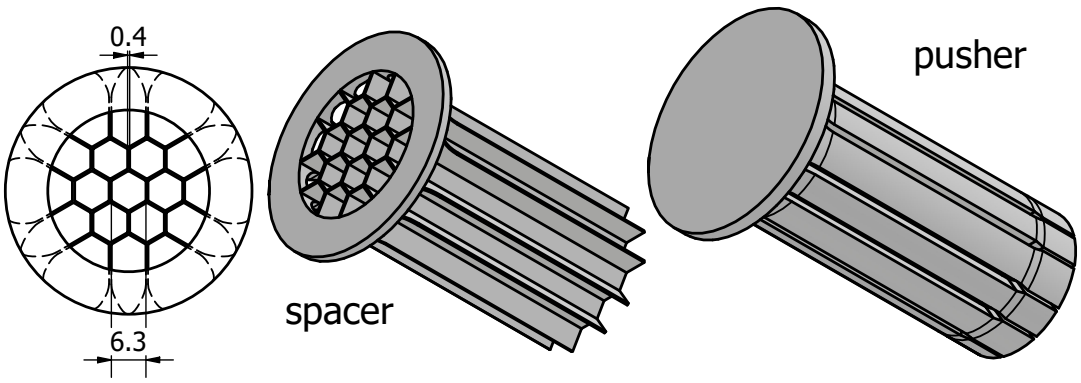

(a) A CAD drawing of the tools. Dimensions are in millimeters.

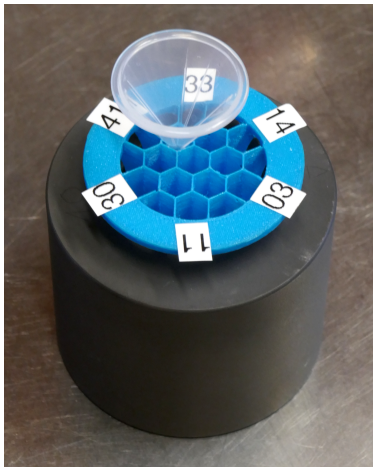

(b) The die filling in progress

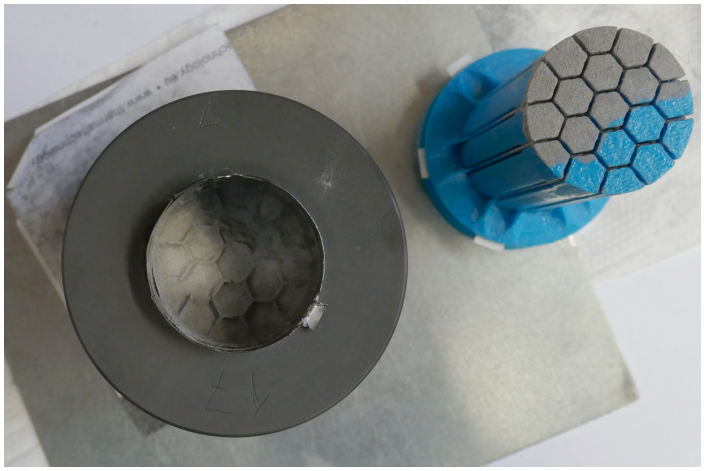

(c) The filled die after the spacer and pusher are removed

Figure 7.2: Using the honeycomb spacers for the FAST die filling

alloying of Al with other elements to prevent its sudden melting. Then, the sample was heated at 100 K/min to 1250 °C, where the heating rate was decreased to 50 K/min to prevent temperature overshoot, and heated to the final sintering temperature of 1300 °C. The isothermal sintering was performed for 30 min and the sample was subsequently cooled to the RT.

The piston position data (the green curve) show a movement of the piston during the isothermal stage (at ca 50 min) when the shrinkage rate suddenly increases. This may be caused by the dissolution and homogenization process after the consolidation is finished, or by deformation of the sample when the homogenization behavior is different in different regions of the sample.

The sintering was performed at a relatively low temperature of 1300 °C, even though we needed to homogenize the slow-diffusing Ta. This is due to a possible formation of Al-Zr intermetallics, which have relatively low melting points of 1462 °C (Al_3Zr_5). As we have earlier learned the hard way, the combination of a temperature overshoot and the piston pressure can lead to a catastrophic failure during sintering when the intermetallic compound melts. Therefore, we have used the FAST for consolidation only and the homogenization was carried out in a tube furnace (Nabertherm) with a more precise temperature control and a water quenching capability. For homogenization, the sample was wrapped in the Zr foil to suppress oxidation, homogenized at

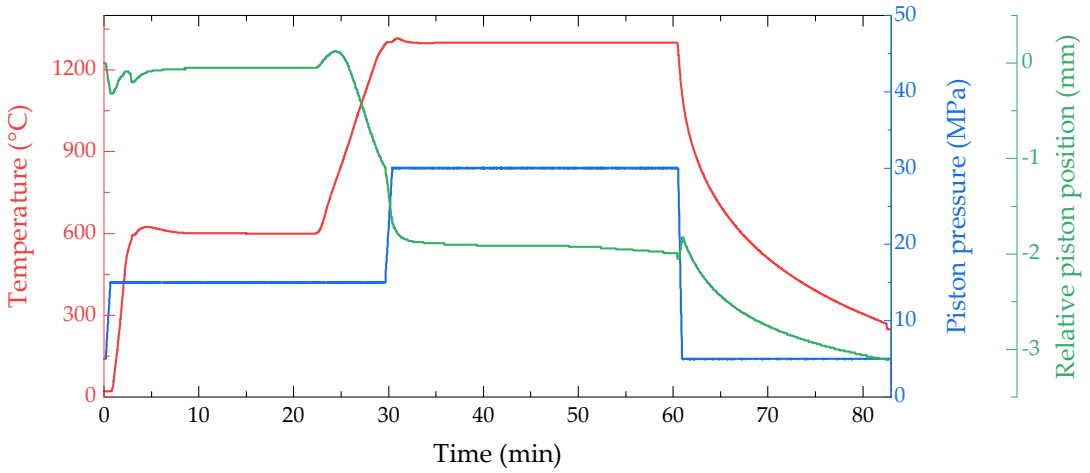

Figure 7.3: The process parameters during the sintering of the heterogeneous RCCA sample

1400 °C for 168 h in an Ar atmosphere (99.9999 % purity) and water quenched. The quenching is necessary to prevent formation of other phases during cooling.

The samples were sliced using precision metallographic saw and ground by SiC papers up to #2000 grit. The final polishing was performed using Vibromet vibratory polisher in three steps – 8 h in 0.3 µm Al_2O_3 suspension, 8 h in 0.05 µm Al_2O_3 suspension and 4 h in 0.05 µm SiO_2 colloidal suspension.

7.2 Results

The sintering and the heat treatment were successfully carried out. The BSE micrograph of the sintered sample section is shown in Figure 7.4. The compartment structure was preserved during the die filling and sintering and is clearly visible. The compartments are slightly deformed when compared to the drawing in Figure 7.2, with the Zr rich compartments (the upper part of the micrograph) bigger than the Zr lean compartments. This may be caused either by an uneven compartment filling and subsequent displacement under mechanical load, or by different densification kinetics and CTE, causing different balance of shrinkage and thermal expansion in each compartment, resulting in internal stresses and displacements.

There is a large number of cracks, especially in the Zr rich part of the sample. This should not be a surprise, as the sample is strongly heterogeneous (in CTE, besides other things), causing large internal stresses during water quenching from 1400 °C. The cracks mostly follow the GBs decorated with brittle Al-Zr intermetallics, which are more common in the Zr rich area.

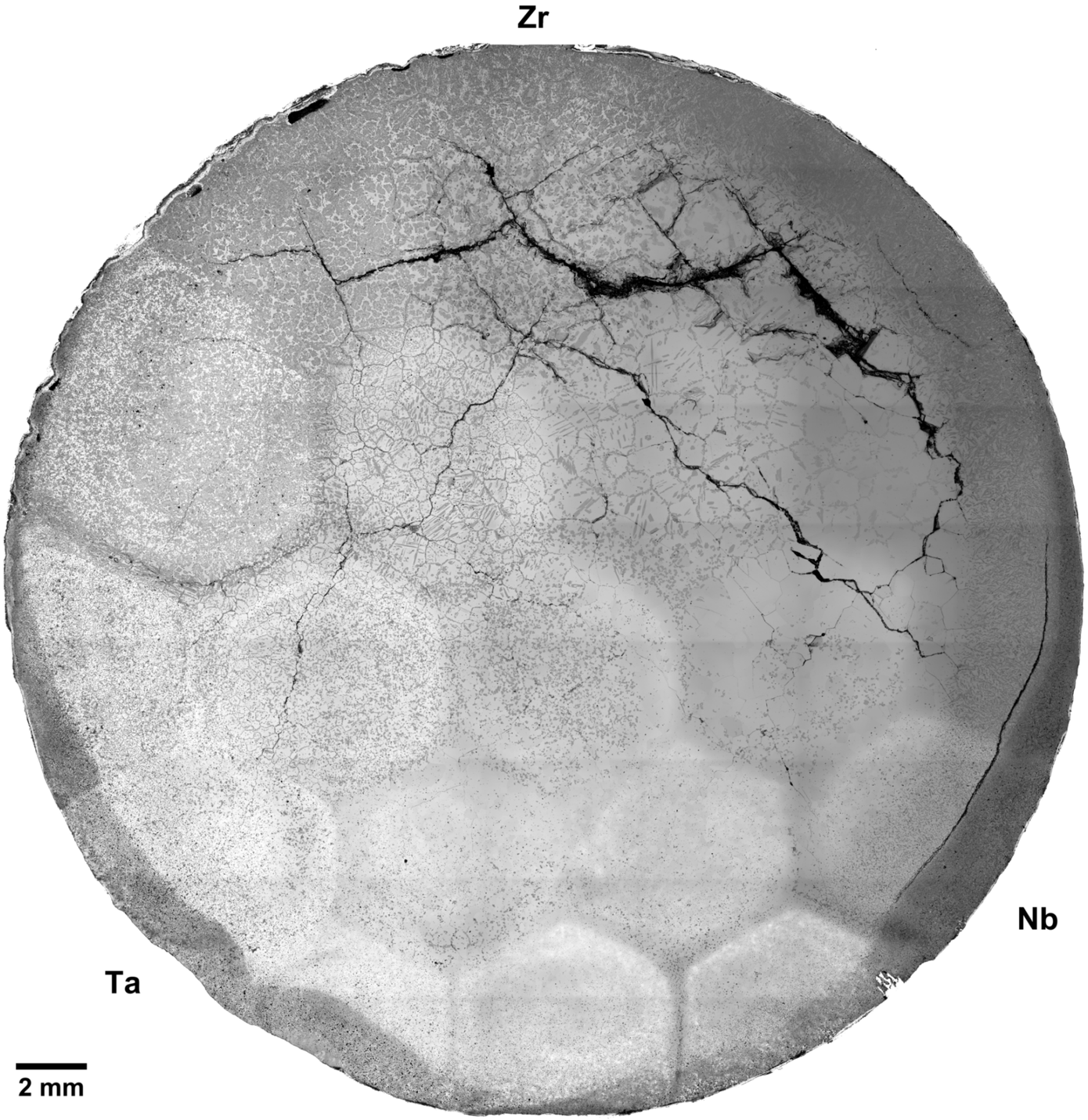

Figure 7.4: A stitched BSE micrograph of the sintered sample cross-section with the compartment structure clearly visible. Cracks in the upper part are a result of heterogeneous coefficient of thermal expansion and rapid cooling during quenching. Horizontal shading is caused by an insufficient flat-field correction of the image tiles.

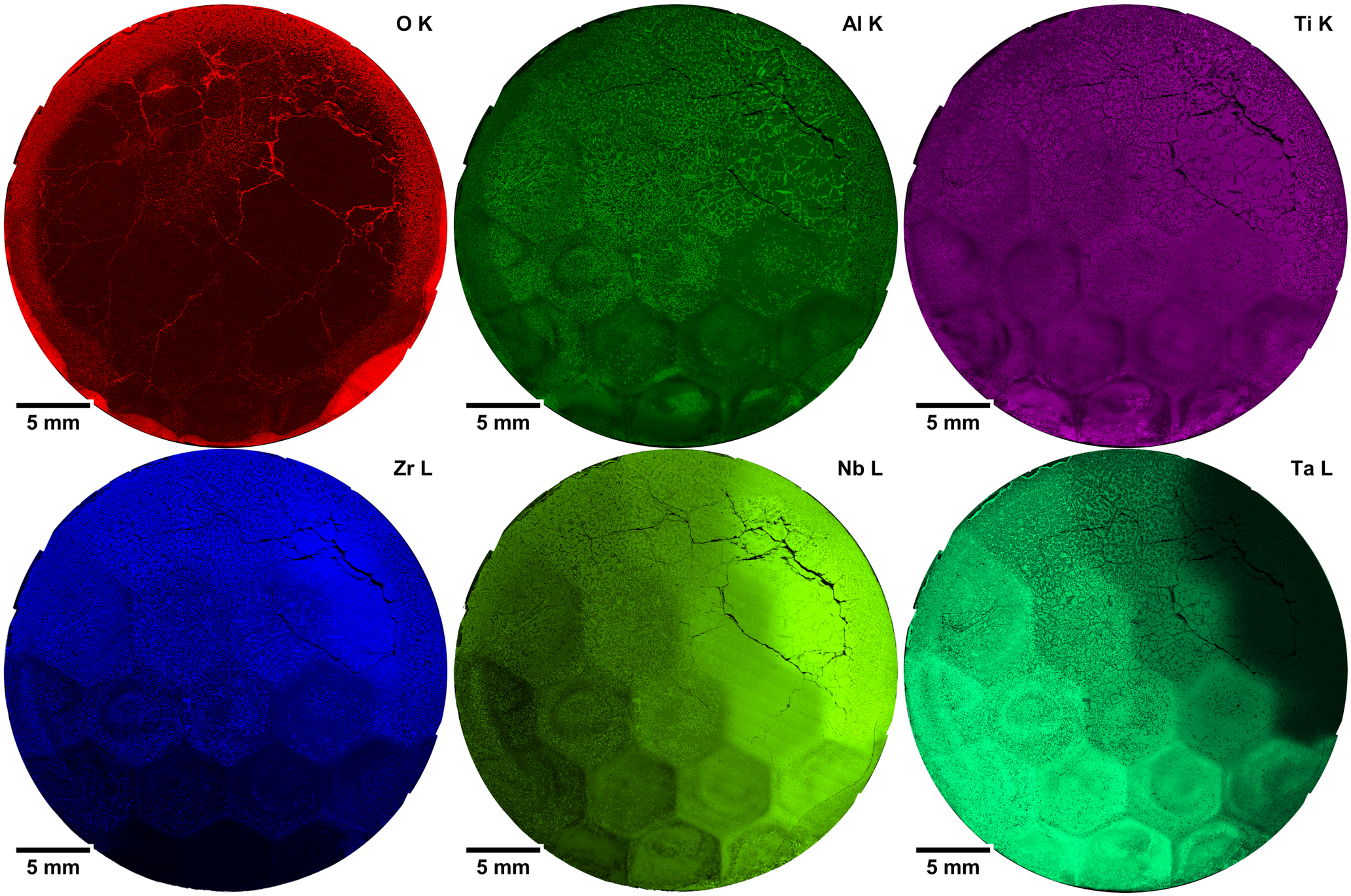

Figure 7.5: Low magnification EDS maps of the whole sample area. The sample and orientation are the same as in Figure 7.4, although a different section of the sample is shown. Courtesy of Radek Mušálek, IPP CAS.

An EDS mapping was performed across the sample (a different section, though), the raw count maps are shown in Figure 7.5 for all alloying elements and oxygen. Apart from the oxygen signal from the cracks, coming from the remnants of the polishing suspension, there is an oxygen rich layer near the surface of the sample, few mm into depth. This corresponds to the darker band around the edge in Figure 7.4, containing oxides (which will be shown later in higher magnification). The oxygen content in the surface samples measured by CGHE reached 5 wt% (!), while in the center of the specimen, the concentration of O was 'only' 0.75 ± 0.09 wt%. This suggests significant oxidation during the heat treatment.

The other elemental maps have shown that there is a large amount of Al- and Zr- rich phases present (probably the Al-Zr intermetallics). The Nb L sig-

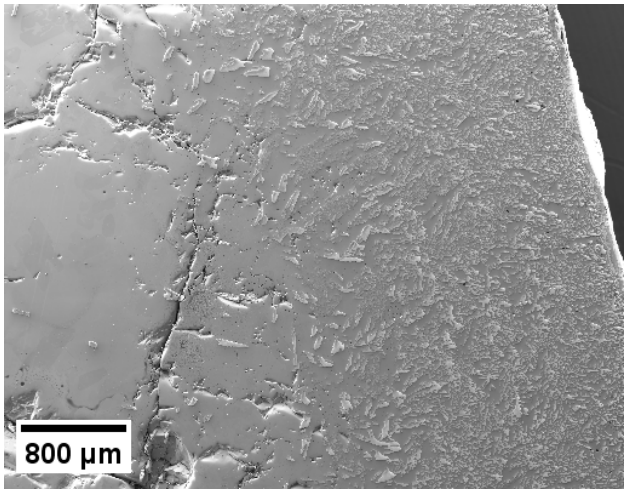

(a) SEM BSE micrograph

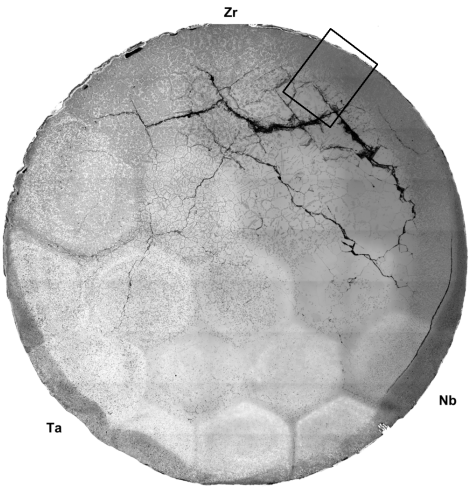

(b) Position of the map at the sample

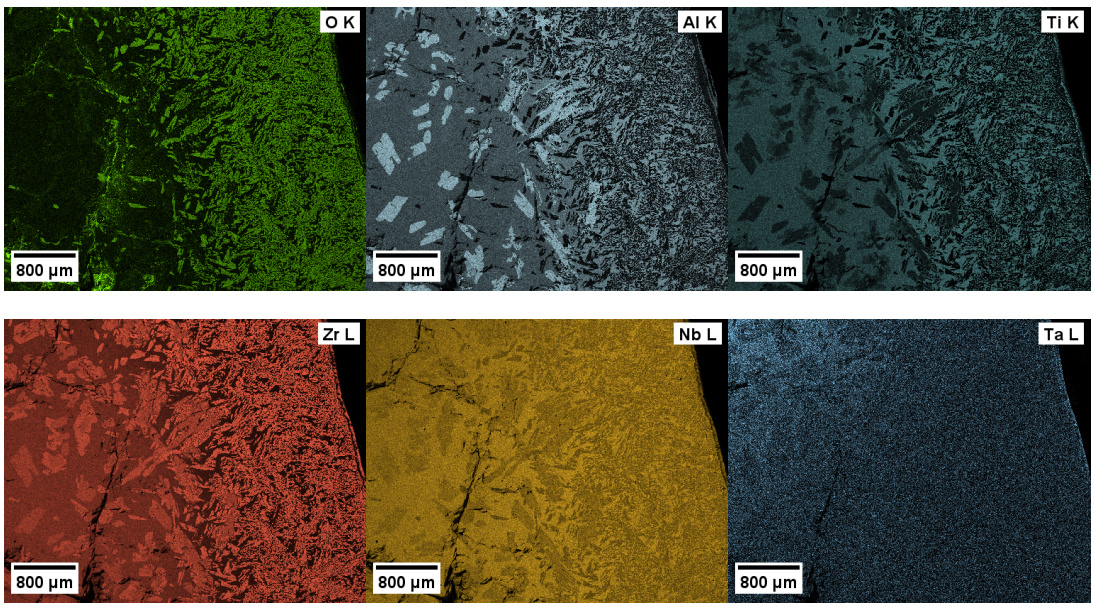

(c) EDS elemental maps

Figure 7.6: The SEM and EDS analysis of the oxide layer in the compartment corresponding to the $Al_{20}Ti_{20}Nb_{20}Zr_{40}$ alloy (nominally).

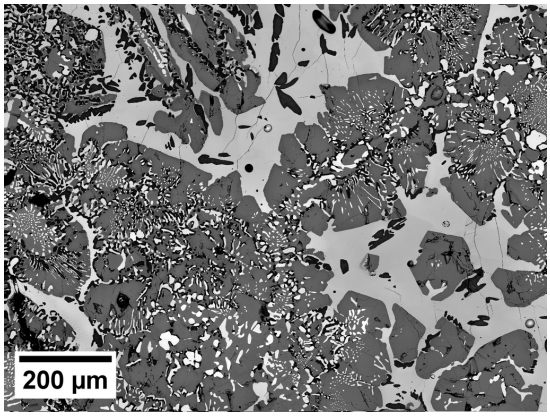

(a) SEM BSE micrograph

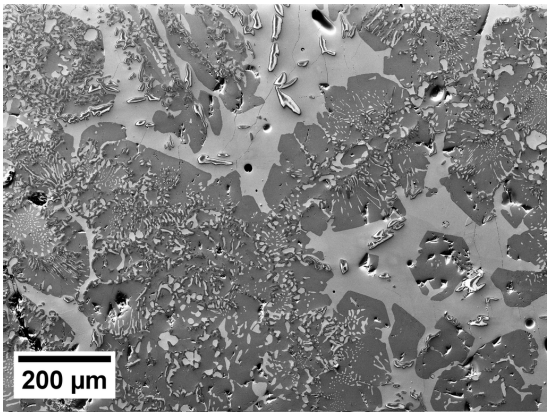

(b) SEM SE micrograph

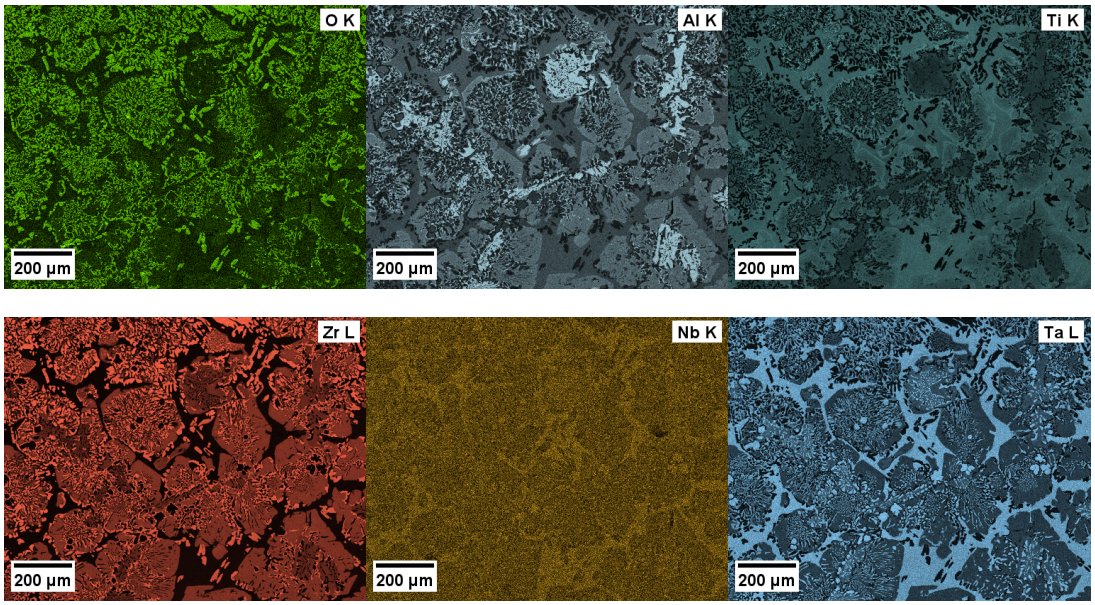

(c) EDS elemental maps

Figure 7.7: The SEM and EDS analysis of the $Al_{20}Ti_{20}Ta_{20}Zr_{40}$ alloy: multiple phases and traces of eutectic transformation are present.

nal is strongly correlated with the Zr L signal due to peak overlap. There are also some heterogeneities visible at the millimeter scale, best visible in the compartments in the lower part of the sample. These are much larger than the average particle size and can be only attributed to poor mixing of the powder. It should be noted that since we are not interested in macroscopic mechanical properties, it is sufficient that the average composition is homogeneous in the region of interest for detailed EDS mapping.

The oxide layer is shown in greater detail in Figure 7.6. The correlation of Zr and O signals suggests that the oxides are mostly ZrO_2, the Nb is correlated with Zr due to the peak overlap.

Typical micrographs of the compartment microstructure are shown in Figure 7.7 to 7.9, accompanied by the EDS maps. Both micrograph collection and EDS acquisition were fully automated (in the spirit of high-throughput method). The drawback is that it is not possible to automatically tune brightness and contrast in EDS acquisition software for each map, which renders

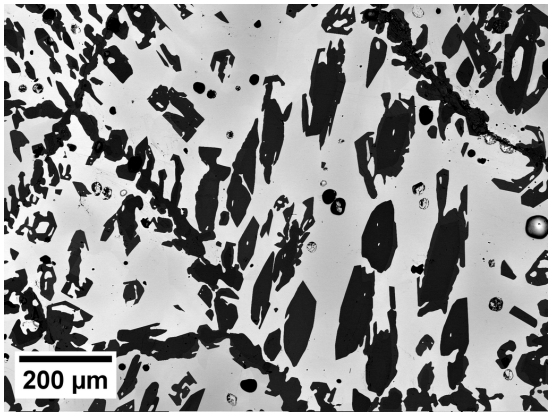

(a) SEM BSE micrograph

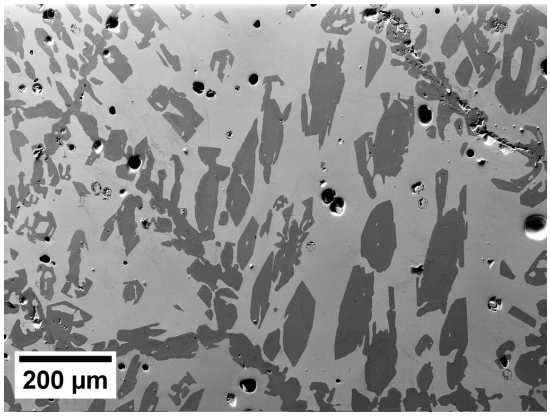

(b) SEM SE micrograph

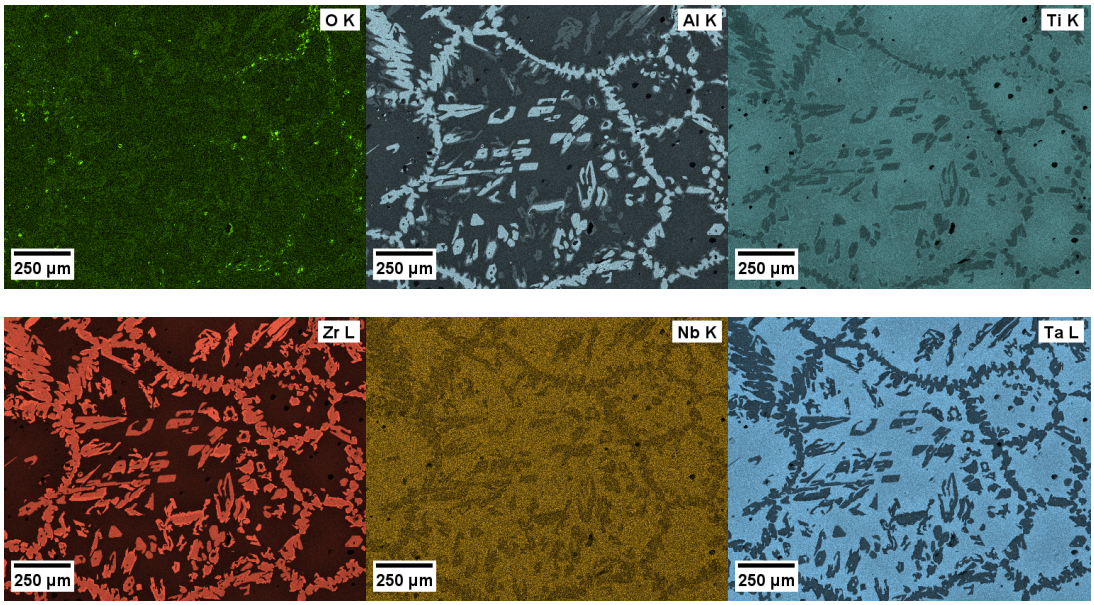

(c) EDS elemental maps

Figure 7.8: The SEM and EDS analysis of the $Al_{20}Ti_{20}Ta_{20}Nb_{10}Zr_{30}$ alloy: two different AlZr intermetallics with different compositions.

the SEM micrographs acquired during EDS mapping unusable for such compositionally heterogenous sample. Therefore, an SEM image from a different position within the same compartment had to be used.

The $Al_{20}Ti_{20}Ta_{20}Zr_{40}$ alloy, shown in the Figure 7.7, contains at least 4 compositionally different phases: the Ta-, Nb- and Ti-rich matrix and various Al-, and Zr-based intermetallic phases with additions of other elements. Traces of solidification/eutectic microstructure are visible within the Al- and Zr-rich regions, suggesting that partial melting may have occurred during the heat treatment.

Two compositionally different intermetallic compounds were found in the $Al_{20}Ti_{20}Ta_{20}Nb_{10}Zr_{30}$ alloy (Figure 7.8). The first one, found at the grain boundaries of the matrix, consists mostly of Al and Zr, while the second one is significantly enriched with Ti. Ta and Nb are mostly found in the matrix.

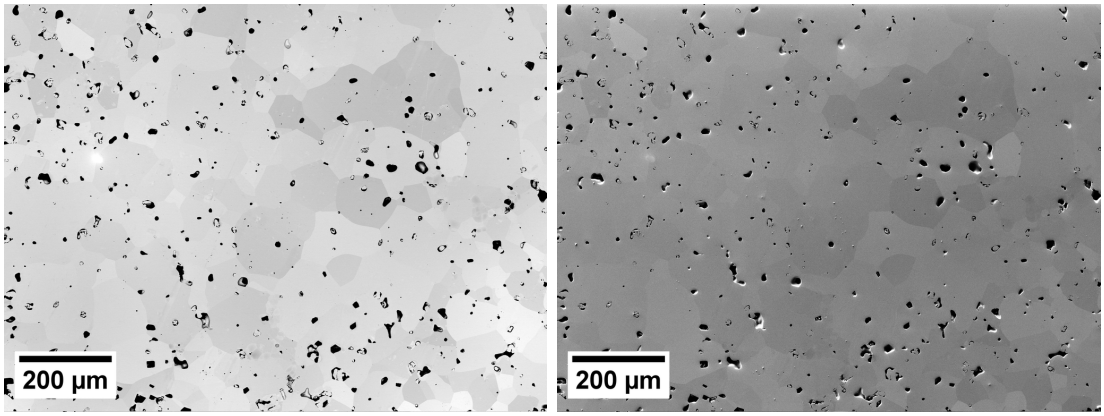

(a) SEM BSE micrograph (b) SEM SE micrograph

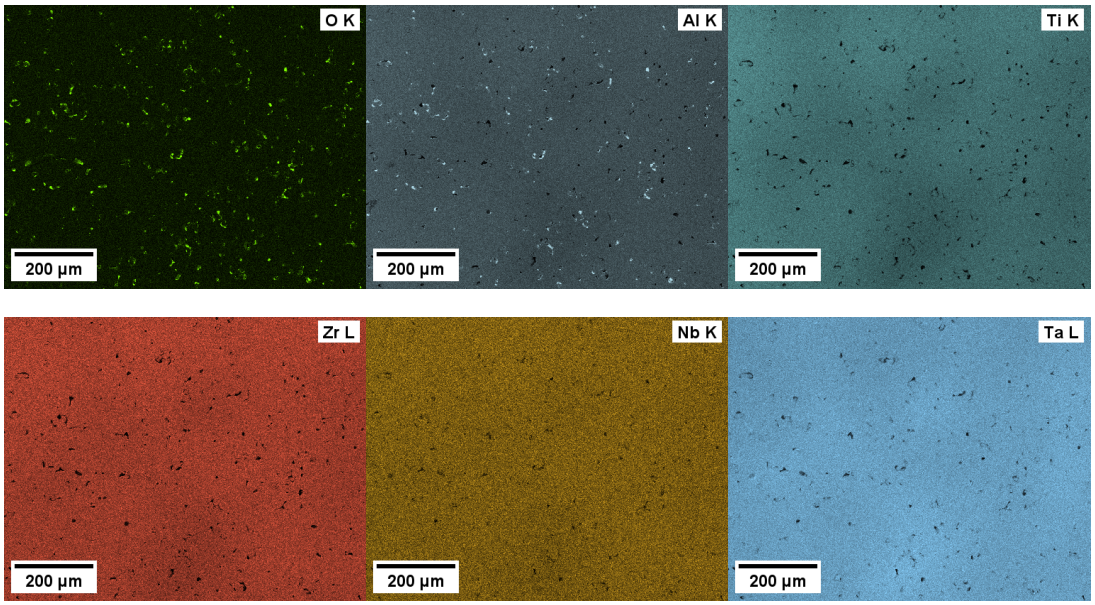

(c) EDS elemental maps

Figure 7.9: The SEM and EDS analysis of the $Al_{20}Ti_{20}Ta_{30}Nb_{30}$ alloy: the single-phase microstructure.

Finally, a homogeneous, single-phase microstructure was observed in the $Al_{20}Ti_{20}Ta_{30}Nb_{30}$ alloy (Figure 7.9), with only small fraction of Al_2O_3. A significant porosity (2.5 %) was found as a result of alloying.

7.3 Outlook

We have shown that it is possible to exploit the capabilities of FAST for high-throughput manufacturing and analysis of RCCAs. However, there are several issues which need to be addressed for the future, concerning sample manufacturing, data acquisition and processing.

Since the presence of oxygen can significantly influence the phase composition, an oxygen trap will be installed to further purify the inert gas used for the heat treatments at high temperatures, so the oxidation will be limited. Additional Zr foil will be used for wrapping the sample, acting as an oxygen getter. The powder mixing must be improved to suppress the observed compositional heterogeneities at the millimeter scale.

The EDS analysis presented above is obviously not complete. A quantitative EDS analysis is necessary to correctly measure the chemical composition of individual phases. However, this requires clustering of datapoints into phases, which is a non-trivial task, beyond the scope of this thesis. This analysis must be also automated as much as possible for two reasons – to speed up the analysis of the numerous samples and to limit the human input, getting more robust results. The full phase analysis for constructing the phase diagrams also requires XRD data as a complement to the EDS, either for identification of the existing phases, or for a description of new ones.

All these tasks are a part of an ongoing research project, supported by a Czech Science Foundation project no. 22-24563S, in collaboration with the Institute of Plasma Physics of Czech Academy of Sciences.

8 Concluding Remarks

Several unconventional applications of the field assisted sintering technology (FAST) were explored in this thesis: the manufacturing of composites with a metallic reinforcement lattice, upscaling the FAST for a single-run manufacturing of large tensile specimens, using blended elemental powder metallurgy (BEPM) for investigations of phase stability in Ti-Nb-Zr-O alloys in heterogeneous samples and the high-throughput characterization of the refractory complex-concentrated alloys (RCCAs).

The manufacturing of composites (Chapter 4) was successful only partially. The chemical etching of the lattice has greatly improved its surface roughness. The composite material exhibited increased strength only when compared with unannealed Al matrix. When it was properly annealed, brittle fracture occurred in the interfacial layer between the matrix and the reinforcement at the onset of yield. Moreover, the lattice geometry prevented proper penetration of the Al powder, resulting in a high porosity and poor sintering quality.

The upscaling and streamlining of the sintering process, described in Chapter 5, was successful. We were able to manufacture a homogenous, fully dense rod of Ti-5Al-5V-5Mo-3Cr alloy, with the yield strength reaching 1183 MPa and the ductility of 6 %, comparable to the commercially available alloy. The alloy can be made from blended elemental powders in a single FAST run, combining consolidation, homogenization and ageing heat treatment. The process can be used for rapid prototyping of new alloys, including tensile testing.

The BEPM was further exploited in Chapter 6 for investigation of the phase stability of Ti-xNb-7Zr-yO system. A Nb concentration gradient was used to measure the critical concentration of β stabilizers to suppress the α/α'' formation: 22 wt% of Nb. Homogeneous alloys with a controlled concentration of oxygen were also prepared, confirming the results obtained using the heterogeneous sample. The lowest elastic modulus of 64 GPa was measured in the single-phase Ti-29Nb-7Zr-0.7O sample. We have also discovered that martensitic α'' phase can form in a narrow range around the critical concentration of 22 wt%, even when the material is not quenched, but cooled at a moderate cooling rate ($100 - 400\,\mathrm{K/min}$).

Finally, in Chapter 7, we have designed and successfully tested a method for sintering multiple powder blends in a single specimen, creating a heterogeneous specimen across a wide range of alloy compositions. This method allowed high-throughput investigations of phase compositions of an AlTiTaNbZr refractory complex concentrated alloy.

The acquired experience with the BEPM was used for other projects as well, such as for preparing heterogenous samples for scanning acoustic microscopy, allowing high-throughput characterization of elastic modulus, and for defor-

mation tests, resolving local, compositionally dependent deformation mechanisms by DIC. However, these topics are beyond the scope of this thesis.

While manufacturing architectured composites will probably not be exploited further, the other methods have proven themselves as viable. The ability to reach high temperatures required for the alloy homogenization is a big advantage of FAST, supported by the ability to prepare small samples and a relative ease of use. Our current plan is to continue with the high-throughput investigations of the RCCAs, as reliable thermodynamic data about the system are needed.

Bibliography

1. Upadhyaya, G. S. *Powder metallurgy technology* 160 pp. ISBN: 978-1-898326-40-3 (Cambridge International Science Publishing, Cambridge, 1997).
2. Fang, Z. Z. *Sintering of Advanced Materials* 1st ed. 502 pp. ISBN: 978-1-84569-994-9 (Elsevier, 2010).
3. Vandiver, P. B., Soffer, O., Klima, B. & Svoboda, J. The Origins of Ceramic Technology at Dolni Věstonice, Czechoslovakia. *Science* **246,** 1002–1008. DOI: 10.1126/science.246.4933.1002 (1989).
4. Bloxam, A. G. *British pat.* 190609020 (A). https://worldwide.espacenet.com/publicationDetails/biblio?FT=D&date=19061213&DB=&locale=en_EP&CC=GB&NR=190609020A&KC=A&ND=4(1906).
5. Bloxam, A. G. *British pat.* 190527002 (A). https://worldwide.espacenet.com/publicationDetails/biblio?FT=D&date=19061213&DB=&locale=en_EP&CC=GB&NR=190527002A&KC=A&ND=4(1906).
6. Weintraub, G. & Rush, H. *US Patent* 1071488A. https://patents.google.com/patent/US1071488A/en(1913).
7. Grasso, S., Sakka, Y. & Maizza, G. Electric current activated/assisted sintering (ECAS): a review of patents 1906–2008. *Science and Technology of Advanced Materials* **10,** 053001. ISSN: 1468-6996. DOI: 10.1088/1468-6996/10/5/053001 (2009).
8. Guillon, O. *et al.* Field-Assisted Sintering Technology/Spark Plasma Sintering: Mechanisms, Materials, and Technology Developments. *Advanced Engineering Materials* **16,** 830–849. ISSN: 1527-2648. DOI: 10.1002/adem.201300409 (2014).
9. Hulbert, D. M., Anders, A., Andersson, J., Lavernia, E. J. & Mukherjee, A. K. A discussion on the absence of plasma in spark plasma sintering. *Scripta Materialia* **60,** 835–838. ISSN: 1359-6462. DOI: 10.1016/j.scriptamat.2008.12.059 (2009).
10. Trzaska, Z., Couret, A. & Monchoux, J.-P. Spark plasma sintering mechanisms at the necks between TiAl powder particles. *Acta Materialia* **118,** 100–108. ISSN: 1359-6454. DOI: 10.1016/j.actamat.2016.07.043 (Supplement C 2016).
11. Collard, C., Trzaska, Z., Durand, L., Chaix, J.-M. & Monchoux, J.-P. Theoretical and experimental investigations of local overheating at particle contacts in spark plasma sintering. *Powder Technology* **321,** 458–470. ISSN: 0032-5910. DOI: 10.1016/j.powtec.2017.08.033 (2017).

12. Trzaska, Z. & Monchoux, J.-P. Electromigration experiments by spark plasma sintering in the silver–zinc system. *Journal of Alloys and Compounds* **635,** 142–149. ISSN: 0925-8388. DOI: 10.1016/j.jallcom.2015.02.122 (Supplement C 2015).

13. Wang, Y. C., Fu, Z. Y. & Zhang, Q. J. SPS Temperature Distribution of Different Conductivity Materials. *Key Engineering Materials* **224-226,** 717–720. DOI: 10.4028/www.scientific.net/KEM.224-226.717 (2002).

14. Anselmi-Tamburini, U., Gennari, S., Garay, J. E. & Munir, Z. A. Fundamental investigations on the spark plasma sintering/synthesis process: II. Modeling of current and temperature distributions. *Materials Science and Engineering: A* **394,** 139–148. ISSN: 0921-5093. DOI: 10.1016/j.msea.2004.11.019 (2005).

15. Laptev, A. M., Bram, M., Vanmeensel, K., Gonzalez-Julian, J. & Guillon, O. Enhancing efficiency of field assisted sintering by advanced thermal insulation. *Journal of Materials Processing Technology* **262,** 326–339. ISSN: 0924-0136. DOI: 10.1016/j.jmatprotec.2018.07.008 (2018).

16. Voisin, T. *et al.* Temperature control during Spark Plasma Sintering and application to up-scaling and complex shaping. *Journal of Materials Processing Technology* **213,** 269–278. ISSN: 0924-0136. DOI: 10.1016/j.jmatprotec.2012.09.023 (2013).

17. Morsi, K., El-Desouky, A., Johnson, B., Mar, A. & Lanka, S. Spark plasma extrusion (SPE): Prospects and potential. *Scripta Materialia* **61,** 395–398. ISSN: 1359-6462. DOI: 10.1016/j.scriptamat.2009.04.026 (2009).

18. Lichtinghagen, K. *pat.* 4420294 (1983).

19. Hallett, R., Cox, J. R. & Morsi, K. Novel Spark Plasma Extrusion of Titanium Above and Below the —-Transus: Effect on Microstructure and Properties. *Metallurgical and Materials Transactions B* **51,** 1363–1369. ISSN: 1543-1916. DOI: 10.1007/s11663-020-01845-5 (2020).

20. Weston, N. S. & Jackson, M. FAST-forge - A new cost-effective hybrid processing route for consolidating titanium powder into near net shape forged components. *Journal of Materials Processing Technology* **243,** 335–346. ISSN: 0924-0136. DOI: 10.1016/j.jmatprotec.2016.12.013 (2017).

21. Calvert, E., Wynne, B., Weston, N., Tudball, A. & Jackson, M. Thermomechanical processing of a high strength metastable beta titanium alloy powder, consolidated using the low-cost FAST-forge process. *Journal of Materials Processing Technology* **254,** 158–170. ISSN: 0924-0136. DOI: 10.1016/j.jmatprotec.2017.11.035 (2018).

22. Arnaud, C. *et al.* Dog-bone copper specimens prepared by one-step spark plasma sintering. *Journal of Materials Science* **50,** 7364–7373. ISSN: 1573-4803. DOI: 10.1007/s10853-015-9293-5 (2015).

23. Manière, C., Torresani, E. & Olevsky, E. A. Simultaneous Spark Plasma Sintering of Multiple Complex Shapes. *Materials* **12,** 557. DOI: 10.3390/ma12040557 (2019).

24. Voisin, T. *et al.* An Innovative Way to Produce γ-TiAl Blades: Spark Plasma Sintering. *Advanced Engineering Materials* **17,** 1408–1413. ISSN: 1527-2648. DOI: 10.1002/adem.201500019 (2015).

25. Lukac, F. *et al.* Spark plasma sintering of gas atomized high-entropy alloy HfNbTaTiZr. *Journal of Materials Research* **33,** 3247–3257. ISSN: 0884-2914, 2044-5326. DOI: 10.1557/jmr.2018.320 (2018).

26. Karre, R. *et al.* Comparative study on Ti-Nb binary alloys fabricated through spark plasma sintering and conventional P/M routes for biomedical application. *Materials Science and Engineering: C* **94,** 619–627. ISSN: 0928-4931. DOI: 10.1016/j.msec.2018.10.006 (2019).

27. Terayama, A., Fuyama, N., Yamashita, Y., Ishizaki, I. & Kyogoku, H. Fabrication of Ti–Nb alloys by powder metallurgy process and their shape memory characteristics. *Journal of Alloys and Compounds. SI :ICOMAT2011* **577,** S408–S412. ISSN: 0925-8388. DOI: 10.1016/j.jallcom.2011.12.166 (2013).

28. Amigó, A., Vicente, A., Afonso, C. R. M. & Amigó, V. Mechanical Properties and the Microstructure of β Ti-35Nb-10Ta-xFe Alloys Obtained by Powder Metallurgy for Biomedical Applications. *Metals* **9,** 76. DOI: 10.3390/met9010076 (2019).

29. Taddei, E. B., Henriques, V. A. R., Silva, C. R. M. & Cairo, C. A. A. Production of new titanium alloy for orthopedic implants. *Materials Science and Engineering: C. Selected Papers Presented at Symposia B and F at the Brazilian Society for Materials Research* **24,** 683–687. ISSN: 0928-4931. DOI: 10.1016/j.msec.2004.08.011 (2004).

30. Carman, A. *et al.* Role of alloying elements in microstructure evolution and alloying elements behaviour during sintering of a near-β titanium alloy. *Materials Science and Engineering: A* **528,** 1686–1693. ISSN: 0921-5093. DOI: 10.1016/j.msea.2010.11.004 (2011).

31. Siqueira, R. P., Sandim, H. R. Z., Hayama, A. O. F. & Henriques, V. A. R. Microstructural evolution during sintering of the blended elemental Ti–5Al–2.5Fe alloy. *Journal of Alloys and Compounds* **476,** 130–137. ISSN: 0925-8388. DOI: 10.1016/j.jallcom.2008.09.004 (2009).

32. Sharma, B., Vajpai, S. K. & Ameyama, K. Microstructure and properties of beta Ti–Nb alloy prepared by powder metallurgy route using titanium hydride powder. *Journal of Alloys and Compounds* **656,** 978–986. ISSN: 0925-8388. DOI: 10.1016/j.jallcom.2015.10.053 (2016).

33. Zou, L. M., Yang, C., Long, Y., Xiao, Z. Y. & Li, Y. Y. Fabrication of biomedical Ti–35Nb–7Zr–5Ta alloys by mechanical alloying and spark plasma sintering. *Powder Metallurgy* **55,** 65–70. ISSN: 0032-5899, 1743-2901. DOI: 10.1179/1743290111Y.0000000021 (2012).

34. Collins, P. C., Banerjee, R., Banerjee, S. & Fraser, H. L. Laser deposition of compositionally graded titanium–vanadium and titanium–molybdenum alloys. *Materials Science and Engineering: A* **352,** 118–128. ISSN: 0921-5093. DOI: 10.1016/S0921-5093(02)00909-7 (2003).

35. Miracle, D. B., Li, M., Zhang, Z., Mishra, R. & Flores, K. M. Emerging Capabilities for the High-Throughput Characterization of Structural Materials. *Annual Review of Materials Research* **51,** 131–164. ISSN: 1531-7331, 1545-4118. DOI: 10.1146/annurev-matsci-080619-022100 (2021).

36. Zhang, Z., Li, M., Cavin, J., Flores, K. & Mishra, R. A Fast and Robust Method for Predicting the Phase Stability of Refractory Complex Concentrated Alloys using Pairwise Mixing Enthalpy. *Acta Materialia* **241,** 118389. ISSN: 1359-6454. DOI: 10.1016/j.actamat.2022.118389 (2022).

37. *CALPHAD: Calculation of Phase Diagrams - A Comprehensive Guide* ISBN: 978-0-08-042129-2. DOI: 10.1016/S1470-1804(98)X8001-6 (Elsevier, 1998).

38. Dayananda, M. A. Analysis of multicomponent diffusion couples for interdiffusion fluxes and interdiffusion coefficients. *Journal of Phase Equilibria and Diffusion* **26,** 441–446. ISSN: 1863-7345. DOI: 10.1007/s11669-005-0032-5 (2005).

39. Zhong, J., Chen, L. & Zhang, L. High-throughput determination of high-quality interdiffusion coefficients in metallic solids: a review. *Journal of Materials Science*, 1–36. ISSN: 0022-2461. DOI: 10.1007/s10853-020-04805-1 (2020).

40. Krebs, R. E. *The History and Use of Our Earth's Chemical Elements* 2nd ed. ISBN: 978-0-313-33438-2 (Greenwood Press, 2006).

41. Lütjering, G. & Williams, J. C. *Titanium* 379 pp. ISBN: 978-3-540-71397-5 (Springer Berlin Heidelberg, Berlin, Heidelberg, 2007).

42. Banerjee, S. & Mukhopadhyay, P. *Phase Transformations, Volume 12: Examples from Titanium and Zirconium Alloys* 1 edition. 840 pp. ISBN: 978-0-08-042145-2 (Elsevier Science, Amsterdam ; Oxford, 2007).

43. Welsch, G., Boyer, R. & Collings, E. W. *Materials Properties Handbook: Titanium Alloys* 1206 pp. ISBN: 978-0-87170-481-8 (ASM International, 1993).

44. Boyer, R. Applications of beta titanium alloys in airframes. *The Minerals, Metal & Materials Society(USA)*, 335–346 (1993).

45. Jones, N. G., Dashwood, R. J., Jackson, M. & Dye, D. — Phase decomposition in Ti–5Al–5Mo–5V–3Cr. *Acta Materialia* **57,** 3830–3839. ISSN: 1359-6454. DOI: 10.1016/j.actamat.2009.04.031 (2009).

46. Moiseyev, V. N. *Titanium Alloys: Russian Aircraft and Aerospace Applications* 216 pp. ISBN: 978-0-429-12979-7. DOI: 10.1201/9781420037678 (CRC Press, Boca Raton, 2005).

47. Jones, N. G., Dashwood, R. J., Dye, D. & Jackson, M. Thermomechanical processing of Ti–5Al–5Mo–5V–3Cr. *Materials Science and Engineering: A* **490,** 369–377. ISSN: 0921-5093. DOI: 10.1016/j.msea.2008.01.055 (2008).

48. Boyer, R. R. & Briggs, R. D. The use of β titanium alloys in the aerospace industry. *Journal of Materials Engineering and Performance* **14,** 681–685. ISSN: 1544-1024. DOI: 10.1361/105994905X75448 (2005).

49. Ren, L., Xiao, W., Han, W., Ma, C. & Zhou, L. Influence of duplex ageing on secondary α precipitates and mechanical properties of the near —-Ti alloy Ti-55531. *Materials Characterization* **144,** 1–8. ISSN: 1044-5803. DOI: 10.1016/j.matchar.2018.06.025 (2018).

50. Shekhar, S., Sarkar, R., Kar, S. K. & Bhattacharjee, A. Effect of solution treatment and aging on microstructure and tensile properties of high strength — titanium alloy, Ti–5Al–5V–5Mo–3Cr. *Materials & Design. Lightweight Materials and Structural Solutions for Transport Applications* **66,** 596–610. ISSN: 0261-3069. DOI: 10.1016/j.matdes.2014.04.015 (2015).

51. Xu, S.-h., Liu, Y., Liu, B., Wang, X. & Chen, Z.-x. Microstructural evolution and mechanical properties of Ti–5Al–5Mo–5V–3Cr alloy by heat treatment with continuous temperature gradient. *Transactions of Nonferrous Metals Society of China* **28,** 273–281. ISSN: 1003-6326. DOI: 10.1016/S1003-6326(18)64660-6 (2018).

52. Calvert, E. L., Knowles, A. J., Pope, J. J., Dye, D. & Jackson, M. Novel high strength titanium-titanium composites produced using field-assisted sintering technology (FAST). *Scripta Materialia* **159,** 51–57. ISSN: 1359-6462. DOI: 10.1016/j.scriptamat.2018.08.036 (2019).

53. Schwab, H. *et al.* Processing of Ti-5553 with improved mechanical properties via an in-situ heat treatment combining selective laser melting and substrate plate heating. *Materials & Design* **130,** 83–89. ISSN: 0264-1275. DOI: 10.1016/j.matdes.2017.05.010 (2017).

54. Liu, W. *et al.* Ti–5Al–5V–5Mo–3Cr–1Zr (Ti-55531) alloy with excellent mechanical properties fabricated by spark plasma sintering combined with in-situ aging. *Materials Science and Engineering: A* **847,** 143316. ISSN: 0921-5093. DOI: 10.1016/j.msea.2022.143316 (2022).

55. Niinomi, M. Mechanical properties of biomedical titanium alloys. *Materials Science and Engineering: A* **243,** 231–236. ISSN: 0921-5093. DOI: 10.1016/S0921-5093(97)00806-X (1998).

56. Qazi, J. I., Rack, H. J. & Marquardt, B. High-strength metastable beta-titanium alloys for biomedical applications. *JOM* **56,** 49–51. ISSN: 1543-1851. DOI: 10.1007/s11837-004-0253-9 (2004).

57. Raabe, D., Sander, B., Friák, M., Ma, D. & Neugebauer, J. Theory-guided bottom-up design of β-titanium alloys as biomaterials based on first principles calculations: Theory and experiments. *Acta Materialia* **55,** 4475–4487. ISSN: 1359-6454. DOI: 10.1016/j.actamat.2007.04.024 (2007).

58. Geetha, M., Singh, A. K., Asokamani, R. & Gogia, A. K. Ti based biomaterials, the ultimate choice for orthopaedic implants – A review. *Progress in Materials Science* **54,** 397–425. ISSN: 0079-6425. DOI: 10.1016/j.pmatsci.2008.06.004 (2009).

59. Cardoso, F. F., Ferrandini, P. L., Lopes, E. S. N., Cremasco, A. & Caram, R. Ti–Mo alloys employed as biomaterials: Effects of composition and aging heat treatment on microstructure and mechanical behavior. *Journal of the Mechanical Behavior of Biomedical Materials* **32,** 31–38. ISSN: 1751-6161. DOI: 10.1016/j.jmbbm.2013.11.021 (2014).

60. Stráský, J., Preisler, D., Bartha, K. & Janeček, M. Manufacturing of Biomedical Ti-Based Alloys with High Oxygen Content and Various Amount of Beta-Stabilizing Elements. *Materials Science Forum* **941,** 2471–2476. ISSN: 1662-9752. DOI: 10.4028/www.scientific.net/MSF.941.2471 (2018).

61. Zhang, L.-C. & Chen, L.-Y. A Review on Biomedical Titanium Alloys: Recent Progress and Prospect. *Advanced Engineering Materials* **21,** 1801215. ISSN: 1527-2648. DOI: 10.1002/adem.201801215 (2019).

62. Abdel-Hady Gepreel, M. & Niinomi, M. Biocompatibility of Ti-alloys for long-term implantation. *Journal of the Mechanical Behavior of Biomedical Materials* **20,** 407–415. ISSN: 1751-6161. DOI: 10.1016/j.jmbbm.2012.11.014 (2013).

63. Eisenbarth, E., Velten, D., Müller, M., Thull, R. & Breme, J. Biocompatibility of β-stabilizing elements of titanium alloys. *Biomaterials* **25,** 5705–5713. ISSN: 0142-9612. DOI: 10.1016/j.biomaterials.2004.01.021 (2004).

64. Hao, Y. L., Li, S. J., Sun, S. Y., Zheng, C. Y. & Yang, R. Elastic deformation behaviour of Ti–24Nb–4Zr–7.9Sn for biomedical applications. *Acta Biomaterialia* **3,** 277–286. ISSN: 1742-7061. DOI: 10.1016/j.actbio.2006.11.002 (2007).

65. Wang, Q., Dong, C. & Liaw, P. K. Structural Stabilities of β-Ti Alloys Studied Using a New Mo Equivalent Derived from $[\beta/(\alpha + \beta)]$ Phase-Boundary Slopes. *Metallurgical and Materials Transactions A* **46,** 3440–3447. ISSN: 1543-1940. DOI: 10.1007/s11661-015-2923-3 (2015).

66. Abdel-Hady, M., Hinoshita, K. & Morinaga, M. General approach to phase stability and elastic properties of β-type Ti-alloys using electronic parameters. *Scripta Materialia* **55,** 477–480. ISSN: 1359-6462. DOI: 10.1016/j.scriptamat.2006.04.022 (2006).

67. Abdel-Hady, M. *et al.* Phase stability change with Zr content in β-type Ti–Nb alloys. *Scripta Materialia* **57,** 1000–1003. ISSN: 1359-6462. DOI: 10.1016/j.scriptamat.2007.08.003 (2007).

68. Wei, Q. *et al.* Influence of oxygen content on microstructure and mechanical properties of Ti–Nb–Ta–Zr alloy. *Materials & Design* **32,** 2934–2939. ISSN: 0261-3069. DOI: 10.1016/j.matdes.2010.11.049 (2011).

69. Tahara, M., Kim, H. Y., Inamura, T., Hosoda, H. & Miyazaki, S. Lattice modulation and superelasticity in oxygen-added β-Ti alloys. *Acta Materialia* **59,** 6208–6218. ISSN: 1359-6454. DOI: 10.1016/j.actamat.2011.06.015 (2011).

70. Tahara, M., Inamura, T., Kim, H. Y., Miyazaki, S. & Hosoda, H. Role of oxygen atoms in α'' martensite of Ti-20at.% Nb alloy. *Scripta Materialia* **112,** 15–18. ISSN: 1359-6462. DOI: 10.1016/j.scriptamat.2015.08.033 (2016).

71. Kawano, S., Kobayashi, S. & Okano, S. Effect of Oxygen Addition on the Formation of α'' Martensite and Athermal ω in Ti–Nb Alloys. *Materials Transactions* **60,** 1842–1849. DOI: 10.2320/matertrans.ME201908 (2019).

72. Ahmed, T. & Rack, H. J. *pat.* AU705336B2. https://patents.google.com/patent/AU705336B2/en(1999).

73. Stráský, J. *et al.* Increasing strength of a biomedical Ti-Nb-Ta-Zr alloy by alloying with Fe, Si and O. *Journal of the Mechanical Behavior of Biomedical Materials* **71,** 329–336. ISSN: 1751-6161. DOI: 10.1016/j.jmbbm.2017.03.026 (2017).

74. Stráský, J. *et al.* Achieving high strength and low elastic modulus in interstitial biomedical Ti–Nb–Zr–O alloys through compositional optimization. *Materials Science and Engineering: A* **839,** 142833. ISSN: 0921-5093. DOI: 10.1016/j.msea.2022.142833 (2022).

75. Chawla, K. K. *Composite materials: science and engineering* 3rd ed. 542 pp. ISBN: 978-0-387-74364-6 (Springer Science+Business Media, New York, 2012).

76. *Architectured Materials in Nature and Engineering: Archimats* (eds Estrin, Y., Bréchet, Y., Dunlop, J. & Fratzl, P.) (Springer International Publishing, 2019). ISBN: 978-3-030-11941-6. DOI: 10.1007/978-3-030-11942-3. https://www.springer.com/gp/book/9783030119416 (Nov. 18, 2020).

77. Martin, G. *et al.* Coupling electron beam melting and spark plasma sintering: A new processing route for achieving titanium architectured microstructures. *Scripta Materialia* **122,** 5–9. ISSN: 1359-6462. DOI: 10.1016/j.scriptamat.2016.05.001 (2016).

78. Barrie, C., Fernandez-Silva, B., Snell, R., Todd, I. & Jackson, M. AddFAST: A hybrid technique for tailoring microstructures in titanium-titanium composites. *Journal of Materials Processing Technology* **315,** 117920. ISSN: 0924-0136. DOI: 10.1016/j.jmatprotec.2023.117920 (2023).

79. Cakmak, E. *et al.* Feasibility Study of Making Metallic Hybrid Materials Using Additive Manufacturing. *Metallurgical and Materials Transactions A* **49,** 5035–5041. ISSN: 1543-1940. DOI: 10.1007/s11661-018-4741-x (2018).

80. De Lama, M. A. *et al.* Microstructural stability of spark-plasma-sintered Wf/W composite with zirconia interface coating under high-heat-flux hydrogen beam irradiation. *Nuclear Materials and Energy* **13,** 74–80. ISSN: 2352-1791. DOI: 10.1016/j.nme.2017.06.007 (2017).

81. Pripanapong, P., Umeda, J., Imai, H., Takahashi, M. & Kondoh, K. Tensile Strength of Ti/Mg Alloys Dissimilar Bonding Material Fabricated by Spark Plasma Sintering. *IJEIR* **5,** 253–259. ISSN: 22775668 (2016).

82. Zhang, M. *et al.* 3D printed Mg-NiTi interpenetrating-phase composites with high strength, damping capacity, and energy absorption efficiency. *Science Advances* **6,** eaba5581. DOI: 10.1126/sciadv.aba5581 (2020).

83. Yamane, T. & Ueda, J. Mechanical Properties of Commercial Pure Titanium at High Temperature. *Transactions of the Japan Institute of Metals* **7,** 91–94. DOI: 10.2320/matertrans1960.7.91 (1966).

84. Ji, S. M. *et al.* Characterization of Ti-6Al-4V alloy in the temperature range of warm metal forming and fracture analysis of the warm capping process. *Journal of Materials Research and Technology* **18,** 1590–1606. ISSN: 2238-7854. DOI: 10.1016/j.jmrt.2022.03.066 (2022).

85. *ASM Handbook, Volume 2: Properties of Wrought Aluminum and Aluminum Alloys* 456 pp. ISBN: 978-1-62708-162-7 (ASM International, 1990).

86. Touloukian, Y. S., Kirby, R. K., Taylor, R. E. & Desai, P. D. *Thermal Expansion: Metallic elements and alloys* ISBN: 978-1-4757-1624-5 978-1-4757-1622-1. DOI: 10.1007/978-1-4757-1622-1 (Springer US, Boston, MA, 1975).

87. Schaedler, T. A. & Carter, W. B. Architected Cellular Materials. *Annual Review of Materials Research* **46,** 187–210. ISSN: 1531-7331. DOI: 10.1146/annurev-matsci-070115-031624 (2016).

88. Al-Ketan, O., Rowshan, R. & Abu Al-Rub, R. K. Topology-mechanical property relationship of 3D printed strut, skeletal, and sheet based periodic metallic cellular materials. *Additive Manufacturing* **19,** 167–183. ISSN: 2214-8604. DOI: 10.1016/j.addma.2017.12.006 (2018).

89. Jamshidi, P. *et al.* Selective Laser Melting of Ti-6Al-4V: The Impact of Post-processing on the Tensile, Fatigue and Biological Properties for Medical Implant Applications. *Materials* **13.** ISSN: 1996-1944. DOI: 10.3390/ma13122813 (2020).

90. Dobrzański, L., Dobrzańska-Danikiewicz, A., Gaweł, T. & Achtelik-Franczak, A. Selective Laser Sintering And Melting Of Pristine Titanium And Titanium Ti6Al4V Alloy Powders And Selection Of Chemical Environment For Etching Of Such Materials. *Archives of Metallurgy and Materials* **60,** 2039–2046. ISSN: 2300-1909. DOI: 10.1515/amm-2015-0346 (2015).

91. Cantor, B., Chang, I. T. H., Knight, P. & Vincent, A. J. B. Microstructural development in equiatomic multicomponent alloys. *Materials Science and Engineering: A* **375-377,** 213–218. ISSN: 0921-5093. DOI: 10.1016/j.msea.2003.10.257 (2004).

92. Yeh, J.-W. *et al.* Formation of simple crystal structures in Cu-Co-Ni-Cr-Al-Fe-Ti-V alloys with multiprincipal metallic elements. *Metallurgical and Materials Transactions A* **35,** 2533–2536. ISSN: 1543-1940. DOI: 10.1007/s11661-006-0234-4 (2004).

93. Yeh, J.-W. *et al.* Nanostructured High-Entropy Alloys with Multiple Principal Elements: Novel Alloy Design Concepts and Outcomes. *Advanced Engineering Materials* **6,** 299–303. ISSN: 1527-2648. DOI: https://doi.org/10.1002/adem.200300567 (2004).

94. Miracle, D. B. & Senkov, O. N. A critical review of high entropy alloys and related concepts. *Acta Materialia* **122,** 448–511. ISSN: 1359-6454. DOI: 10.1016/j.actamat.2016.08.081 (2017).

95. Senkov, O. N., Miracle, D. B., Chaput, K. J. & Couzinie, J.-P. Development and exploration of refractory high entropy alloys—A review. *Journal of Materials Research* **33,** 3092–3128. ISSN: 2044-5326. DOI: 10.1557/jmr.2018.153 (2018).

96. Reed, R. C. *The Superalloys: Fundamentals and Applications* DOI: 10.1017/CBO9780511541285 (Cambridge University Press, 2006).

97. Senkov, O. N., Gorsse, S. & Miracle, D. B. High temperature strength of refractory complex concentrated alloys. *Acta Materialia* **175,** 394–405. ISSN: 1359-6454. DOI: 10.1016/j.actamat.2019.06.032 (2019).

98. Miracle, D. B., Tsai, M.-H., Senkov, O. N., Soni, V. & Banerjee, R. Refractory high entropy superalloys (RSAs). *Scripta Materialia* **187,** 445–452. ISSN: 1359-6462. DOI: 10.1016/j.scriptamat.2020.06.048 (2020).

99. Miracle, D. B. *et al.* Exploration and Development of High Entropy Alloys for Structural Applications. *Entropy* **16,** 494–525. DOI: 10.3390/e16010494 (2014).

100. Meyers, R. A. *Encyclopedia of Analytical Chemistry* 14344 pp. ISBN: 978-0-471-97670-7 (Wiley, 2006).

101. Zaefferer, S. & Elhami, N.-N. Theory and application of electron channelling contrast imaging under controlled diffraction conditions. *Acta Materialia* **75,** 20–50. ISSN: 1359-6454. DOI: 10.1016/j.actamat.2014.04.018 (2014).

102. Heiple, C. R. & Carpenter, S. H. Acoustic emission produced by deformation of metals and alloys - A review. *Journal of Acoustic Emission* **6,** 177–204. ISSN: 0730-0050 (1987).

103. Huang, M. *et al.* Using acoustic emission in fatigue and fracture materials research. *JOM* **50,** 1–14 (1998).

104. Landa, M. *et al.* Modal resonant ultrasound spectroscopy for ferroelastics. *Applied Physics A* **96,** 557–567. ISSN: 1432-0630. DOI: 10.1007/s00339-008-5047-4 (2009).

105. *ASM Handbook, Volume 4: Heat Treating of Aluminum Alloys* (ASM International, 1991).

106. *Binary Alloy Phase Diagrams Vol. 1* (ed Massalski, T. B.) (American Society for Metals, 1986). ISBN: 0-87170-262-2.

107. *Binary Alloy Phase Diagrams Vol. 2* (ed Massalski, T. B.) (American Society for Metals, 1986). ISBN: 0-87170-262-2.

108. Li, Z. *et al.* 700 °C Isothermal Section of the Al-Ti-Si Ternary Phase Diagram. *Journal of Phase Equilibria and Diffusion* **35,** 564–574. ISSN: 1863-7345. DOI: 10.1007/s11669-014-0325-7 (2014).

109. Raman, A. & Schubert, K. Über den Aufbau einiger zu TiAl3 verwandter Legierungsreihen. II. Untersuchungen in einigen T-Al-Si- und T4...6-In-Systemen. *Zeitschrift für Metallkunde,* 44–52 (1965).

110. Schubert, K. *et al.* Einige Strukturdaten metallischer Phasen (8). *Naturwissenschaften* **50,** 41–41. ISSN: 1432-1904. DOI: 10.1007/BF00622812 (1963).

111. Momma, K. & Izumi, F. VESTA 3 for three-dimensional visualization of crystal, volumetric and morphology data. *Journal of Applied Crystallography* **44,** 1272–1276. ISSN: 0021-8898. DOI: 10.1107/S0021889811038970 (2011).

112. Wang, J., Liu, Y., Liu, Y., Wu, C. & Su, X. The Isothermal Section of the Al-Si-Ti Ternary System at 550 °C. *Journal of Phase Equilibria and Diffusion* **40,** 810–819. ISSN: 1863-7345. DOI: 10.1007/s11669-019-00774-4 (2019).

113. Luo, Q., Li, Q., Zhang, J.-Y., Chen, S.-L. & Chou, K.-C. Experimental investigation and thermodynamic calculation of the Al–Si–Ti system in Al-rich corner. *Journal of Alloys and Compounds* **602,** 58–65. ISSN: 0925-8388. DOI: 10.1016/j.jallcom.2014.02.107 (2014).

114. Egusa, D. & Abe, E. The structure of long period stacking/order Mg–Zn–RE phases with extended non-stoichiometry ranges. *Acta Materialia* **60,** 166–178. ISSN: 1359-6454. DOI: 10.1016/j.actamat.2011.09.030 (2012).

115. Zhang, X., Li, C., Zheng, M., Zhong, H. & Gu, J. Alternative-band microstructure and LPSO phase in TiAl alloy produced by direct laser deposition. *Materials Characterization* **164,** 110315. ISSN: 1044-5803. DOI: 10.1016/j.matchar.2020.110315 (2020).

116. Raghavan, V. Al-Si-Ti (Aluminum-Silicon-Titanium). *Journal of Phase Equilibria and Diffusion* **30,** 82–83. ISSN: 1863-7345. DOI: 10.1007/s11669-008-9435-4 (2009).

117. Prusov, E., Deev, V. & Shunqi, M. Thermodynamic assessment of the Al-Mg-Si-Ti phase diagram for metal matrix composites design. *Materials Today: Proceedings. International Conference on Modern Trends in Manufacturing Technologies and Equipment 2019* **19,** 2005–2008. ISSN: 2214-7853. DOI: 10.1016/j.matpr.2019.07.061 (2019).

118. Fuji, A., Ikeuchi, K., Sato, Y. S. & Kokawa, H. Interlayer growth at interfaces of Ti/Al–1%Mn, Ti/Al–4·6%Mg and Ti/pure Al friction weld joints by post-weld heat treatment. *Science and Technology of Welding and Joining* **9,** 507–512. ISSN: 1362-1718. DOI: 10.1179/136217104225021797 (2004).

119. Fuji, A. In situ observation of interlayer growth during heat treatment of friction weld joint between pure titanium and pure aluminium. *Science and Technology of Welding and Joining* **7,** 413–416. ISSN: 1362-1718. DOI: 10.1179/136217102225006903 (2002).

120. Hamajima, T., Ameyama, K. & Fuji, A. Microstructural Change of Weld Interface in Ti/Al Friction Weld during Heat Treatment. *Journal of the Society of Materials Science, Japan* **44,** 1224–1230. DOI: 10.2472/jsms.44.1224 (1995).

121. Rajakumar, S. & Balasubramanian, V. Diffusion bonding of titanium and AA 7075 aluminum alloy dissimilar joints—process modeling and optimization using desirability approach. *The International Journal of Advanced Manufacturing Technology* **86,** 1095–1112. ISSN: 1433-3015. DOI: 10.1007/s00170-015-8223-7 (2016).

122. AlHazaa, A., Khan, T. I. & Haq, I. Transient liquid phase (TLP) bonding of Al7075 to Ti–6Al–4V alloy. *Materials Characterization* **61,** 312–317. ISSN: 1044-5803. DOI: 10.1016/j.matchar.2009.12.014 (2010).

123. Wilden, J., Bergmann, J. & Herz, S. Properties of diffusion welded hybrid joints titanium/aluminum. *Proceedings of the 3rd International Brazing and Soldering Conference,* 338–343 (2006).

124. Ma, Z. *et al.* A general strategy for the reliable joining of Al/Ti dissimilar alloys via ultrasonic assisted friction stir welding. *Journal of Materials Science & Technology* **35,** 94–99. ISSN: 1005-0302. DOI: 10.1016/j.jmst.2018.09.022 (2019).

125. Okazaki, K., Morinaka, K. & Conrad, H. Grain Growth Kinetics in Ti–O Alloys. *Transactions of the Japan Institute of Metals* **14,** 202–207. DOI: 10.2320/matertrans1960.14.202 (1973).

126. Bermingham, M. J., McDonald, S. D., Dargusch, M. S. & StJohn, D. H. Effect of Oxygen on the —-Grain Size of Cast Titanium. *Materials Science Forum* **654-656,** 1472–1475. ISSN: 1662-9752. DOI: 10.4028/www.scientific.net/MSF.654-656.1472 (2010).

127. Kozlík, J., Becker, H., Stráský, J., Harcuba, P. & Janeček, M. Manufacturing of fine-grained titanium by cryogenic milling and spark plasma sintering. *Materials Science and Engineering: A* **772,** 138783. ISSN: 0921-5093. DOI: 10.1016/j.msea.2019.138783 (2020).

128. Mavros, N. *et al.* Spark plasma sintering of low modulus titanium-niobium-tantalum-zirconium (TNTZ) alloy for biomedical applications. *Materials & Design* **183,** 108163. ISSN: 0264-1275. DOI: 10.1016/j.matdes.2019.108163 (2019).

129. Bahador, A. *et al.* Microstructure globularization of high oxygen concentration dual-phase extruded Ti alloys via powder metallurgy route. *Materials Characterization* **172,** 110855. ISSN: 1044-5803. DOI: 10.1016/j.matchar.2020.110855 (2021).

130. Yokota, K., Bahador, A., Shitara, K., Umeda, J. & Kondoh, K. Mechanisms of tensile strengthening and oxygen solid solution in single β-phase Ti-35 at.%Ta+O alloys. *Materials Science and Engineering: A* **802,** 140677. ISSN: 0921-5093. DOI: 10.1016/j.msea.2020.140677 (2021).

131. Furuta, T. *et al.* Mechanical Properties and Phase Stability of Ti-Nb-Ta-Zr-O Alloys. *Materials Transactions* **48,** 1124–1130. DOI: 10.2320/matertrans.48.1124 (2007).

132. Obbard, E. G. *et al.* The effect of oxygen on α″ martensite and superelasticity in Ti–24Nb–4Zr–8Sn. *Acta Materialia* **59,** 112–125. ISSN: 1359-6454. DOI: 10.1016/j.actamat.2010.09.015 (2011).

133. Tane, M., Hagihara, K., Ueda, M., Nakano, T. & Okuda, Y. Elastic-modulus enhancement during room-temperature aging and its suppression in metastable Ti–Nb-Based alloys with low body-centered cubic phase stability. *Acta Materialia* **102,** 373–384. ISSN: 1359-6454. DOI: 10.1016/j.actamat.2015.09.030 (2016).

134. Bönisch, M., Stoica, M. & Calin, M. Routes to control diffusive pathways and thermal expansion in Ti-alloys. *Scientific Reports* **10,** 3045. ISSN: 2045-2322. DOI: 10.1038/s41598-020-60038-x (2020).

135. Preisler, D. *et al.* High-throughput characterization of elastic moduli of Ti-Nb-Zr-O biomedical alloys fabricated by field-assisted sintering technique. *Journal of Alloys and Compounds* **932,** 167656. ISSN: 0925-8388. DOI: 10.1016/j.jallcom.2022.167656 (2023).

List of Figures

List of Tables

List of Abbreviations

3PB	3-point bending
AE	acoustic emission
BE	blended elements
BF	bright-field
BEPM	blended elemental powder metallurgy
BSE	backscatter electrons
CALPHAD	calculation of phase diagrams
CCA	complex concentrated alloy
CGHE	carrier gas hot extraction
CIF	crystallography information file
CTE	coefficient of thermal expansion
DF	dark-field
DIC	differential image correlation
EDS	energy-dispersive X-ray spectroscopy
FAST	field-assisted sintering technology
GB	grain boundary
HEA	high-entropy alloy
PA	prealloyed
RCCA	refractory complex concentrated alloy
RT	room temperature
RUS	resonant ultrasound spectroscopy
SAED	selected area electron diffraction
SE	secondary electrons
SEM	scanning electron microscopy
TEM	transmission electron microscopy
STEM	scanning transmission electron microscopy
TRIP	transformation-induced plasticity
TWIP	twinning-induced plasticity
Ti5553	Ti-5Al-5V-5Mo-3Cr alloy
WDS	wave-dispersive X-ray spectroscopy
XRD	X-ray diffraction

A Gibbs Energies of Ti-xNb-7Zr-yO Alloys

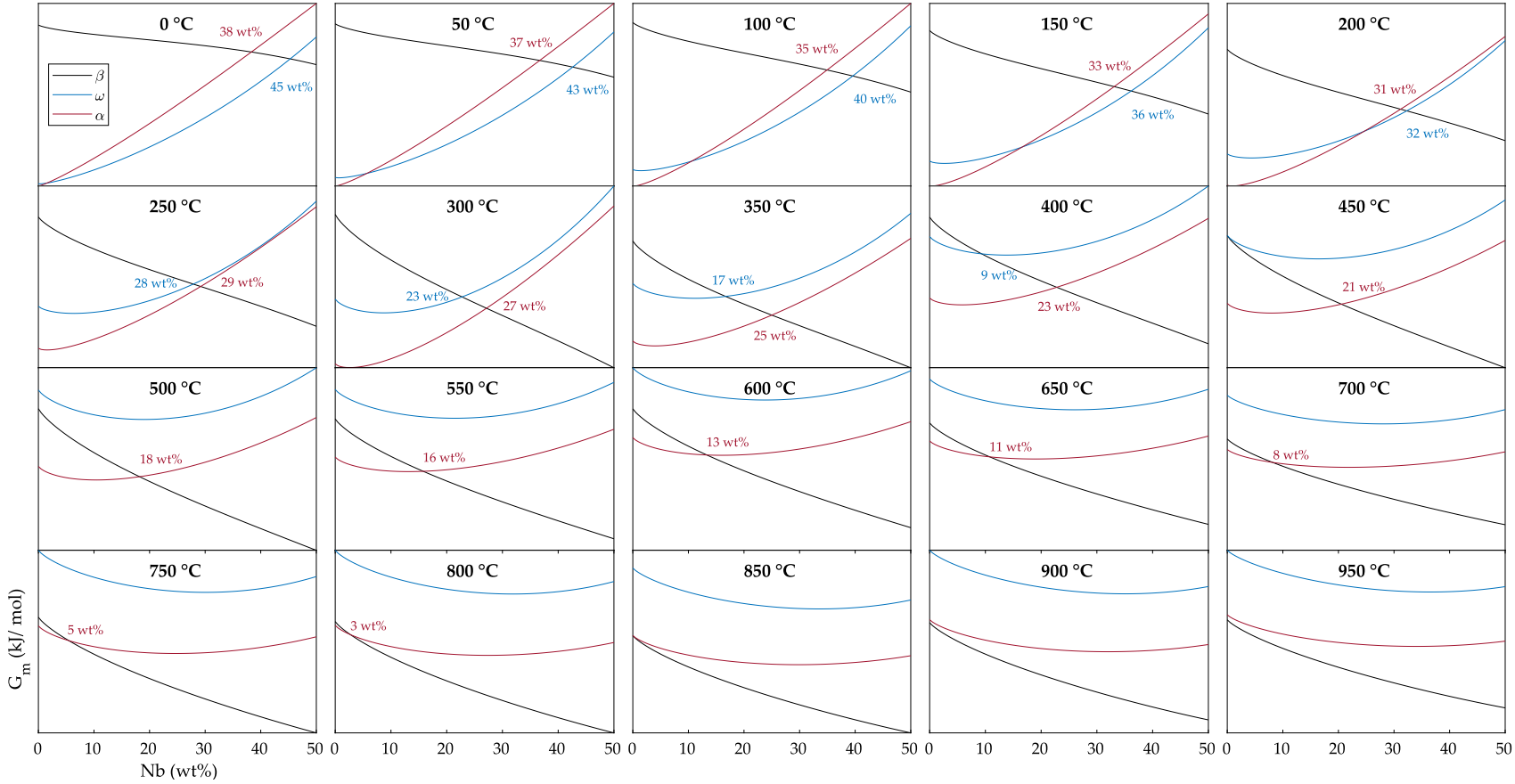

Figure A.1: Gibbs free energy curves of α, β and ω phases from 0 to 950 °C calculated for the alloy composition Ti-xNb-7Zr (i.e. not considering oxygen) by ThermoCalc. Concentrations at which the curves intersect are displayed, corresponding to the red and blue T_0 curve in Figure 6.19.

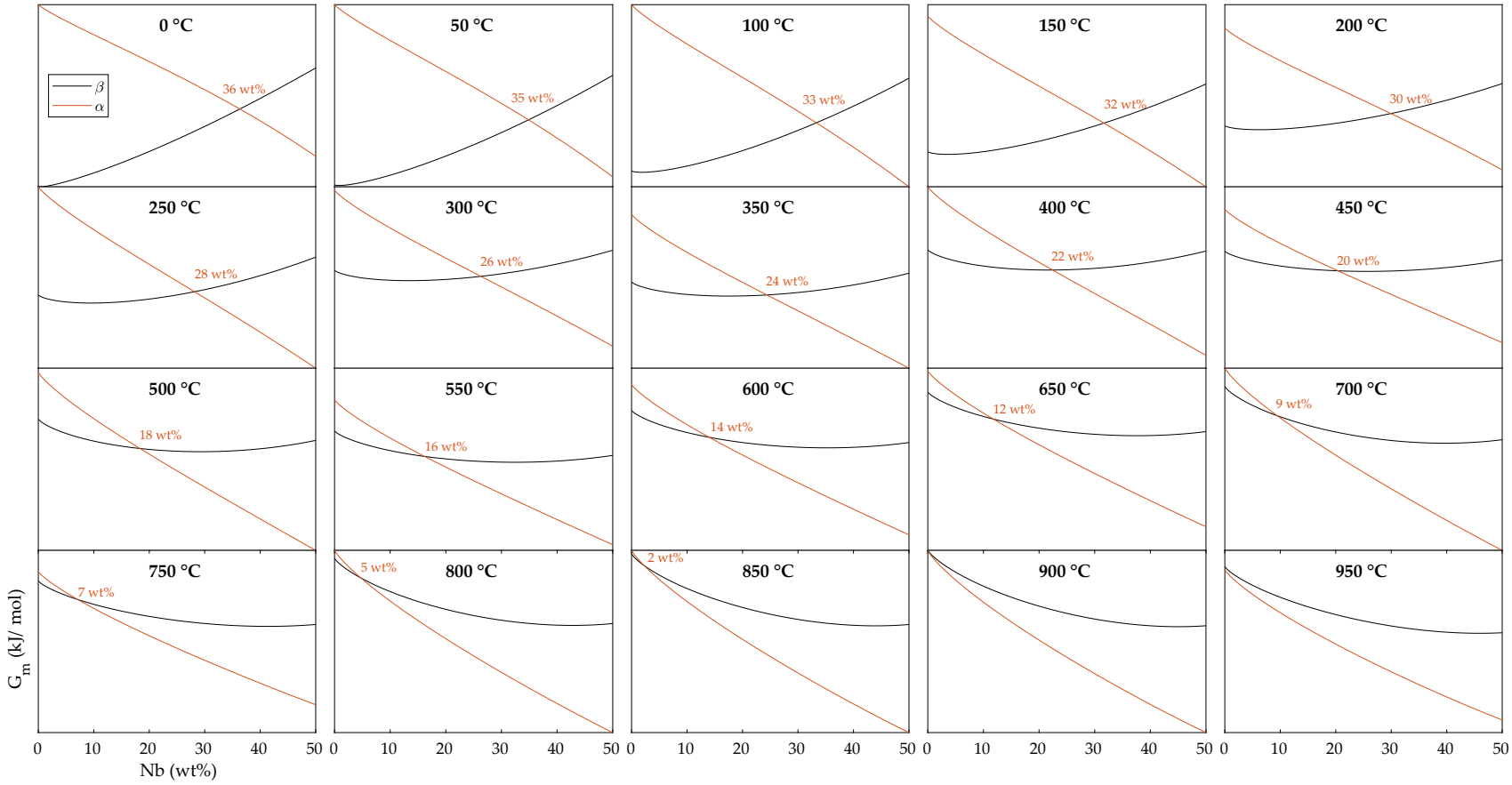

Figure A.2: Gibbs free energy curves of α and β phases from 0 to 950 °C calculated for the nominal alloy composition Ti-xNb-7Zr-0.8O by ThermoCalc. Concentrations at which the curves intersect are also displayed, corresponding to the orange T_0 curves in Figure 6.19.